Durham E-Theses

Understanding the Behaviour of Magnetic Damping in Ferromagnetic Thin-Film Multilayers

KALEL ALSAEED

How to cite:

Use policy

Understanding the Behaviour of Magnetic Damping in Ferromagnetic Thin-Film Multilayers

Kalel Alsaeed

A Thesis presented for the degree of
Doctor of Philosophy

Centre for Materials Physics
Department of Physics
Durham University

Abstract

Magnetisation processes including rotation of magnetisation, and dynamic propagation of domains walls in magnetic materials are regulated by the precessional damped motion of magnetic moments about an effective field. In thin-film systems, when a ferromagnetic (FM) layer is in contact with non-magnetic (NM), and excited with a microwave, spin-current is transmitted across the interface. This process is known as spin pumping and results in the transmission of energy and angular momentum. The structure of both the FM and NM layers greatly affects spin pumping, with the change of crystalline structure affecting both spin-pumping and two-magnon scattering. In Ferromagnetic Resonance (FMR) measurements, we can assess spin pumping by observing changes in the FMR linewidth when a non-magnetic layer is introduced. These alterations serve as exhibits of the transfer of spin angular momentum from the ferromagnetic material to the non-magnetic layer. Two-magnon scattering is the energy transfer from uniform-to-nonuniform precessional modes.

This thesis focuses on understanding variation in damping parameters between two identical 10 nm thick CoFe magnetic layers separated by Ag. The precessional dynamics were measured using FMR. The thickness of the Ag interlayer has a considerable impact on the damping parameter. When certain Ag layer thickness corresponds to an antiferromagnetic coupling peak that might lead to enhancement of the damping in our samples. The interaction of the Ruderman-Kittel-Kasuya-Yosida (RKKY) across the Ag layer could results in the formation of stationary spin-wave modes that are out of phase within the effective field. This could be a reason of the additional bump term to the frequency-dependence of the resonance linewidth over a certain frequency.

In the polarised neutron reflectivity and polarisation analysis (PNR/PA) investigation, when we relaxed the magnetization from hard-axis saturation, we expected the layers to align antiparallel along/against the beam direction as the field is reduced. The sample was rotated about the film's normal axis and measured twice, at 0 and 45 degrees. The results indicate that there was a reduced structural scattering length density (SLD) at the interface between Ag and CoFe, while there was an increase in the magnetic SLD during a 45-degree scan. These changes may be recognised as variations in composition and the presence of magnetic properties that exhibit anisotropic behaviour. In a further magnetic anisotropy study, we made an unusual sample different from typical samples where the sample stage remained static during the growth of the first and third NiFe layers. The Ag layer was formed in the usual way with the

sample stage rotating. Then, FMR measurements were carried out at various angles. The findings reveal that the frequency behaviour of both single and double resonance data remains linear and is not influenced by variations in measurement angles. This suggests that the anomalous enhanced linewidth seen in other samples with Ag spacer layers is not purely the result of misaligned magnetic anisotropies.

Declaration

Unless stated otherwise, the work in this thesis is solely that of the author. No part of this thesis has been submitted elsewhere for any other degree or qualification.

The Ferromagnetic Resonance (FMR) and Magneto-Optical Kerr Effect (MOKE) instruments required the formation of various components, including mounting brackets, sample holders, cryostat housings, and optics bench support frames. These designs were made by Dr. A.T. Hindmarch and Dr. B. Nicholson, while the construction was executed by the skilled mechanical workshop team within the physics department.

The samples explored in chapters 3 and 4 were prepared by the author with the guidance and support of Dr. A.T. Hindmarch. This collaboration also extended to the FMR measurements and the subsequent FMR analysis. X-ray Reflectivity (XRR) and X-ray Diffraction (XRD) for all the samples discussed in this thesis were conducted by the author. All tasks related to sample deposition, fabrication, and structural analysis were carried out at Durham University.

The acquisition of polarised neutron reflectivity data presented in chapter 4 was a cooperative effort, drawing upon the expertise of my supervisor, Dr. A.T. Hindmarch, and beamline scientists, Dr. Christy Kinane and Dr. Andrew Caruana. However, all data analysis was performed by the author, aided by the insightful input from the beamline scientists.

Acknowledgements

Firstly, I would like to thank my supervisor Dr. Aidan Hindmarch for his guidance, support, and friendship over the years and for entertaining my experimental ideas and encouraging me to continue tinkering with instruments, without which my interest in instrument development would certainly not have transpired. I would also like to thank my second supervisor Prof. Peter Hatton.

I am grateful for the welcoming provided by Dr. Christy Kinane, Dr. Andrew Caruana while attending the beamline experiments. This work would not have been possible without the support of Stephen Lishman and the rest of the mechanical workshop team. It has been a pleasure to share my time at Durham with Dr. Charles Swindells, Dr. Ariam Hernandez, Dr. Oto-Obong Inyang, Dr. Ben Nicholson, Dr. Faisal Alanazi, and Dr. Tahir Aduragba. Thank you for the great discussions, whether physics related or not, which kept us all going.

Lastly, but most significantly, I express my heartfelt gratitude to my family. To my parents in Saudi Arabia, your love and support across the miles have been a constant source of strength. To my wife, Dr. Amnah Obidan, here in Durham, your limitless support throughout my PhD journey has been irreplaceable, and your tireless care for our children, a blessing. To my delightful children, Aleen, and Ahmed, thank you for filling my life with joy and purpose. Your presence is the motivation that fuels my academic pursuits.

List of publications

Measuring Magnetic Hysteresis Curves with Polarised Soft X-ray Reflectivity.

Raymond Fan, Kiranjot, Razan Aboljadayel, **Kalel Alsaeed**, Peter Bencok, David Burn, Aidan Hindmarch and Paul Steadman

Journal of Synchrotron Radiation, Accepted (2023)

Contents

Chapter 1. Thesis Outline

1.1 Introduction

Magnetic damping and ferromagnetic resonance are pivotal to the understanding of ferromagnetic materials, especially in thin-film configurations. The oscillatory behaviour of magnetization, central to magnetic data storage and sensory applications, has captivated researchers in spintronics and magnetics, primarily driven by the imperative to manipulate the magnetic attributes of thin layers and nanoscale constructs. A heightened damping coefficient in ferromagnetic systems emerges as a coveted trait for tech applications. By increasing the damping, the magnetization precession lifetime diminishes, paving the way for faster data inscription and conversion. In opposition, in cutting-edge applications like spin-transfer torque magnetic random-access memory (MRAM) and magnetic apparatuses, a reduced magnetic damping is preferred. This decrement in damping aids in reducing the write-current, thereby optimizing spin wave transmission in these systems[1] .

The study aims to contribute to the understanding of magnetic damping phenomenon through experimental research with the aid of theory, to understand the role of damping in general and the modifications that can be implemented for both increasing and decreasing it. The focus was to investigate damping variation as a function of the non-magnetic layer thickness in a tri-layer system.

1.2 Aims of thesis

The aim of this thesis is to provide insight into the understanding of magnetisation damping in thin-films and nanostructures. The study focuses on damping in CoFe as ferromagnetic (FM) materials and Ag nonmagnetic materials. All samples were produced as thin films made by co-sputtering system. The thickness of the Ag interlayer has a considerable impact on the damping parameter. Spin-pumping between the two identical FM layers occurs when the Ag layer thickness corresponds to an antiferromagnetic (AF) coupling peak and leads to enhancement of the damping in our samples. As a result of the AF coupling across the Ag layer, stationary spin-wave modes in anti-phase are formed due to the Ruderman-Kittel-Kasuya-Yosida (RKKY) interaction into the effective field. This shows up as an additional bump term to the frequency-dependence of the resonance linewidth over a certain frequency. When the FM

layers are in a saturated state, both magnetized along the applied field direction yet the spin-pumping contribution to the damping persists.

1.3 Thesis Outline

In Chapter 2, the basic mechanisms that cause the static magnetic properties of thin film systems and the physical origins of magnetism are discussed. Also, understanding magnetic moments and how they can be arranged to categorise materials was significant. Chapter 3 The experimental techniques and processes used to produce and structurally characterise thin film magnetic systems are discussed. The samples in this investigation were grown using magnetron sputtering in an ultra-high vacuum deposition chamber, and various mechanisms of film growth are explained. The experimental methods, including functional magnetic measurements, are described in Chapter 4. The magnetization state of a material is typically characterised by functional magnetic measurements, and this state is defined by the orientation and strength of the material's magnetic moment. In Chapter 5, we start with an introduction to the fundamental concepts, then we analyse damping, experimental details, and ferromagnetic resonance (FMR) data. Effective damping techniques are described in depth, and their results are shown. Fitting procedures and data from x-ray reflectivity (XRR) and polarised neutron reflectivity/polarized analysis (PNR-PA) measurements on the CoFe/Ag (2.6nm)/CoFe sample system are discussed in Chapter 6. Also, we are studying a sample that is nominally antiferromagnetically (AF) coupled FM/Ag(2.6nm)/FM, and we have investigated the magnetic anisotropy present in this sample in Chapter 7.

Chapter 2. The phenomenon of magnetism in thin films

2.1 Introduction

This chapter discusses the fundamental mechanisms that give rise to the static magnetic characteristics of thin film systems, along with the physical origins of magnetism. Initially, we describe the formation of magnetic moments and how their arrangement can be used to categorise materials. Next, we discuss the concept of induced magnetism in a non-magnetic material at the contact with a magnetic material. Following that, the energy contributions that occur in ferromagnetic systems are discussed, and the material categories that result from such interactions are explained. Then, an overview of electron transport in these materials is provided. The consequences of the resulting dynamic characteristics are also addressed. In the final part of this chapter, we will discuss about magnetic damping and spin pumping.

2.2 Magnetic Moments

The collective properties of the atomic magnetic moments are responsible for macroscopical behaviour. Short-range interactions between the moments can result in long range magnetic ordering, that gives rise to the measurable magnetic properties of the system. The origin of these magnetic moments and their interactions are described in this section.

2.2.1 Atomic Magnetic Moment

The magnetic moment of an electron is created when its spin, which represents its intrinsic angular momentum, is combined to the angular momentum of the electron's orbit around the atom. This results in the electron having a net spin-orbit angular momentum. In an atom, the total angular momentum (μ) by the gyromagnetic ratio (γ) or the Landẽ g-factor (g_0) is associated with the atomic magnetic momentum (J). Fig 2.1 illustrates an electron's angular momentum as a planet spinning on its axis and orbiting about a nucleus. The spin angular momentum is an intrinsic property of an electron. Since the electron is a fermion the spin angular momentum can be expressed as $\pm\frac{1}{2}\hbar$ where $\hbar$ is the reduced Plank's constant. The spin angular momentum is also generally referred to either spin-up ($\uparrow$, $+$) or spin-down ($\downarrow$, $-$). The sum of the spin (S) and orbital (L) angular momentum is [2];

$$S = \sum m_s, \tag{2.1}$$

and

$$L = \sum m_l. \tag{2.2}$$

where the spin magnetic quantum number is denoted by m_s while the magnetic quantum number for orbital angular momentum is represented by m_l. In an atom, the total angular momentum (μ) by the gyromagnetic ratio ($_\gamma$) or the Landẽ g-factor (g_0) is associated with the atomic magnetic momentum (J).

$$\mu_{tot} = -\frac{g\mu_B}{\hbar} J, \tag{2.3}$$

here μ_B is the Bohr magneton. The total angular momentum of the spin (S) and orbital (L) angular momentum is represented in figure 2.2. The intrinsic spin and orbital angular momenta combine to give the toal angular momentum via the spin-orbit interaction, described in the following section. In ferromagnetic materials, such as iron ($3.63\mu_B$), cobalt ($2.49\mu_B$), and nickel ($1.26\mu_B$), have an extremely high magnetic moment, whereas the magnetic moment in other materials is relatively low [3]. The sum of these contributions, $J = L + S$, can obtain the total angular momentum vector, $\vec{J}$, and the Landẽ g-factor, g, is given by,

$$g = 1 + \frac{J(J+1)+S(S+1)-L(L+1)}{2J(J+1)}, \tag{2.4}$$

J, L, and S are the magnitudes of $\vec{J}$, $\vec{L}$, and $\vec{S}$, respectively. Atoms that have all their electron shells filled have no net spin or orbital angular momentum, and as a result, they do not produce a net magnetic moment. We will discuss Hund's rules shortly, where this is explained in more detail. Also, the exchange interaction arises from the quantum mechanical principles that dictate the behaviour of electrons in atoms, this is explained in section 2.4.1.
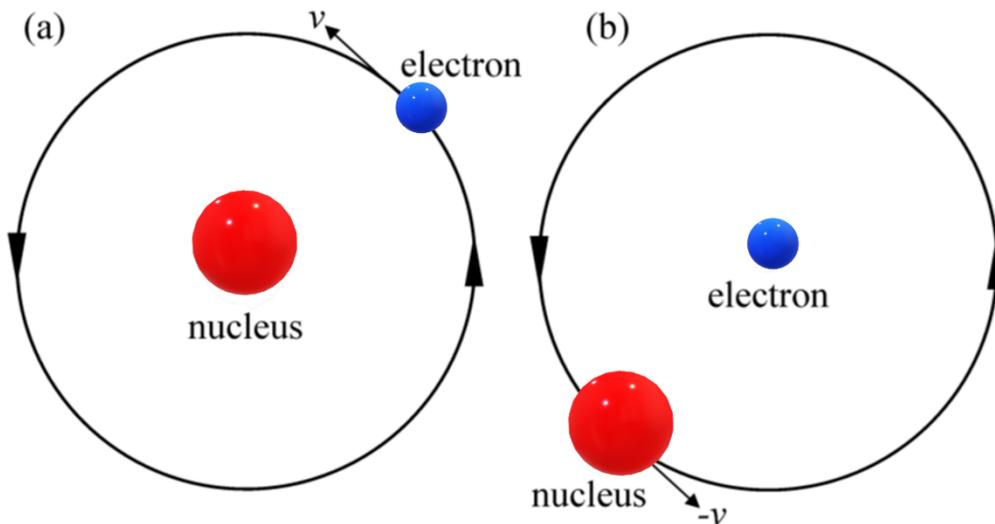
Figure 2.1. (a) An electron in orbit around a nucleus moving at velocity v relative to the nucleus's reference frame. (b) Compared to the electron's perspective, the nucleus orbits at a speed of -v relative to the electron.

2.2.2 Spin-Orbit Interaction (SOI)

The Spin Orbit Interaction (SOI) results from a relativistic interaction due to the relative motion of the electron and atomic nucleus. In the rest-frame of the electron, the nucleus's motion results in a magnetic field related to the orbital angular momentum ($\vec{L}$). When the positively charged nucleus orbits the electron, a positive current loop is produced and consequently, a magnetic field ($\vec{B}$) is created. As shown in Fig2.2, the nucleus orbits the electron forming a closed loop that representing the Spin Orbit Interaction. The energy of the electron in the magnetic field depends on the spin orientation through [3]. Thus, the changing of that energy can be written as:

$$\Delta E = -\vec{\mu_s}.(\vec{B}) \tag{2.5}$$

where μ_s is the spin dipole moment and $\vec{B}$ is the magnetic field. The symmetry of that crystal becomes important when atoms are placed on a lattice to form a crystal [4].
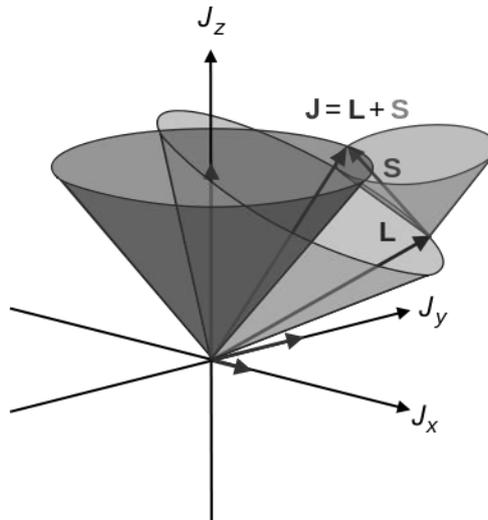
Figure 2.2. Illustrates the total angular momentum J, orbital L, and spin S. Cones form as a result of quantum uncertainty in measuring angular momentum components.

A screened potential for other electron states, such conduction electrons, leads to a reduced atomic number scale. In the heavy metals such as Pt, Ir, and Ta, the total SOI scaling is about Z^2 [4]. Shanavas et al. demonstrate how the strength of spin-orbit coupling changes between different atomic shells. This indicates that transition metals with 5d electron states at the Fermi energy, such as Pt, have a stronger spin-orbit interaction than metals like Au, which have s-states at the Fermi energy.

2.2.3 Hund's Rules

The net magnetic moment can be determined by considering how electrons occupy the ground state of the main orbitals while accounting for spin and orbital angular momentum as well as their interaction. The electrons' interaction and the magnetic moment in the materials are explained by Hund's rules [1, 5]:

1. The spin-spin energy is minimised as a result of the maximization of the total atomic spin $S = \sum m_s$

2. The maximum orbital momentum $L = \sum m_l$ value with the same S value is the most stable.

3. Consider a perturbation due to the SOI to find the total angular momentum J, if the shell is less than half full, $J = |L - S|$; however, $J = |L + S|$ if the shell is more than half full.

In the case of Co, it has 7 electrons in the 3d shell, which holds up to 10 electrons. With Hund's rules, the first 5 electrons in the 3d orbitals fill unoccupied m_l states (-2, -1,0,1,2) as spin up maximise L. The sum of these contributions provides L = 3, S = 3/2 and since the 3d shell is over half full J = 3/2 + 3= 9/2. These rules are valid for isolated atomic system; for the light metals other energy contributions can control over the SOI. The orbital angular momentum L=0 in Hund's rules, this is because of the crystal symmetry, making the potential (that causes the spin-orbit coupling) to differ from that of an isolated atom. The removal of rotational symmetry in a crystal means that the orbital angular momentum is no longer conserved and so averages to L=0.

2.3 Magnetic Materials

The macroscopic magnetic response of a material is the result of the interactions between microscopic magnetic moments of atoms. The interaction between these moments is facilitated by an exchange energy (J_{ex}). The magnetic materials can be categorised by their magnetic properties. In terms of susceptibilities, diamagnetic is small and negative due to current loops. When the atoms have a moment themselves, an additional paramagnetic term is positive and larger due to the moments gradually aligning with the field. In a ferromagnetism, the susceptibility is large and positive, and the field dependent magnetisation aligns with the field [5, 6]. Figure 2.3 shows a brief description of each material.
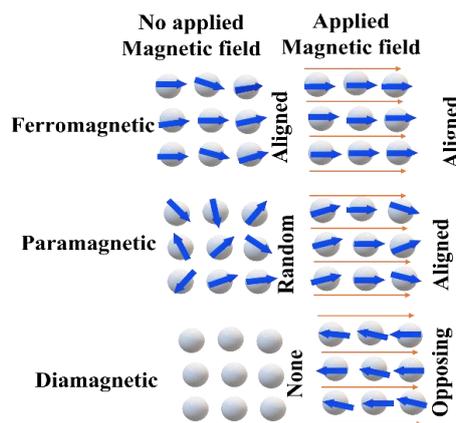
Figure 2.3. Ferromagnetic, paramagnetic, and diamagnetic materials

This section introduces some of the measurable parameters that rely on the net moment of a system before discussing the major classification of magnetic materials used in this study.

2.3.1 Magnetic Material Parameters

The magnetisation of a system of identical atoms is given by $M = n_a \mu_a$, where n_a is the number of dipole moments per unit volume and the μ_a is the magnetic moment of each atom. The system behaviour to an external field can be defined as [7],

$$\vec{M} = x_S \vec{H} ,\tag{2.6}$$

$$\vec{B} = \mu \vec{H} = \mu_r \mu_0 \vec{H}\tag{2.7}$$

where x_S is the magnetic susceptibility, the magnetisation per unit field. Magnetic permeability is another closely linked parameter of significance. Also, $\vec{B} = \mu_0 (\vec{H} + \vec{M})$ is the flux density in a system, μ_r is the relative magnetic permeability and μ_0 is the permeability of free space.

2.3.2 Diamagnetism

All materials generally have weak diamagnetic characteristics; however, when an external magnetic field is applied, a magnetic moment emerges to oppose the direction of the field and rises linearly with the field. The magnetisation behaviour as a function of field and temperature is illustrated in Figure 2.4. Typically, this can be interpreted as the external field interacting upon the orbital motion of the electrons, hence generating a current that opposes the external field. Even for full shells with L= 0, diamagnetism still occur [8]. This leads to a negative susceptibility which is temperature-independent and is generally small in comparison to para-magnetism and ferromagnetism [9].

Figure 2.4. Shows (a) the magnetisation of a diamagnetic material as a function of applied magnetic field (H) and (b) the diamagnetic susceptibility as a function of temperature (T)

2.3.3 Paramagnetism

As described previously, there is a net magnetic moment for atoms containing unpaired electrons. These moments are effectively uncoupled in paramagnetic materials, and they are aligned randomly with no net magnetization when the field is zero. Figure 2.5 illustrates field and temperature profiles coupled with indications of net magnetization due to the presence of an external magnetic field, which reduce the thermal motion of the moments. This causes a positive magnetic susceptibility, which according to Curie's law, $x_M = \frac{C}{T}$ where C is a material specific quantity, has an inverse temperature dependency [10].
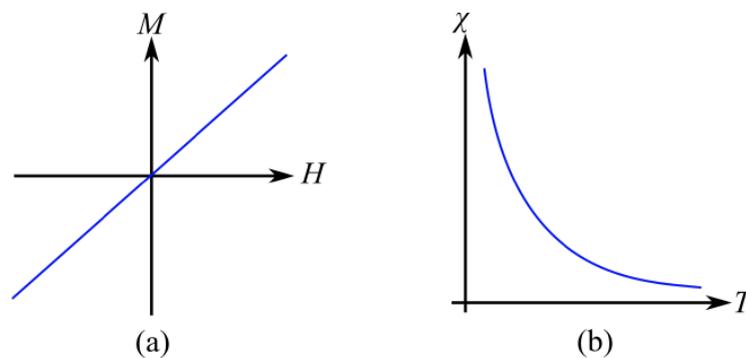
Figure 2.5. Demonstrations (a) the magnetisation of a paramagnetic material as a function of small applied magnetic field (H) and (b) the paramagnetic susceptibility as a function of temperature(T).

2.3.4 Ferromagnetism

The term "ferromagnetism" is used to describe a category of materials in which a net magnetisation exists even in the absence of an external magnetic field as seen in figure 2.6, in contrast to paramagnetism. Magnetic moments in atoms like to be aligned in a long-range due to a short-range coupling called the exchange interaction that encourages parallel alignment between neighbouring magnetic moments. The thermal energy is sufficient to overcome this interaction at high temperatures, and the material acts as a paramagnet above the Curie temperature [11].
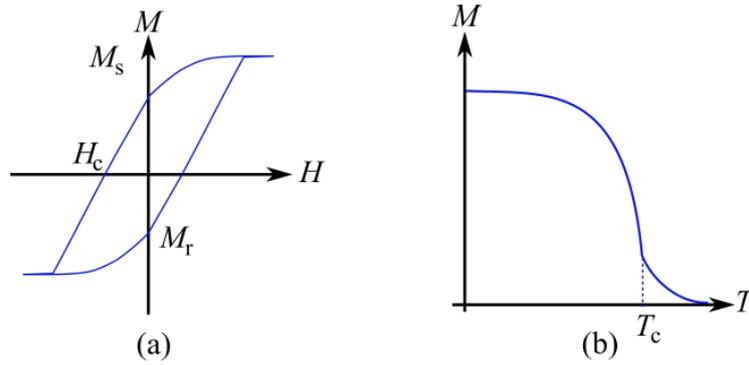
Figure 2.6. Demonstrations (a) the magnetisation of a ferromagnetic material as a function of applied magnetic field, forming a hysteresis loop and (b) the saturation ferromagnetic material as a function of temperature (T).

While exchange interactions do provide some degree of local ordering, other factors could lead to the magnetization direction to be nonuniform on a broader scale. The state known as magnetization saturation (M_s) can occur when a large external magnetic field is applied to a material. This causes the magnetic moments throughout the material to become aligned with the field. Removing the field results in a state known as magnetic remanence, where a net moment remains. When the field is reversed, the magnetization will reverse its sign when it goes through the point of zero magnetization and that is called the coercivity field, and the magnetic hysteresis loop is produced by completing a magnetic field cycle, the area enclosed by the loop is the energy dissipated during the cycle [12]. When an external magnetic field is absent or below the saturation level, magnetic moments in a material tend to arrange themselves in discrete regions called magnetic domains. They are separated apart by magnetic domain walls to decrease the system's overall energy by reducing its magnetostatic energy at the expense of increased exchange energy within the domain wall.

2.3.5 Antiferromagnetism

In ferromagnetic materials, the exchange is positive, which results in parallel spin alignment. However, in antiferromagnetic materials, a negative exchange energy produces a system in which neighbouring magnetic moments have an antiparallel arrangement of local magnetic moments. This results in the formation of an antiferromagnetic material. This pattern of behaviour is illustrated in Figure 2.7. When subjected to an external field, antiparallel moments will be unable to move apart from one another, resulting in a very small positive magnetic suscep-

tibility. Antiferromagnets, exchange interactions can be overcome by extremely high temperatures as they generate sufficient thermal energy. The Néel temperature (T_N) is the ordering temperature where this occurs in antiferromagnetic materials.
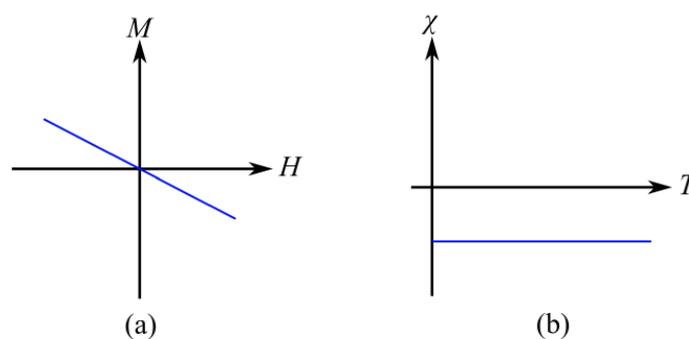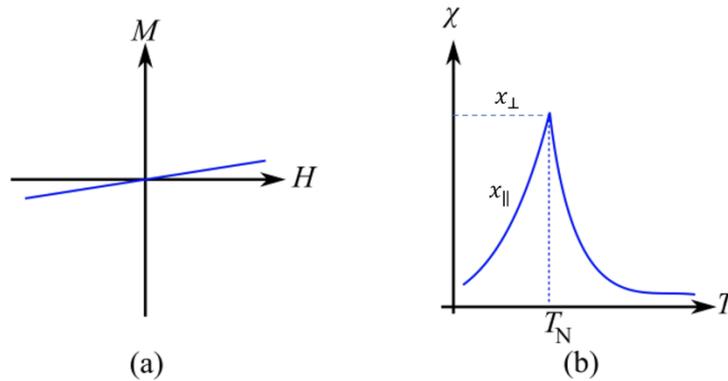

Figure 2.7. (a) The magnetisation of an antiferromagnetic material as a function of applied magnetic field, (b) the antiferromagnetic susceptibility as a function of temperature (T), and above the Néel temperature (T_N) the material will become paramagnetic.

2.4 Energy Contributions in Ferromagnets

The magnetic energy of a material can be defined as the sum of the energies associated with the various physical processes that lead to ferromagnetic behaviour which can be written as

$$E_{tot} = \int_V \varepsilon_{tot} \, dV, \tag{2.8}$$

E_{tot} is an energy and epsilon being the energy density: energy density, integrated over volume, gives energy. This is the total of the individual energy density contributions produced by the various contributing effects and is expressed as

$$\varepsilon_{tot} = \varepsilon_{ex} + \varepsilon_{Ze} + \varepsilon_{mc} + \varepsilon_{dem} + \varepsilon_{ms} + \varepsilon_{me.} \tag{2.9}$$

The various terms represent the exchange energy (ε_{ex}), Zeeman energy (ε_{Ze}), magnetocrystalline anisotropy energy (ε_{mc}), demagnetization energy (ε_{dem}), magnetostatic energy (ε_{ms}), and magnetoelastic energy ($\varepsilon_{me.}$). The fundamental origins and quantitative definitions for the various energy terms are discussed in the next subsection.

2.4.1 Exchange Energy

The magnetic arrangement of materials is caused by this energy. It is linked with the exchange interaction among nearby spins and written as

$$\varepsilon_{ex} = -2J_{ab}.\ \vec{S_a}.\vec{S_b}, \tag{2.10}$$

in this case, S_a and S_b are nearby spins. This exchange integral, J_{ab}, characterises the nature and intensity of the exchange coupling between spins. As a result of the parallel alignment of the spins, ferromagnetic order is formed if J_{ab} is positive and the triplet state has a lower energy. In contrast, antiferromagnetic ordering occurs when J_{ab} is negative because the spin singlet state has a lower energy, and the spins are antiparallel.

The sign of the exchange integral is related to the ratio of the interatomic distance D to the radius of the partially filled d-orbit, which was discovered through studies of the exchange integral in 3d elements by Slater and later by Bethe [12, 13]. This can be seen in Figure 2.8 by the Bethe-Slater curve, which successfully explains the antiferromagnetic ordering. Due to the high density of electrons at the Fermi level, the Coulomb repulsion in a 3D ferromagnet is larger than the kinetic energy. It should be highlighted that the Bethe-Slater relation is a simplified perspective of magnetic exchange and fails to explain more complicated magnetic behaviour.
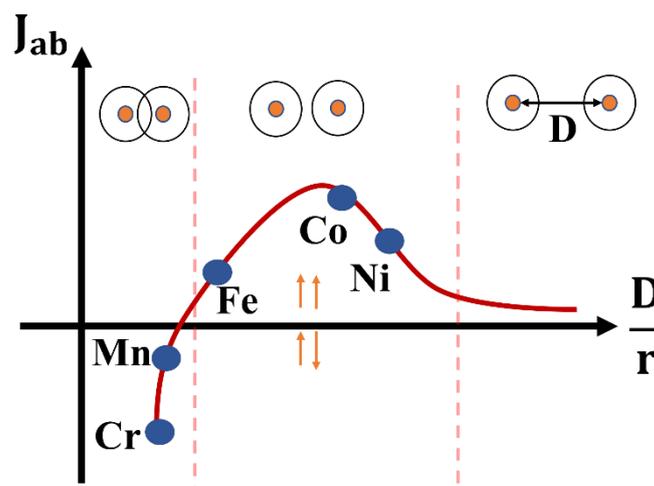
Figure 2.8. Bethe-Slater curve for the reliance of the exchange integral on the interatomic distance and the radius of a partially filled d-orbital.

2.4.2 Zeeman Energy

The interaction of magnetic moments with an external field produces a significant energy contribution in magnetic systems. Zeeman energy is the energy that arises from this interaction, and the energy density is given as

$$\varepsilon_{Ze} = -\mu_0 \overrightarrow{H_{ex}} \cdot \overrightarrow{M_s} \qquad (2.11)$$

where $\overrightarrow{H_{ex}}$ is the external magnetic field. Zeeman energy is minimum when the material's magnetic moment is aligned parallel to the field and maximum when it is aligned antiparallel.

2.4.3 Magneto-crystalline Anisotropy

The orientation of magnetic spin moments of the atoms in a material are related to the crystal lattice of the materials as a consequence of the SOI. The magnetisation of a material is determined by the direction favoured by its spin magnetic moment interaction with the electron orbit, due to the spin-orbit interaction and the crystal lattice. Some crystallographic orientations are more favourable for magnetisation alignment than others; these are called easy axes, while hard axes are those that need a strong magnetic field in order to fully align the magnetisation. Magneto-crystalline anisotropy is the term referring to this phenomenon. This energy is needed to switch the magnetisation from the easy axis to the hard axis overcoming the spin orbit interaction, in a single crystal. Anisotropy energies are always less than exchange energies [14].

To represent the energy of magneto-crystalline anisotropy, we use a power series expansion based on the angular separation of the magnetization direction and the easy axis. In materials such as Co that only contain a single easy axis which is perpendicular to the hard axes, the energy that is linked with the magneto-crystalline anisotropy can be expressed as

$$\varepsilon_{mc} = -K_1 \sin^2\theta + K_2 \sin^4\theta \qquad (2.12)$$

the first and second order anisotropy constants are represented by the coefficients K_1 and K_2, respectively, with K_1 being greater in magnitude K_2. Both coefficients have been demonstrated to be significantly temperature sensitive, declining as temperature rises and approaching zero before the Curie point.

2.4.4 Magnetostatic Energy and Shape Anisotropy

The term "magnetostatic energy" refers to the energy that is related with magnetic stray fields (H_s) and is created by a magnetic body. The magnetic dipoles and the related field are responsible for the creation of this energy through their interaction. The strong exchange interaction is always much greater compared to the magnetic dipole-dipole interaction. The magnetostatic energy density may be given as

$$\varepsilon_{ms} = \frac{\mu_0}{2} \overrightarrow{H_s} . \overrightarrow{M_s} \tag{2.13}$$

The magnetostatic energy is reduced by reducing the extent of the stray field and number of magnetic surface 'charges'. The direction of saturation magnetisation ($\overrightarrow{M_s}$) is typically opposed to the direction that $\overrightarrow{H_s}$ tends to go. The strength of the stray field is dependent on the size and shape of the sample [15]. In the absence of magneto-crystalline anisotropy, magnetisation can proceed in any direction over the surface of a spherical material, but along the longest axis of a non-spherical material, since this reduces the magnetostatic energy by reducing the number of surface charges. In a two-dimensional representation of the non-spherical form, the longest axis lies in-plane of the sample, while the shorter axis lies out of plane. Due to the material's anisotropy, magnetisation is easy axis, in the plane, parallel to the surface, whereas out-of-plane magnetisation is hard axis. As a result of dipole-dipole interactions, this phenomenon is referred to as shape anisotropy. The display of domains in ferromagnetic substances emerges from the balance between exchange energy, promoting the uniform alignment of magnetic moments, and magnetostatic energy, which is reduced when extensive external magnetic fields are prevented. This dynamic interplay drives the creation of magnetic domains and their accompanying boundaries, known as domain walls.

2.5 Band Theory of Magnetism

Physical characteristics of metals, semiconductors, and insulators are typically explained using the band theory, also known as the collective-electron theory [16]. Many of these materials' physical characteristics, such as magnetism, can be explained by using the principle of band theory, which is based on the electronic structure of these materials. Between 1933 and 1936, E.C. Stoner and J.S. Slater developed this theory to explain many material characteristics and

behaviours besides magnetic, such cohesiveness, elasticity, thermal conductivity, and electrical conductivity [17]. The atomic equivalent moment is expressed as the effective number of Bohr magnetons (n_{eff}). This value varies with the material and can be determined by:

$$n_{eff} = \frac{M_S}{n\mu B} \tag{2.14}$$

With n being the number of atoms per unit volume and where the saturation magnetisation M_S is at T=0K.

Any two electrons in the atom cannot have the same energy level, based on the Pauli exclusion principle. In order to maintain the Pauli exclusion principle, energy levels that contain more than two electrons, like the 3p shell, should split into additional sub-levels. Due to the significant splitting and overlapping of the sub-levels of the atoms, the application of this concept while creating a solid becomes more complicated when interacting with heavy transition metals where electrons extend to the 3d and 4s shells.

As isolated atoms come together, the energy levels of atoms merge to form energy bands. These bands can be quantified by the density of states which defined the number of states per unit energy per unit volume. In non-magnetic material the number of spin-up and spin-down electrons (and hence density of states) are identical [18].In a ferromagnet, some spin-down electrons at the Fermi level are expected to spin-flip into the spin-up band, causing a spin imbalance and a net magnetic moment in a ferromagnetic material in the absence of an external magnetic field, see Figure 2.9a. The quantity of electrons that spin flip can be thought of as raising the energy δE in the spin up channel, which is considered as the energy required for spin flip. The magnetisation (M) is calculated as

$$M = (n_\uparrow - n_\downarrow)\mu_B \approx \mu_B g(E_F)\delta E \tag{2.15}$$

where the spin polarisation is not equal to zero ($n_\uparrow - n_\downarrow \neq 0$). As a rise in kinetic energy, the spontaneous shift of electrons from spin-down to spin-up sub-bands in the absence of an external field can be understood. The $g(E_F)$ is the density of electronic states at the Fermi energy E_F. To determine the overall change in energy ΔE, the following formula can be used:

$$\Delta E = \Delta E_{K.E} + \Delta E_{P.E} = \frac{1}{2} (g (E_F) (\delta E)^2 (1- U g(E_F)) \tag{2.16}$$

here U represents the Coulomb energy, and the term $U=\mu_0\mu_B{}^2\lambda$ and $\Delta E_{P.E}$ is the potential energy. The only condition for spontaneous magnetization to happen is when the changing energy is less than zero.
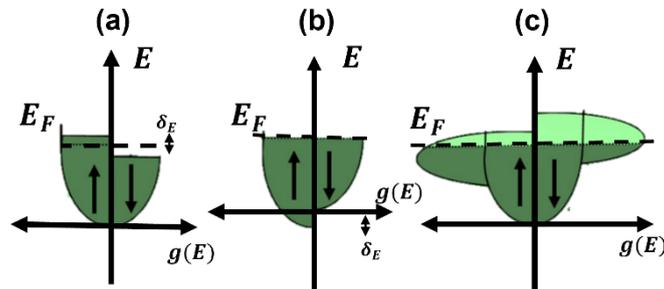
Figure 2.9. Schematic representation of the electronic density of states demonstrating the spontaneous splitting of energy bands in the absence of an external field (a) shows spins state (spin up/down) (b) band splitting as a result of spin flip (c) spontaneous magnetisation in 3d transition metals.

2.6 Magnetic Damping

In ferromagnetic materials, magnetic damping occurs when energy from the precessing magnetization is transferred to the lattice's microscopic thermal motion. Precession can be induced by varying the direction and magnitude of the applied magnetic field. The interactions between spin-waves (magnons) provide a variety of routes for energy dissipation. Energy can be transferred to magnon modes with different wave number k by scattering. The driven precession can be thought of as a uniform magnon mode with k=0, all moments (m) same phase at the same frequency, this is often referred to as the uniform precessional mode. The uniform mode can relax directly or can scatter. The uniform mode can scatter into non-uniform modes with k $\neq$ 0, while conserving momentum, by scattering from crystal defects and impurities [18]. When the uniform-mode energy and angular momentum is dissipated using various magnons, this is a new form of non-uniform relaxation, and this new form is known as two-magnons scattering.

One of the important aspects of ferromagnetic precessional damping is the intrinsic damping process associated with spin-orbit interaction, this is the dissipation directly from the uniform mode. Energy is dissipated to the lattice via the SOI, and this is described by the Kambersky damping process. This framework focuses on the change in the Fermi level and the two primary sources that contribute to overall damping. The concept of damped precession of the uniform mode was first described by Landau and Lifshitz [19]. The relaxation frequency is

related to the quantity determined by the Kambersky model, which is represented by effective field(H_{eff}), the magnetisation (M), and the relaxation frequency (λ). The damped precession, in terms of the relaxation frequency, is given by

$$\frac{d\vec{M}}{dt} = -\gamma\vec{M} \times \overrightarrow{H_{eff}} - \frac{\lambda}{M^2} \vec{M} \times \vec{M} \times \overrightarrow{H_{eff}},$$ (2.17)

where γ is the gyromagnetic ratio and $\overrightarrow{H_{eff}}$ is the effective magnetic field. A related phenomenological explanation of damped precession was achieved by Gilbert. The dimensionless parameter of Gilbert damping is α , where the quantity determines dissipation [20]. The Landau-Lifshitz-Gilbert (LLG) equation can be expressed as

$$\frac{d\vec{M}}{dt} = -\gamma\vec{M} \times \overrightarrow{H_{eff}} + \alpha \left(\vec{M} \times \frac{d\vec{M}}{dt}\right).$$ (2.18)

In the LLG equation, the first term represents magnetization precession; the negative sign is related to the determination of the applied torque direction on $\vec{M}$, which indicates the precession direction. The gyromagnetic ratio is defined as positive to avoid any confusion regarding the sign. Assuming a magnetization $\vec{M}$ of constant magnitude, the second component of the LLG equation reflects the perpendicular damping force on $\vec{M}$, as seen in Fig.2.10.
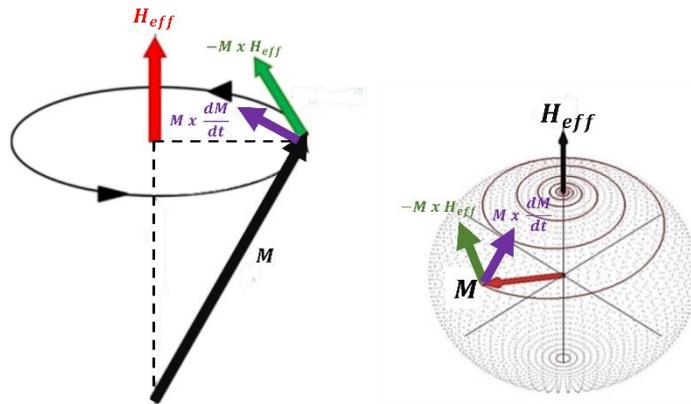
Figure 2.10. Illustration of the Landau-Lifshitz-Gilbert model for the magnetization damping process.

Ferromagnetic resonance (FMR) is used to characterise magnetic materials in terms of their effective damping and magnetisation [21]. Many studies on the Gilbert damping have been carried using the phenomenological LLG equation, and it is now well understood [22]. When the precession is driven by a microwave field, the absorption of microwave power into

the sample can be used to extract information on the damping. That absorption has a Lorentzian profile when the measurement is taken at a constant frequency, as a function of applied the magnetic field. The Kittel equation describes the relationship between the magnetic field and frequency at which resonance occurs. Therefore, the frequency and excitations can be fitted by the Kittel equation. The magnetic field swept absorption line-shape full width half maximum (FWHM), which is determined by the resonance linewidth (ΔH), frequency (f), and ΔH_0, is used to separate the intrinsic and extrinsic damping contributions.

$$\Delta H = \Delta H_0 + \left(\frac{4\pi\alpha}{\gamma}\right)f \tag{2.19}$$

$$f = \frac{\gamma}{2\pi}\sqrt{H_{\text{eff}}(H_{\text{eff}} + 4\pi M_{\text{eff}})} \tag{2.20}$$

Where H_{eff} is the effective field, M_{eff} is the effective magnetisation and γ is the gyromagnetic ratio and the magnetic damping is α. The effective damping contains the total damping contributions, intrinsic and extrinsic damping. Therefore, the intrinsic damping is the first mechanism of the damping that is defined as Gilbert's relaxation of the uniform mode precession. Moreover, this is described in the Landau–Lifshitz–Gilbert (LLG) equation by the term of damping [23]. On the other hand, the ferromagnetic inhomogeneity is linked to the extrinsic damping effects, which can be induced by a variety of variables including sample thickness, surface non-uniformity, and crystalline variations.

Previous studies have focused on ferromagnetic resonance and the damping of ferromagnets, such as Fe, Ni, and Co. These materials have either been studied on their own or have been coated with other types of materials. The value of damping can be changed, and surface oxidation avoided by placing a layer of material on top of the FM material. Some materials, like Cu and Si, are thought to have a minimal influence on damping an FM material when used as capping layers, hence careful material selection is required for studying magnetic damping [24, 25].

2.7 Spin-pumping and spin-mixing conductance

Spin pumping, also called spin injection, is the process by which a spin current is injected into the NM layer to enhance the interface. This spin current is the result of the magnetization dynamics. Spin-pumping is the process of producing a spin current in a material using Ferromagnetic Resonance (FMR). When a ferromagnetic (FM) layer is in contact with a non-magnetic (NM) layer and is excited with a microwave, spin-current is transferred across the interface [26]. Energy and angular momentum are being transferred from the ferromagnet's precessing magnetization via spin pumping onto the adjacent non-magnetic layer. Changes in FM and NM layer structure caused by changes in crystalline structure have a significant impact on spin pumping. Due to the spin-orbit interaction, the spin-current in the non-magnetic layer can relax and as the contribution to the damping of the magnetisation precession in the ferromagnet as a result of this relaxation has the same symmetry, and frequency dependence, as the Gilbert damping this is often considered to be an 'intrinsic' damping contribution. A schematic of the spin-pumping process is shown in figure 2.11. The spin-orbit interaction, which enables spin-flip scattering, is responsible for the relaxation in the non-magnetic layer. For the purpose of calculating the spin-current density at the interface

$$j_s^0 = j_s^{pump} - j_s^{back} \, , \qquad (2.21)$$

the density of the flowback spin can be described by the spin-circuit theory, which can be stated as

$$j_s^{back} = \frac{1}{4\pi}[\ g_{\uparrow\downarrow}^r \ \mu_s(x=0) + g_{\uparrow\downarrow}^i \ m \cdot \mu_s(x=0)]. \qquad (2.22)$$

Here, $g_{eff}^{\uparrow\downarrow}$ is the interface mixing conductance and that will be described in the next section. The spin accumulation is $\mu_s = \mu_\uparrow - \mu_\downarrow$ and $\hat{m}$ represents the unit vector of magnetization. Therefore, the Gilbert damping parameter (α), which is dependent on the ferromagnetic thin-film thickness (d_{FM}), the Bohr magneton (μ_B), the bulk intrinsic damping (α_0), and the g-factor, can be used to calculate the spin pumping. When the backflow effectively acts as an additional source of damping for the ferromagnetic layer. Hence, when a ferromagnetic layer is in contact with a good spin sink layer, the damping in the ferromagnet can be significantly enhanced due to this spin pumping effect.

$$\alpha = \alpha_0 + (g\,\mu_B/4\pi m d_{FM})\, g_{eff}^{\uparrow\downarrow} \qquad (2.23)$$
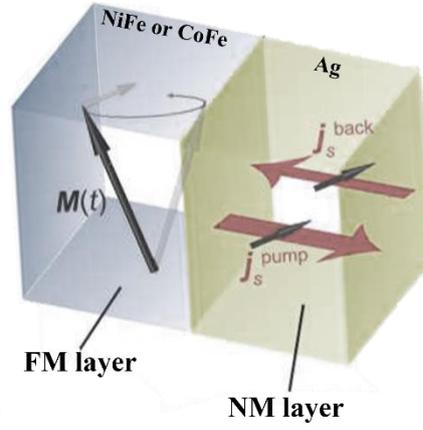
Figure 2.11. A schematic illustration of a pumped spin current and a backflow spin current in a FM/NM bilayer film [25].

The term of spin-mixing conductance counts the spin current that crosses the nearby non-magnetic and describes the spin-current ability to cross through the interface to relax within the non-magnetic layer. Moreover, spin-mixing conductance can be considered having both a real part, due to direct transmission with and without spin-flip at the interface, and an imaginary part related to spin transmission with a precession about the local magnetisation at the interface. The conventional spin-pumping theory shows the relaxation of spin current in the NM layer by the spin-mixing conductance which is typically considered as property of the NM material [26]. As illustrated in fig2.11, various events occur individually on the FM / NM interface, including the interaction of the FM and NM electron energy bands, diffusion of the spins pumped in the NM layer, and backflow into the FM layer, or decay of the injected spin. The pumped spin-current in the NM layer relaxes over a length-scale termed the spin diffusion length (λ_{sf}). This influence can be measured experimentally by measuring the resistance and quantity of a spin current that indicates the flow of the remaining spin after crossing the interface into the NM layer [34]. The spin-orbit interaction of the NM layer is linked to the value of the spin diffusion length. The damping enhancement via spin-pumping is understood in a simplistic fashion, but there are many details that are not yet fully understood.

Summary

The fundamental processes underlying the static magnetic properties of thin-film systems, as well as the fundamental sources of magnetism, have been described. We have delved into the origins of magnetic moments and explained how their configuration can serve as criteria for material classification. Furthermore, we have introduced the topic of magnetism induction in non-magnetic substrates upon interfacing with magnetic ones. In addition, we have studied the energetic constituents inherent in ferromagnetic structures, and subsequently, have illustrated on the resultant material typologies from such interactions. Finally, we have explained the phenomena of magnetic damping and the intricacies of spin pumping. In this next chapter, we will transition from magnetic principles to the methodologies behind material fabrication and the analysis.

Chapter 3. Sample Growth and Structure Analysis

3.1 Introduction

The experimental techniques and processes used to produce and structurally characterise thin film magnetic systems are discussed in this chapter. The samples in this investigation were grown using magnetron sputtering in an ultra-high vacuum deposition chamber, and various mechanisms of film growth are explained. Lastly, X-ray reflectivity (XRR) is discussed; this technique allows structural information to be determined about layers and interfaces buried within the multilayer thin film structures. Furthermore, the XRR data were fitted with a structural model for the sample, and the fitting process is presented.

3.2 Sample Preparation

The samples used for this work were generally deposited onto a silicon wafer topped with a 100nm layer of SiO_2 for the purpose of electrically isolating the metallic thin film from the semiconductor substrate. In the preparation area, the samples are cut and cleaned, and a diamond cutter was used to cut the wafer into appropriately sized pieces and label on the back of each piece. After cutting, the cleaning process took place in a fume hood, putting the sample into a beaker and immersing the sample in acetone to degrease and clean the sample in an ultrasound bath. A gas gun was used to remove the remaining acetone. The same cleaning procedure was repeated but instead of acetone, isopropanol was used. Isopropanol removes any residue of acetone, which can contaminate the vacuum growth system. The samples were dried with a N_2 gas gun and then transferred to a storage container before film deposition.

3.3 Magnetron Sputter Deposition System

All samples in this work have been created using an ultra-high vacuum (UHV) Mantis QPrep500 sputtering deposition system which provides DC source for growth of conducting materials and RF power sources for non-conductive target materials. The two main parts of the sputter system are the deposition chamber and load-lock. The deposition chamber has a base pressure of 5×10^{-9} Torr (6.67×10^{-7} Pa) and is separated from the load-lock by a gate-valve such that the load-lock can be used to transfer samples in and out of the deposition chamber. A

rotary pump and two turbo pumps are linked to the main chamber. The samples can be transferred from the load-lock chamber to the main chamber under working conditions by means of the transfer arm to be placed on the sample rotating stage located at the top of the main chamber. The system consists of five sputter sources, each connected to a gas line, water line, and power source. A quartz crystal microbalance (QCM) measures the growth rate of thin films. To specify the time of deposition and hence the layer thickness, a computer will control the opening and closing of shutters for all material targets. Fig3.1 shows the Mantis QPrep500 sputtering system with indicated main features.
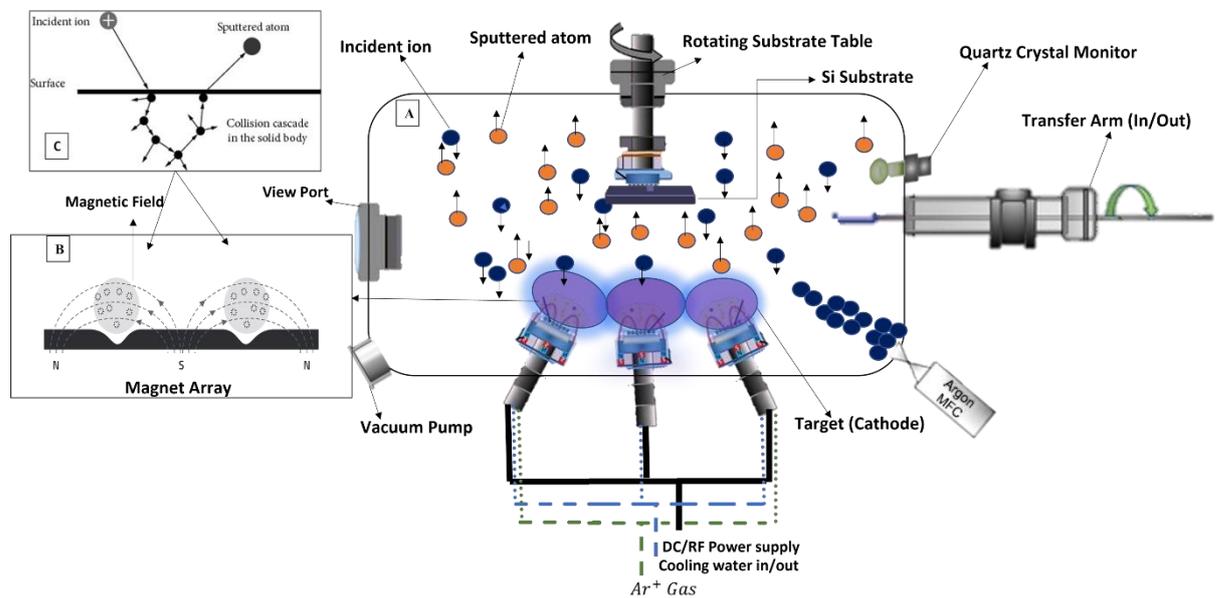

Figure 3.1: A diagram of a typical magnetron sputtering setup. (A): The entire magnetron sputtering vacuum system is displayed, including the target and rotating substrate. (B): the configuration of magnetic fields utilised to contain the Ar plasma. (C): the process of transferring momentum from an Ar^+ ion to a target material, leading to ejection of a target atom.

A RF power supply and DC supplies are used to power the five magnetron sources. At the same time, both DC and RF might be active to create alloy samples. In such cases the alloy composition is estimated from the deposition rate for each individual target, which is computed using the QCM. The DC current was 75 to 100 mA, and the RF power was 50 to 75W for all samples grown in Durham. Typically, Co and Pt targets are sputtered using DC magnetron sputtering. The typical Ar gas pressure was 1×10^{-3} Torr [27-29].

The discovery of sputtering in 1852 by W. Grove [30] revolutionized thin film production by utilizing energetic particles that collide with a solid surface, leading to the expulsion of atoms or molecules. This process has become a vital technique across multiple industries, including electronics, solar cells, optical coatings, and magnetic storage media. Researchers can exert precise control over film properties by adjusting factors such as sputtering power, gas pressure, and target-substrate distance. Applicability to a wide range of materials, and easily depositing multilayers and alloy samples are the most significant advantages of the sputtering process. During the deposition process, the DC bias voltage creates the positive ions in the plasma, which are accelerated to the target cathode due to the dc bias and the sputtered atoms travel to the sample stage above the target. After the emitted atoms reach the substrate, the thin-film surface begins to form itself by binding to the atoms with the substrate. To avoid damage to the target, water cooling is applied as the sputtering process increases the target temperature. In magnetron sputtering the targets are mounted onto a metal cathode which contains a magnet array. The magnetic field confines electrons close to the target surface, which collide with neutral Ar atoms creating further ions. The interaction between the magnetic field and the Ar^+ ion generates a dense plasma above the target surface.

In DC magnetron sputtering, a constant negative bias voltage is given to the deposition target, which operates as one electrode, while a surrounding earth shield acts as the other. The voltage ionises the precursor gas, generating the plasma and ions needed for the sputtering process. To produce a plasma, the target material used for film deposition via DC sputtering must be electrically conductive. The Mantis sputtering system used in this research project is seen in Fig. 3.2. Within the magnetron sputtering, a capacitively connected RF power supply is used to sputter non-conducting target materials. When the RF power frequency exceeds the ion plasma frequency, a continuous negative bias is formed on the target electrode which enables sputtering without detrimental build-up of surface charge on the insulating target [31].
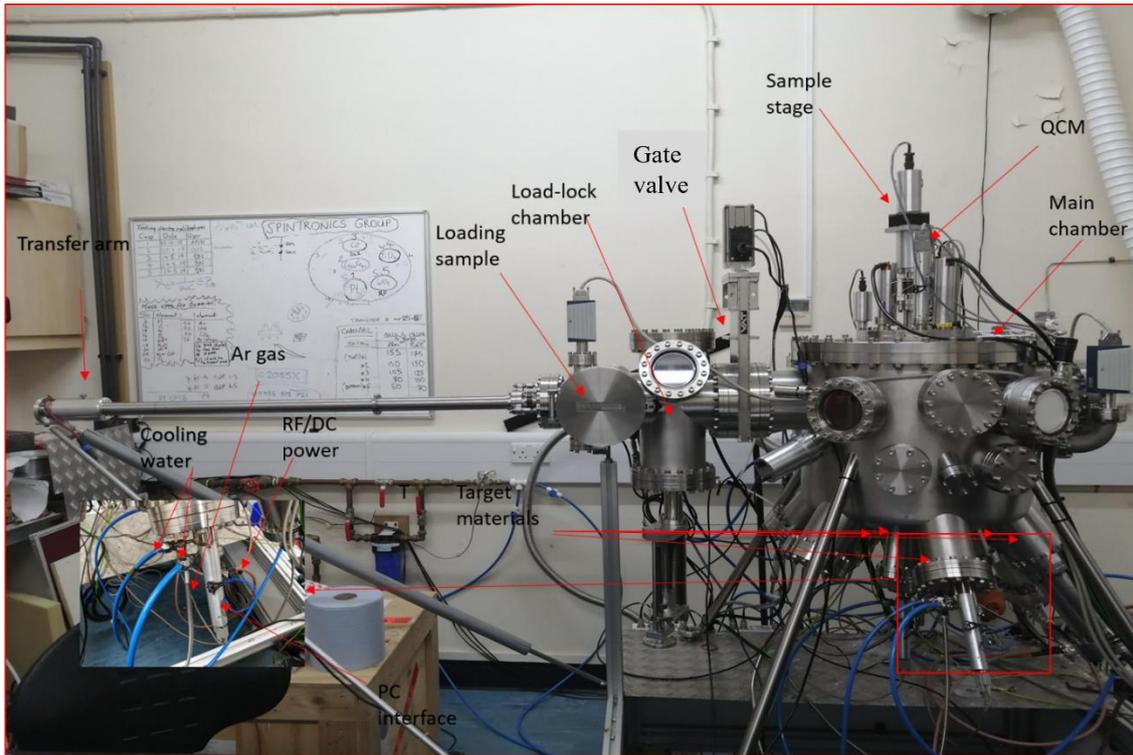
Figure 3.2: An overview of the Mantis Qprep500 sputtering machine in the lab, with the key components labelled.

3.4 Growth Modes of the Thin Film

The first step in forming any material layer on a substrate is to deposit sputtered atoms. The surface energies of the substrate and the target materials that adsorb onto the surface control the structure of the thin film. Thin-film layers are formed in three different ways, which are referred to as growth modes. These three modes are all linked to the atom-to-atom bonding strength between the deposited atoms. The initial mode of epitaxial layer growth, known as Frank-van der Merwe growth, is dependent on the strength of the bonds between the deposited atoms and the substrate atoms. When the bonding strength is sufficiently strong, the deposited atoms organize themselves into a monolayer that aligns with the lattice of the substrate. This results in the formation of a well-defined epitaxial layer, where the deposited atoms exhibit a uniform crystal structure. The ability of the deposited atoms to form these ordered layers is facilitated by their strong affinity for the substrate surface. The success of Frank-van der Merwe growth is directly influenced by the bonding strengths that allow for the controlled arrangement of atoms in epitaxial layers [32]. The island growth mode is the second form of deposition, in which atom-atom bonding strength is significantly more powerful than atom-substrate bonding strength. This mode begins with atoms associating with others, forming islands in separate areas on the substrate, and then these islands join to form the thin-film layer. Figure 3.3

demonstrates the formation of these modes when the thickness of the thin-film layer is gradually increased. Island merging occurs during the process of thin film growth, where islands or clusters of atoms come together to form a continuous film. When these islands merge, they often do not have the same crystallographic orientation, which means that the crystal lattice of one island may be misaligned with the lattice of another island [31] leading to the formation of a grain boundary.
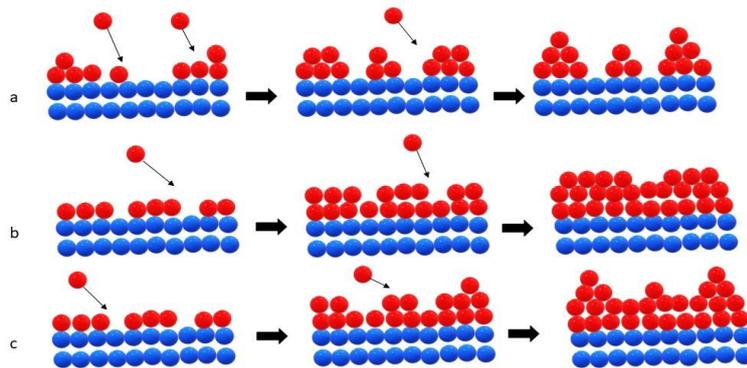
Figure 3.3: Thin-film growth modes (a) Volmer-Weber island growth, (b) Frank-Van der Merwe layer-by-layer growth, and (c) Stranski-Krastanov layer plus-island growth are demonstrated.

The third mode, known as Stranski-Krastanov growth mode, is a combination of layer-by-layer and island growths. This mode begins with the layer-by-layer growth method until a full monolayer covers the substrate, after which island growth completes the layer [33]. The third growth mode allows relaxation of lattice strain. Different surface structures should be induced as a result of various growth modes. As film thickness increases, changes in crystal structure might occur within a layer or even between two layers. A considerable influence on the crystal structure of the thin-film, and hence the magnetic properties, might be caused by depositing of various thicknesses and capping layers [33, 34].

3.5 The Structure of Materials

When a unit cell repeats to create a lattice structure, it forms a crystalline structure [34, 35]. The body-centred cubic (BCC), face-centred cubic (FCC), and hexagonally close packed cubic (HCP) are the three major metallic unit cells corresponding to the materials used in this work. Metals like Fe and W, exhibiting a BCC structure, Al, Cu, CoFe, Ag and Au featuring a FCC structure, as well as Ti and Zn with a HCP structure, serve as distinct examples of the broad range of materials associated with each type of unit cell. These instances highlight the fundamental role the crystal lattice plays in shaping the unique physical and chemical properties inherent to different metallic substances. The significant structural difference between FCC and HCP is the layering of each monolayer on top of others. The FCC structure sets among three layers while HCP structure cycles among two layers. All these structures are shown in figure3.4.
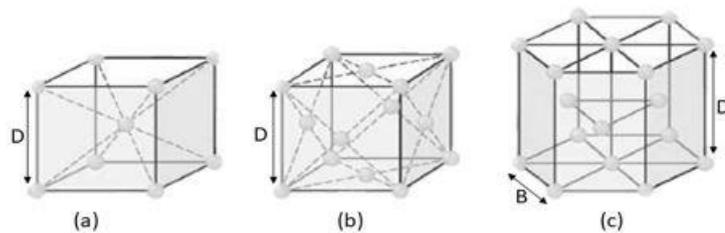
Figure 3.4: The metallic crystal structure:(a) body-centred cubic (BCC), (b) face-centred cubic (FCC), and (c) hexagonally closed packed (HCP).

3.6 X-Ray Reflectivity

X-ray reflectivity is a technique used to study the surface and interface structure of thin films or multi-layered structures. It is a surface-sensitive analytical procedure for characterising thin layers among multilayers samples, where the film thickness varies [36-39]. According to the law of Fresnel reflectivity, the intensity of the reflected beam is influenced by constructive and destructive interference and is further impacted when the interfaces are not perfectly smooth and sharp. The interference fringe regions are related to the film thickness by the modified Bragg equation.

As a result of the different electron concentrations on opposite sides of an interface between different materials, x-rays will be refracted and reflected at such an interface. The refractive (n) can be expressed as

$$n = \frac{c}{v} = 1 - \delta + i\beta , \tag{3.1}$$

where c is the speed of light and v is the speed of light in the material. The dispersion coefficient (δ), which is linked to the wavevector of the incident beam ($\vec{k}$) and the electron density of the material (ρ). The absorption coefficient (β) is responsible for the attenuation of the propagating photon beam. The β value is known to be extremely small, on the range of $10^{-6} - 10^{-8}$, and the value of δ is related to the speed of light in the material relative to its speed in a vacuum. n is less than 1 and v in the material is larger than the speed of light, c. These values are physically reasonable if v represents the phase velocity rather than the group velocity [40]. Fig. 3.5 displays the specular x-ray scattering geometry for a single layer with refractive index as stated. The sum of the refracted and reflected amplitudes equals the total incident beam amplitude. The critical angle θ_c, at which total external reflection occurs, can be determined using Snell's law. The total reflection is external since the refractive index of the material is < 1 in contrast to a prism which has total internal reflection since the refractive index is > 1. This law links the incidence and refraction angles using refractive indexes. The requirement for total reflection is $\theta_t = 0$,

$$n_0 \sin \theta_i = n_1 \sin \theta_t, \tag{3.2}$$

$$\theta_c = \sin^{-1} \left(\frac{n_1}{n_0} \right) \tag{3.3}$$

The critical angle θ_c for most metals, and Cu K-alpha x-rays is typically below 1 degree. The critical edge itself is determined by the electron density in the region of the sample surface, so the surface layer can have an impact on the reflectivity profile. When an x-ray beam propagates through a multi-layered sample, refraction and reflection occur at each interface [41]. The complexity of the equations rises as the number of layers and interfaces in the sample structure increases.
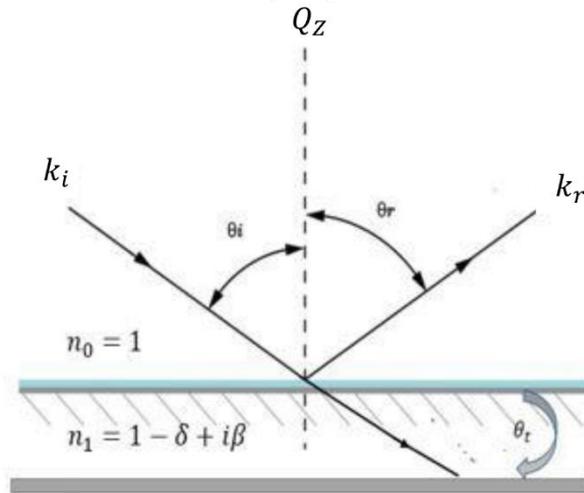
Figure 3.5: Schematic diagram of the measurement geometry for x-ray reflection from a single layer with refractive index n_1. The incident x-ray in general is partly transmitted and partly specularly reflected with a scattering vector Q_Z.

Beyond the simplest modelling, multiple reflections between upper and lower interfaces can further modify the reflectivity, particularly close to the critical edge.

3.6.1 Reflection from a Thin-Film for a single layer

The basic processes of reflection and refraction from a single interface are described previously. These processes are repeated in each interface of a thin film. The vacuum around the thin film has a refractive index of n_0, followed by the first layer of the film, which has an index of n_1, and the substrate, that has an index of n_s. There is no influence on the total intensity of the reflecting beams beyond the substrate layer, which can be considered to be semi-infinite. Once x-rays reach a thin film at a particular angle, in general a series of reflections can occur from both the top and bottom of each layer. The combination of the reflection and transmitted intensities for a thin film made of multiple layers with different electron densities is given by $R = |r|^2$ and $T = |t|^2$, where r is the reflection amplitude and t is the transmission amplitude. The reflectance of a simple bilayer structure is provided by the initial reflectance and subsequent from the transmitted waves, assuming perfect interfaces, as seen in figure 3.6.
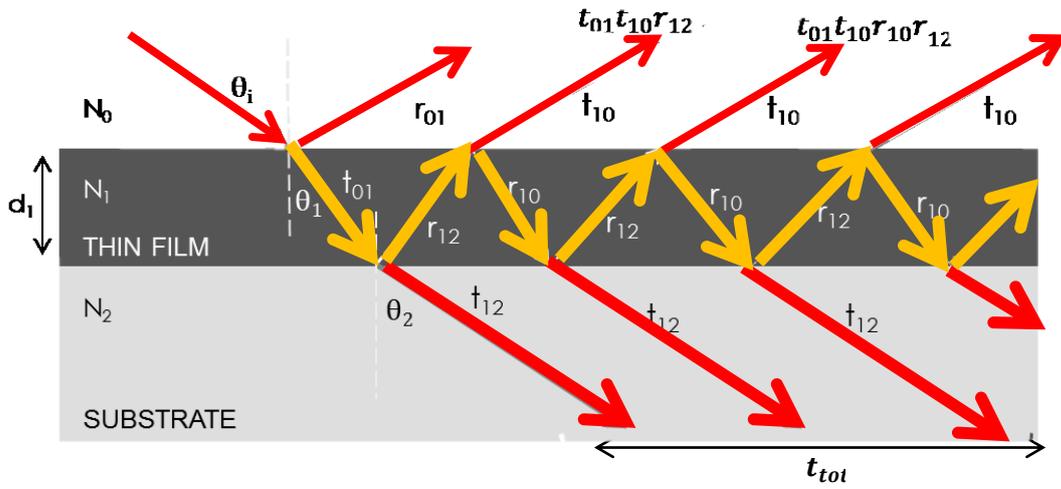
Figure 3.6: Diagram example of x-ray interactions with a single layer above the substrate layer as used for total reflection calculation of the input x-ray beam.

From the incident x-ray beam to the (r) and transmitted (t), the total reflected x-ray intensity (r_{t_0t}) can be determined:

$$r = r_{10} + t_{01}t_{10}r_{12}p^2(r_{10}r_{12}p^2).$$
(3.4)

The layer density assumed to be homogenous in this equation, which simplifies the calculation. The reflection amplitude is linked to the phase factor $p^2 = e^{(i\,dQ)}$. The formula relates to the layer thickness, d, and scattering vector, Q, which is related to the wavevector k_1 in the layer,

$$Q = 2k_1 \sin \theta_i.$$
(3.5)
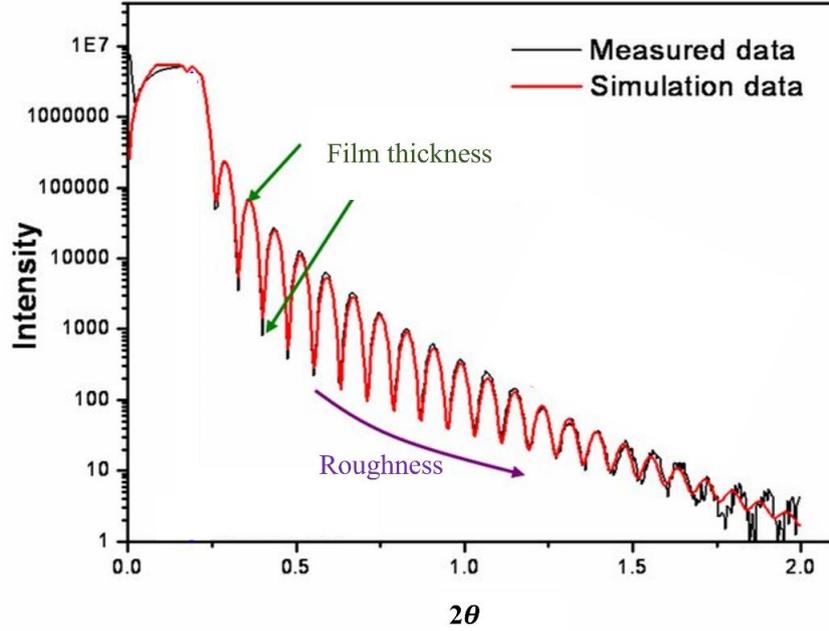
Figure 3.7: Reflectivity of a 10nm NiFe film deposited on an SiO_2 substrate is being investigated. Also, there is a fitting analysis that considers the film's thickness and roughness.

The x-ray reflective profile of a NiFe film formed on a SiO_2 substrate is in figure 3.7. Interference between x-rays reflected of the surface of thin-film multilayers and the interface between thin film and substrate appear as oscillations known as Kiessig fringes in the reflectivity profile. Kiessig discovered these oscillations in 1931, and thicker films have shorter period oscillations [42].

3.6.2 Reflection from a Thin-Film for a multilayers sample

The reflected x-ray intensity from a thin film is determined by various parameters, including the number of layers, thicknesses, and interfaces between the layers. For a multi-layered thin film, the total reflected amplitude can be determined using Parrat's recursion formula [43],

$$r = r_{10} + t_{01}t_{10}r_{12}p^2 + t_{01}t_{10}r_{12}r_{10}r_{12}p^4 + \cdots$$

$$= r_{10} + t_{01}t_{10}r_{12}p^2 \sum_{m=0}^{\infty} (r_{10}r_{12}p^4)^m \quad ,$$

(3.6)

For a basic bilayer sample, under the assumption of perfect interfaces, the determination of reflectance integrates both the initial reflectance and the succeeding reflections originating from the transmitted waves. This concept is graphically embodied in Figure 3.8.
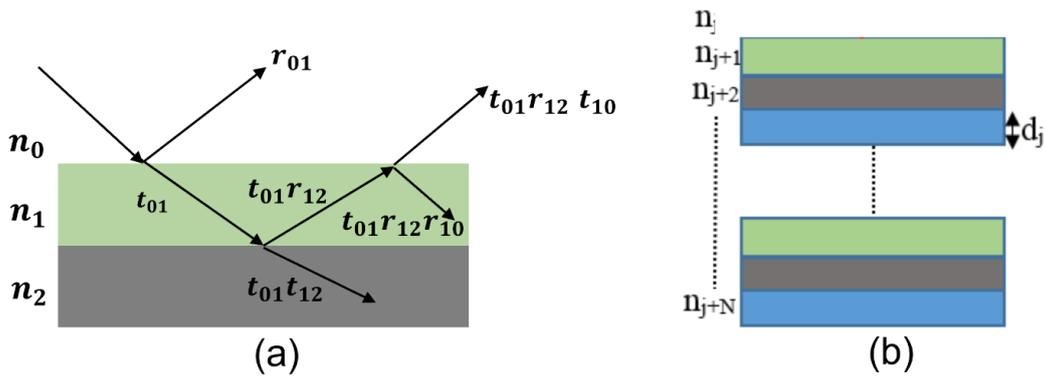
Figure 3.8: (a) Diagram illustration of reflected and transmitted x-ray in a multiple layer sample. (b) Schematic of the interface notation used in Parratt formalism.

Additional layers can be treated using paratt's recursive formalism [44], in which each additional layer, j has a corresponding refractive index, n_j and thickness d_j. Figure 3.6b demonstrates this layout. The reflectivity is then found recursively for any interface. As a result of phase variations in reflected beams, both constructive and destructive interference phenomena take place, leading to the formation of interference fringes that vary with the incident angle. In cases involving a specific film thickness, the principle of constructive interference associates with Bragg's law,

$$2d \sin(\theta_i) = m \lambda \qquad (3.7)$$

where m is an integer fringe number and λ is the wavelength. These fringes, known as Kiessig fringes, display variations that are intricately tied to alterations in the angle of incidence, as shown by the following expression:

$$\Delta\theta_i = \frac{\lambda}{2d} \ . \qquad (3.8)$$

An illustration of these fringes is provided in Figure 3.9 (a), demonstrating a single layer of CoFe. This figure indicates that an increase in film thickness results in a reduction of the fringe spacing. In the case of more complex structures, multiple periods of Kiessig fringes may be observed. Figure 3.9b provides an example of such Kiessig fringes for a multi-layer sample.
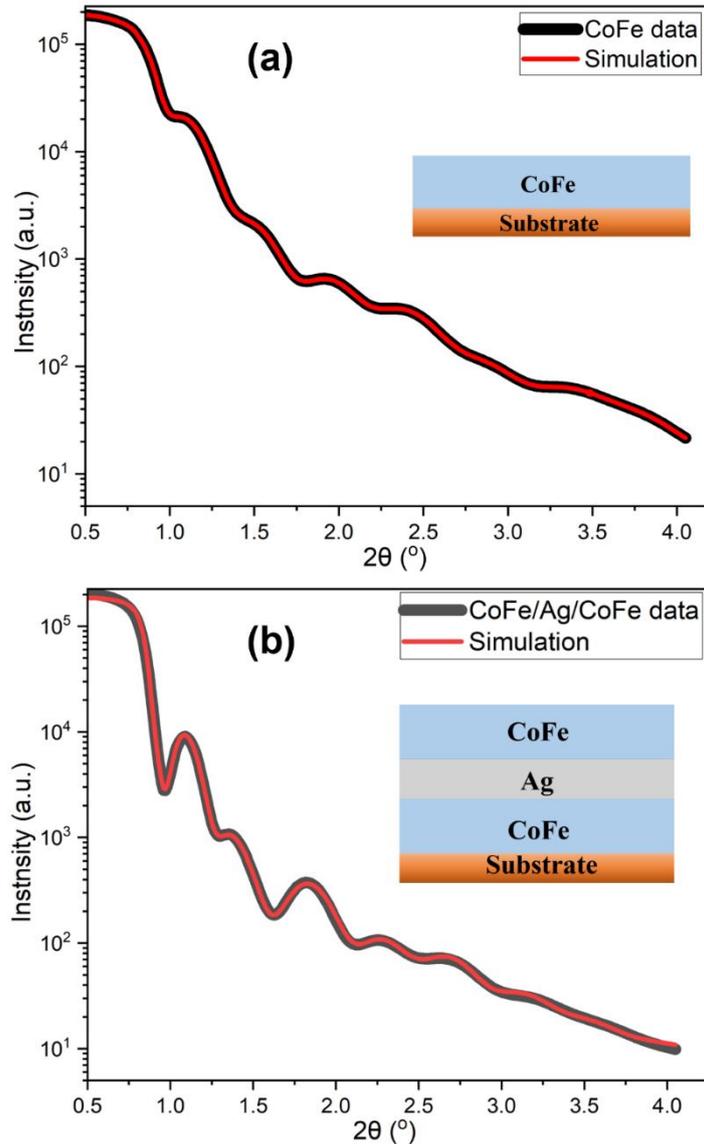
Figure 3.9: (a) Simulated XRR patterns for a single layer of CoFe (10nm) Thin Film and (b) XRR data for a complex multi-layered sample containing CoFe 10 nm/ Ag 7 nm / CoFe 10 nm layers.

Additionally, as x-rays traverse through a thin film, their intensity undergoes reduction or attenuation. As x-rays travel through a thin film, the intensity of the x-rays is attenuated in relation to the path length within the film (d_{path}). The path travelled through the thin film varies as the incident angle increases beyond the critical angle. To understand the role of layer density, it is crucial to investigate its impact on the calculation of reflection (r) and transmission (t) coefficients at each interface. Calculated using Fresnel's laws, these coefficients rely on the scattering length density a value derived from the actual density of the layer [45].

Handling a layer with non-uniform density presents unique challenges. A widely adopted strategy involves modelling it as a sequence of thinner, uniform-density sublayers, or slabs. This approach enhances the precision of modelling the reflectivity behaviour of the non-

uniform layer. It simplifies the analysis by allowing each uniform-density sublayer to be treated independently, contributing to a more accurate overall picture of the thin film's structural properties. In the case of a layer within a thin film exhibiting non-uniform density, it is often more effective to model it as a succession of thinner sublayers, each boasting uniform density. This methodology involves assigning each sublayer a uniform density representative of that portion of the original layer's non-uniform density [44]. Such an approach fosters a more accurate estimation of the thin film's total reflected amplitude.

During an x-ray reflectivity experiment on a multilayer thin film, the procedure typically involves capturing the reflected intensity in relation to the incident angle. This data allows for the generation of a reflectivity curve. Subsequently, an algorithm is applied to adjust the parameter (thickness, density, and roughness) of each layer in the model, aiming for the best possible match with the experimental reflectivity curve. This task usually involves an iterative optimization process to the best fit, which ultimately sheds light on the thin film layers' structure and properties. The process of fitting XRR data involved using specialized software specifically created for XRR data analysis. In general, widely used software such as GenX was utilized for this purpose. These software applications utilize mathematical models to analyse the experimental XRR data and derive essential structural details about the sample, including layer thickness, density, and roughness. The fitting process involves adjusting model parameters to minimize the difference between the calculated and measured XRR curves, ultimately obtaining valuable structural insights.

3.6.3 X-ray diffraction

X-ray diffraction is a useful tool for determining the sample crystalline structure. Electrons in the atoms are a regular array of scattering centres for x-rays and constructive interference of x-rays results in intense diffraction peaks as described by Bragg's law.

$$n\lambda = 2d_{\text{hkl}} \sin \theta \ , \tag{3.9}$$

where n is a positive integer, x-ray wavelength is λ, d_{hkl} is spacing between atomic planes, and the incident angle between the x-ray and the relevant lattice planes is θ. Fig.3.10 shows the Bragg example of structural interference of x-rays diffracted from atoms separated by a lattice spacing. Bragg's law describes the link between the angles of incidence and reflection and the path difference. Constructive interference occurs as x-rays are diffracted from various planes in the lattice, indexed by h, k and l,

$$d_{hkl} = a_0/\sqrt{h^2 + k^2 + l^2} \; , \tag{3.10}$$

where a_0 is the lattice constant, the length of the edge of the unit cell in the crystal lattice. Bragg's law describes the constructive interference of X-rays and can be determined by measuring the intensity of scattered x-rays as a function of incidence and detector angle.
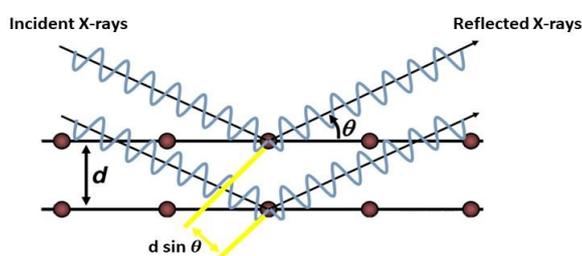
Figure 3.10: A simplified schematic of the x-ray diffraction process, showing constructive interference when the path difference corresponds to an integer multiple of the wavelength.

3.6.4 Experimental Technique

In this study, thin-film measurements were conducted using XRR and XRD techniques, which were performed on Bede D1 and D8 BRUKER diffractometer. The x-ray reflectivity system used is seen in Fig. 3.11. The x-ray system uses a 40 kV voltage to generate Cu-K_α and Cu-K_β x-rays by accelerating electrons emitted by a filament, into a Cu target. The electrons will lose some of their kinetic energy due to the collision, causing the Cu atoms to emit photons with the characteristic of Cu-K_α and Cu-K_β emissions, together with a Bremsstrahlung background. The two separate emissions from the Cu (K_α and K_β) can be obtained by passing the x-ray beam via primary source slits. The primary source slits remove most of the Bremsstrahlung, and then a Si crystal monochromator removes the Cu-K_β by Bragg reflection and rotating the crystal to select the single Cu-K_α wavelength. The beam width is adjusted by closing the secondary slits to 1 mm or 1.5 mm.

The samples were placed on a sample stage, and the incident beam was moved through a variety of angles θ. At 2θ, the detector was scanned in the specular condition. A detector slit is aligned with the reflection angle 2θ to minimise the width of the observed x-ray beam. When performing XRR measurements, it's customary to allocate a data collection duration, or "count time", of 8 seconds for each individual point. Additionally, the θ angle adjustment is typically set with a step size of 0.01 degrees, meaning that the instrument's angle will shift by this increment for each successive data point.

On the other hand, during XRD experiments, a slightly different set of parameters is commonly used. The count time is typically lengthened to 20 seconds for each point, allowing for more thorough data collection. Concurrently, the θ angle's step size is usually expanded to 0.2 degrees, providing a broader view of the sample's crystal structure with each angular shift. It is important to note that these settings represent standard starting points and may need adjustments depending on the specifics of investigation and the characteristics of samples. Balancing data detail, experiment duration, and sample properties is vital to obtain optimal results.
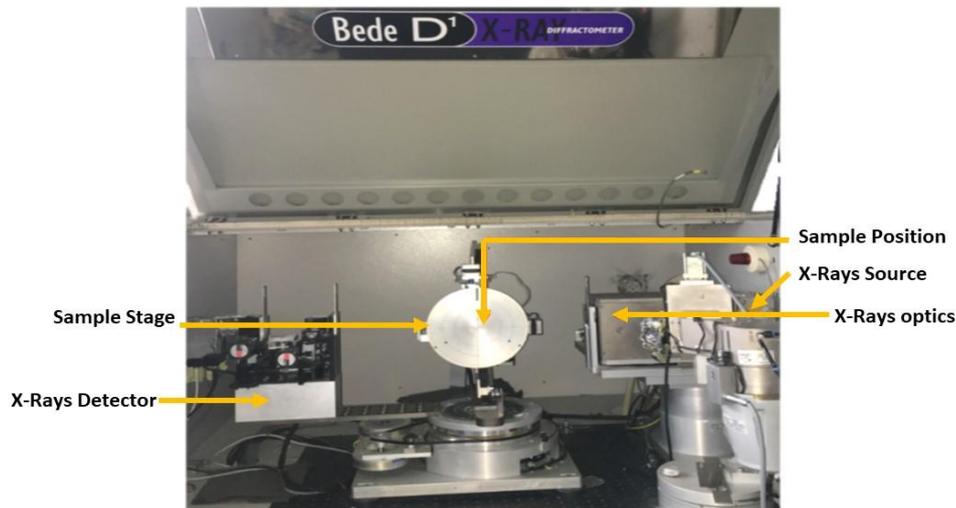
Figure 3.11: The core parts of the Bede D1 x-ray reflectivity system is illustrated.

The open source GenX programme, which uses Parratt's recursion formula to fit the data based on genetic algorithms, was used for data fitting [44]. The software adjusts the density, interface width, and thickness of each layer with a specified scattering factor to generate a scattering length density profile and associated simulated $\theta - 2\theta$ scans to

statistically compare with the data. It is essential to ensure that the simulation is based on a physically realistic model.

GenX uses a user-defined model system of separate layers, with density, roughness, and thickness. According to the dynamics of film growth, it is frequently required to split a layer of a single material in order to model, for example, differences in density between the interfacial region and the bulk. Although it is reasonable to simulate the data with many layers, the quantity of observed data points can limit the number of free parameters that can be handled within reasonable limits. Nonetheless, for large datasets or complex models, the computation time required to evaluate the model with a high number of parameters can also be a substantial constraint [45]. This limitation can be particularly relevant in the case of GenX simulation, where the intricacy of the model and the scale of the simulated system can demand a considerable number of computational resources.

The modelling in software like GenX is largely dictated by the complexity of the system under investigation. When dealing with a system that only involve a few layers, the process can be quick, often taking just several minutes to an hour. But more intricate systems with several layers, or those that need to account for nuanced variations in properties like density or roughness within a single layer, may demand a more substantial time investment. Every layer in a system typically has three defining parameters: thickness, density, and roughness. More complex elements like gradient or oscillating layers necessitate extra parameters. Additionally, each dataset being refined may call for the consideration of other parameters, like scaling factor and background. Overall, the more parameters involved, the more time it will likely take due to the optimization process used to reconcile calculated and observed reflectivity curves [45]. However, this modification process can be expedited, and the probability of finding the optimal solution improved, by providing accurate initial parameter estimates and enforcing relevant constraints.

Summary

This chapter presented experimental techniques to manufacture and structurally characterise the thin film magnetic systems used in this thesis. The samples in this investigation were grown in a high vacuum deposition chamber via magnetron sputtering, and various techniques of film growth have been discussed. The thickness of each layer in thin films, as well as the interfaces between them, can be determined using x-ray reflectivity and x-ray diffraction methods provide additional information about the morphology of nanoscale structures and the crystallisation of thin films for multilayer thin films. Both techniques have been described. The upcoming chapter will provide a detailed description of all the experimental techniques utilized in this study for magnetic characterisation of materials and multilayers.

Chapter 4. Functional Magnetic Measurements

4.1 Introduction

This chapter describes the experimental techniques used in this study, covering functional magnetic measurements. Functional magnetic measurements of a material generally characterise its magnetization state, which refers to the direction and magnitude of the material's magnetic moment. This magnetization state can be affected by, for example, external magnetic fields, temperature, and the crystal structure of the material. Magneto-optical Kerr effect (MOKE) magnetometry, polarised neutron reflectivity (PNR) and ferromagnetic resonance (FMR) spectroscopy are described here. For these techniques, a background on the fundamental concepts is provided first, followed by a description of the experimental system.

4.2 Magneto-Optical Kerr Effect

Polarization of light is a vectorial characteristic of an electromagnetic wave and determines how its electrical component interacts with electron motion in a material. Light polarisation is achieved with a polariser that transmits waves with an electric component aligned parallel to the polarisation axis which is often defined by crystal formation of the materials used to make the polariser, causing it to block waves with an electric component perpendicular to the polarisation axis. When polarised light interacts with a magnetic material, the polarisation can be rotated relative to that of the incident beam. Faraday discovered such rotation in 1845 when polarised light was passed through a magnetic material [46]. Kerr observed an analog of this rotation in 1877 using a reflected beam of polarised light from a magnetic material. The magneto-optical Kerr (MOKE) is the name given to this effect. The MOKE is related to the magnetisation of the material, making it useful as a non-destructive way of exploring magnetic reversal of materials within a skin depth of 10 - 20nm [46, 47]. The theory, principles, and experimental setup of the MOKE magnetometer are discussed in the following sections.

4.2.1 Interaction of Polarised Light with Magnetic Materials

Polarised light transmitted through a material may be considered in two separate geometries; the Faraday geometry, in which the light wave travels parallel to the magnetisation direction, and the Voigt geometry, in which the light travels perpendicular to the magnetisation direction. In the Faraday geometry, the polarised light beam is considered as formed of left and right circularly polarised light, but in the Voigt geometry, it is thought of composed of linearly

polarised light with polarisation parallel and perpendicular to the direction of the magnetic field. The linearly polarised light used for MOKE measurement is thought of as a mixture of left and right circular polarisation. In the case of in-plane MOKE, which can indeed be similar to Voigt geometry, the consideration of circularly polarized light is particularly useful. This is because the interaction of the light with the magnetization in the plane of the film can result in a change in the polarization state that is more easily understood in terms of circular polarizations. A phase difference induced between the two polarisation components provides linear polarisation rotated by an angle relative to the incident polarisation, whereas an induced intensity difference generates elliptical polarisation instead of linear polarisation. Linear polarisation is further categorized into either P-polarised (the electric field vector of the light is parallel to the plane of incidence) or S-polarised (the electric field vector is perpendicular to the plane of incidence).

The Kerr effect is caused by differences in the refractive indices seen by the two helicities of circularly polarised light within the magnetic material. The linear polarisation of the incoming beam is rotated due to the change in refractive indices after a reflection of initially linearly polarised light from a magnetised material. The effective refractive index for each helicity is affected by the sample's magnetisation. Thus, a magnetic hysteresis loop can be obtained by measuring the degree of rotation or the associated, observed intensity change due to polarisation rotation with a fixed analysing polariser, as a function of applied magnetic field [3, 48].

4.2.2 Kerr Effect Geometries

Three geometries can be used to detect magneto optical Kerr effects: longitudinal, polar, and transverse. Polar MOKE occurs when the vector of magnetization is parallel to the incidence plane and perpendicular to the sample surface. In the longitudinal MOKE, the magnetization vector is parallel to both the incidence plane and the sample surface, whereas in the transverse effect the magnetisation lies perpendicular to the incidence plane and parallel to the sample surface. Figure 4.1 demonstrates the three potential geometries involved. In the polar geometry all polarisations experience Kerr rotation, which is highest at normal incidence. The longitudinal and transverse Kerr effects are both sensitive to changes in in-plane magnetisation. The magnetisation is within the scattering plane with the longitudinal geometry, since the magnetic field is applied in the sample plane and along the scattering plane [3]. In this work, only longitudinal measurement geometry was considered. As the light is attenuated within a

metallic film, MOKE is a surface sensitive technique. The skin depth is defined as the length scale along which the intensity decreases to 1/e of its initial value. The reflected light, therefore, is not sensitive to depths much greater than this value. The longitudinal MOKE is most sensitive to in-plane magnetisation when a high angle incident beam with applied magnetic field parallel to the sample surface is used, as illustrated in Figure 4.1a. The main difficulty of this geometry is that a polar component in the reflected beam is possible, dependent on the magnetic anisotropy inside the sample and the angle of incidence [23, 48].
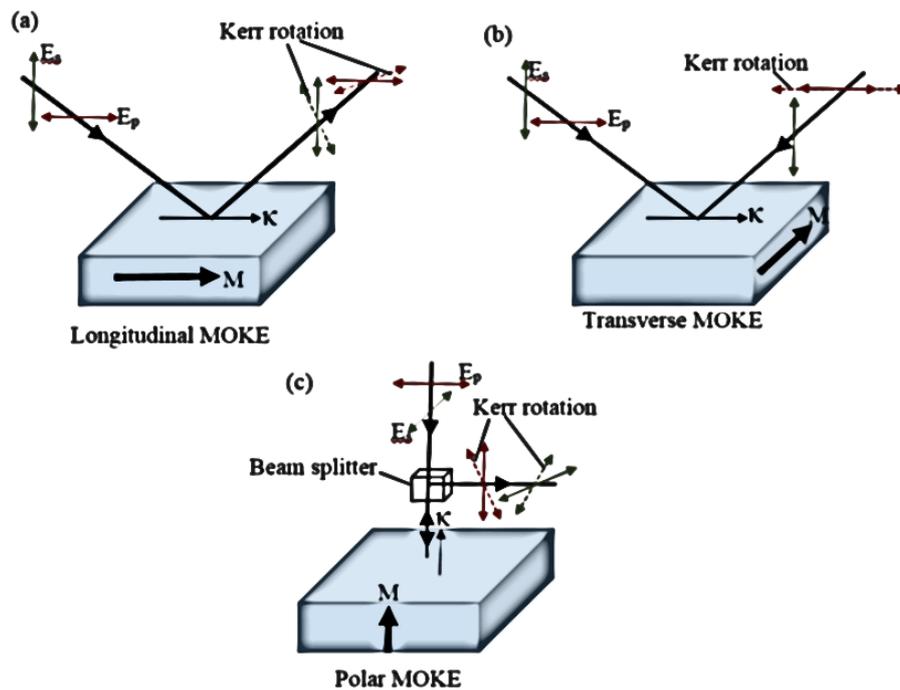
Figure 4.1: Schematic illustrations of the MOKE geometries illustrating magnetisation M and wave propagation direction (a) longitudinal geometry (b) transverse geometry (c) polar geometry [23].

4.2.3 Experimental Setup of Longitudinal MOKE

The experimental setup used was aimed at accessing both longitudinal and polar MOKE. This was accomplished by changing the sample holder and modifying the beam path. A custom designed sample holder was used to install the sample on an x-y translational plate between the poles of an electromagnet. The optical arrangement of longitudinal MOKE is seen in Figure 4.2. The electromagnet was powered by a power supply that was linked to a signal generator, which provided the magnetic field used throughout the measurements.
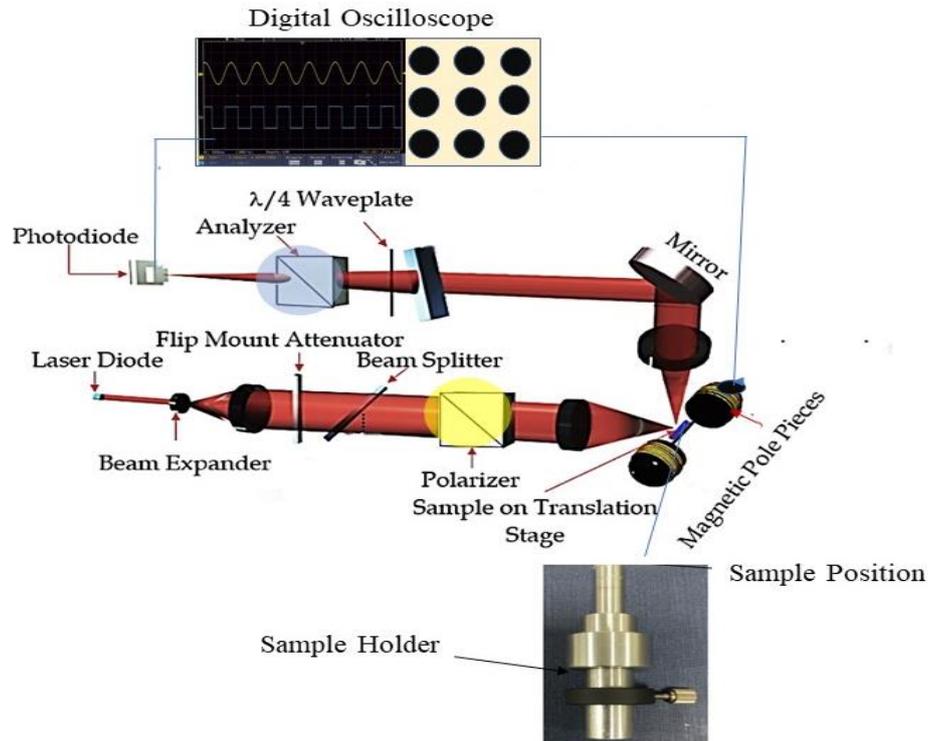
Figure 4.2: Schematic diagram of the experimental setup for longitudinal MOKE measurement and the sample holder is shown.

The incident beam from a diode laser with a wavelength of 658 nm travels via a beam expander into a splitter placed on a motion stage that can be adjusted to guide the beam in longitudinal MOKE geometry. The beam is focussed using lenses deflected using mirrors, and a polariser that helps to improve the beam polarisation ratio. Before being incident on the photo-diode detector, the refocused beam from the sample travels via a focussing lens, a quarter wave ($\lambda / 4$) plate to eliminate any induced ellipticity, and then a Glan-Taylor polarising analyser. The photo-diode signal is converted into a voltage change, and a hysteresis loop averaged over many field cycles is formed.

4.3 Neutron Reflectivity

Chadwick discovered neutrons in 1932 after bombarding beryllium with polonium-derived alpha particles [49, 50]. Bertram Brockhouse and Clifford Shull were awarded the Nobel Prize in 1994 for their pioneering work on neutron scattering. Due to the fact that neutrons are uncharged, they can reach close to the nucleus since there is no Coulomb barrier to overcome, and because of this neutron scattering is like x-ray scattering in that neutrons interact with nucleons in the sample, providing information about the sample's structure as well as the

sample's local magnetisation. As a result of the neutron's spin 1/2 attribute, there is a coupling between the magnetic moment of the neutron and the magnetization state of the material. Neutrons are a non-destructive probe with great penetration because of the weak interaction between neutrons and matter. The following section describes the theory and experimental arrangement for polarised neutron reflectivity (PNR).

4.3.1 Neutron Sources

Atomic nuclei are the primary source of neutron creation, which can be accomplished by a fission process or by use of an accelerator. Fission is the breaking of heavy nuclei into lighter ones with the creation of a residual particle, neutrons and other subatomic particles when a neutron is absorbed. The neutron fluxes produced in reactor sources are typically constant with respect to wavelength variation in most cases [50].

An alternative neutron source is an accelerator, comparable to synchrotron facilities. Spallation occurs when a high energy stream of charged particles (in this instance protons) collides with a heavy metal target (usually tungsten, tantalum, or uranium). The moderator controls the wavelength range of the neutron flux into the instrument [51-53]. It is necessary to have the released neutrons suffer an elastic collision with nuclei in a moderator so that they can achieve thermal equilibrium. The moderator reduces the speed of the neutron, resulting in a neutron beam that is ideal for neutron investigation purposes Since the neutrons generated are extremely high energy, a moderator is again required to bring them back to thermal equilibrium. Also, the moderator controls the wavelength range of the neutron flux into the instrument. Several moderators, including liquid methane at 100 K and liquid hydrogen at 20 K, can be used depending on the neutron scattering technique that is being applied [50].As a result, the relationship between wavelength λ, kinetic energy E and the effective temperature T of a neutron is:

$$E = K_B T = \frac{m_n v^2}{2} = \frac{h^2}{2m_n \lambda^2} \tag{4.1}$$

Since a power outage can stop the process, spallation sources are intrinsically safer than reactor source. Thus, there is no risk of an uncontrolled chain reaction, as there can be in the fission process.

4.3.2 Neutron Scattering Interaction

Neutron reflectivity provides cross-sectional information on the inhomogeneities normal to the sample surface or interface, and like other reflectivity techniques the scattering vector is defined as

$$Q_z = k_i - k_f = \frac{4\pi \sin\Theta}{\lambda} \, . \tag{4.2}$$

The expression for the neutron particle's depth-dependent scattering potential, V:

$$V = \frac{2\pi\hbar^2}{m_n} b_i(r - r_i) \, , \tag{4.3}$$

where b_i is the scattering length of a nucleus labelled 'i' at position r_i and r is the location of the neutron. Within the Born approximation, the reflectivity can be defined as

$$R(Q) = \frac{\pi}{Q^2} |\rho(Q)|^2 . \tag{4.4}$$

here $\rho(Q)$ is the average scattering length density profile, which is a one-dimensional Fourier transform of $\rho(z)$, in equation 4.5. $\rho(z)$ is the product of atom number density N_i and scattering length b_i. For thicker samples, the reflectivity is represented as

$$\rho(Q) = \frac{1}{2\pi} \int_{-\infty}^{\infty} \rho(z) \exp(iQ_z) dz \, , \tag{4.5}$$

$$R \approx \frac{16\pi^2}{Q^2} (Nb)^2 , \tag{4.6}$$

where b is the neutron scattering length and N is the number density. The neutron scattering length density is Nb. The effective refractive index, n(z), for neutrons is given as:

$$n(z) = 1 - \sum_i N_i(z) b_i \lambda^2 / 2\pi \, . \tag{4.7}$$

The scattering length density is positive and small for most materials, making the refractive index slightly less than 1, as for x-ray reflectivity, described in section 3.6. The scattering length density and refractive index are also modified depending on the direction of

the incident neutron spin relative to the material magnetization, making neutron scattering an effective method for investigating depth-resolved magnetism [54].

4.3.3 Polarised Neutron Reflectivity

Polarised neutron reflectivity (PNR) is a very sensitive method that may be used to determine the magnetic properties of ultra-thin films by measuring the structural and magnetic scattering length density profiles. A magnetic field is applied to the sample in a PNR experiment to keep the neutron beam polarised and the sample magnetisation parallel to the field. The neutron beam is polarised into two spin states by spin flippers positioned before and after the sample site to switch the neutron spin from one state to the other. There are four spin polarisation states to be measured at the detector, which are ++, --, -+ and +- polarisation states, which represent the polarisation states of the incident neutron and scattered neutron. Experiments where all 4 spin states are measured, such as those reported in this thesis, are referred to as polarised neutron reflectivity with polarisation analysis (PNR-PA).

If the first flipper is OFF, the + polarisation state is incident on the sample and if the second flipper is also off the analyser reflects only neutrons that have not been subjected to a spin flip, resulting in the measurement of the + + polarisation state at the detector. In order to measure the - + state, the first flipper must be turned ON, indicating that only - polarised neutrons are allowed across, and the analyser still only permits + polarised neutron state to pass through. If the first flipper is OFF and the second flipper is ON, the opposite will occur, and the + - state is determined. Furthermore, by turning ON the two flippers, the --polarization state is obtained. In general, the polarisation states - - and + + are referred to as the non-spin flip (NSF) states, whereas the polarisation states - + and + - are referred to as the spin flip (SF) states [50]. For polarised neutrons, the total scattering potential is expressed as [53],

$$V = \frac{2\pi\hbar^2}{m_n} \begin{pmatrix} \rho_{++} & \rho_{+-} \\ \rho_{-+} & \rho_{--} \end{pmatrix} \tag{4.8}$$

Relative to the spin polarisation, the scattering length densities are expressed as:

$$\rho_{++} = \rho_{\text{nuc}} + \rho_{\text{zmag}}, \rho_{--} = \rho_{\text{nuc}} - \rho_{\text{zmag}},$$

$$\tag{4.9}$$

$$\rho_{-+} = \rho_{\text{xmag}} + i\rho_{\text{ymag}}, \rho_{+-} = \rho_{\text{xmag}} - i\rho_{\text{ymag}}.$$

where ρ_{nuc} represents the nuclear charge density and ρ_{zmag} represents the charge density due to the magnetization in the z-direction. The (x, y, z) mag are the associated magnetisations in the x, y and z-planes. The z-component of magnetization provides insights into the distribution of magnetization within the depth of the sample. It provides information on the vectorial components of magnetisation. The term *nuc* stands for nuclear and represents the contribution to the scattering length density arising from the interaction of the neutron with the atomic nuclei in the material. More on polarised neutron reflectivity is given in [39, 50, 53].

4.3.4 The Polref Reflectometer

Polarised neutron reflectivity experiments were carried out at the Rutherford Appleton Laboratory, STFC, UK, using the Polref beamline. Polref is a reflectometer with a neutron beam incident with a wavelength range of 0.5 - 6.5 Å and the neutron beam source frequency of about 10 Hz. The configuration is designed such that the source of the neutron beam is angled 2.3 ^{o} away from the horizontal to reduce fast neutrons and background γ rays in the direct line of sight of the detector. There is a 23 m gap between the source and the sample stage, and a 3 m gap between sample environment and detector. The neutron beam incident on the sample passes through two synchronous disc choppers, that define the wavelength band, a frame overlap mirror, a polarising mirror, spin flipper, guide field and a beam monitor. The Polref polarised neutron reflectivity setup is shown in Fig 4.3.
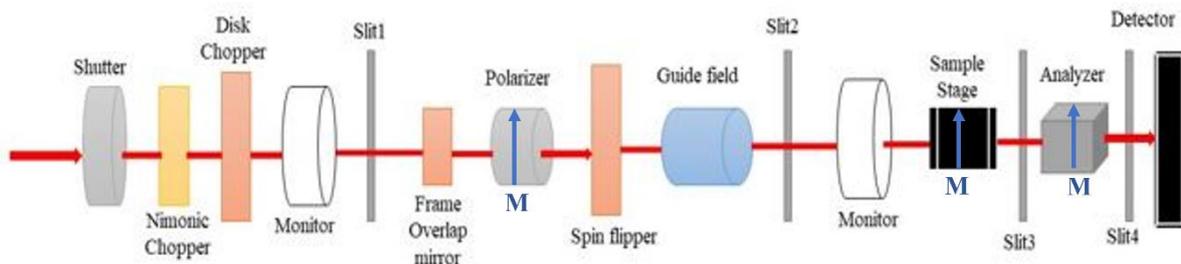
Figure4.3: Schematic of the neutron optics for PNR-PA measurements on the Polref beamline at ISIS. The neutron beam is indicated by the red arrow incident from the left.

The magnetic guide permanent magnets generate guide field, which is designed to reduce the influence of stray fields and thus maintain neutron polarisation. Polarisation matrix elements are accessible in the sample environment because the magnetic field is aligned with the incident polarisation. Refl1D is a software that is frequently applied for fitting PNR data.

It supports the creation and modification of theoretical models to correspond with the reflectometry data and the scattering length density profiles of the sample under investigation. The model considers the physical and magnetic structure of the sample, including layer thicknesses, interface roughness, magnetization, and scattering length densities. The modelling approach in PNR is quite analogous to that used in x-ray reflectivity, with the additional complexity of including the sample's magnetic properties. This allows PNR to provide a more complete picture of the magnetic structure of the sample, including information about the depth-dependent magnetization that is not accessible through x-ray techniques.

4.4 Ferromagnetic Resonance (FMR)

Measurements of ferromagnetic resonance (FMR) determine the dynamic properties of magnetic materials over a broad range of frequencies [55]. Electrical measurements based on strip-lines, and cavity-based systems, are the two methods that are mainly used to investigate the FMR and the magnetic damping. In 1946, Griffiths carried out the first experimental analysis in FMR microwave absorption [56]. Kittel proposed the theoretical description two years later [21]. In both theory and application, FMR has become a well-known technology. The relationship between the magnetization, effective field, and resonant precession frequency is known as the Kittle formula which, for thin-films and cgs units is given by:

$$f = \frac{\gamma}{2\pi} \sqrt{H_{\text{eff}}(H_{\text{eff}} + 4\pi M_{\text{eff}})} \qquad (4.10)$$

Here H_{eff} is the effective field, M_{eff} is the effective magnetisation which includes the perpendicular anisotropy demagnetising field and the saturation magnetisation, and γ is the gyromagnetic ratio.
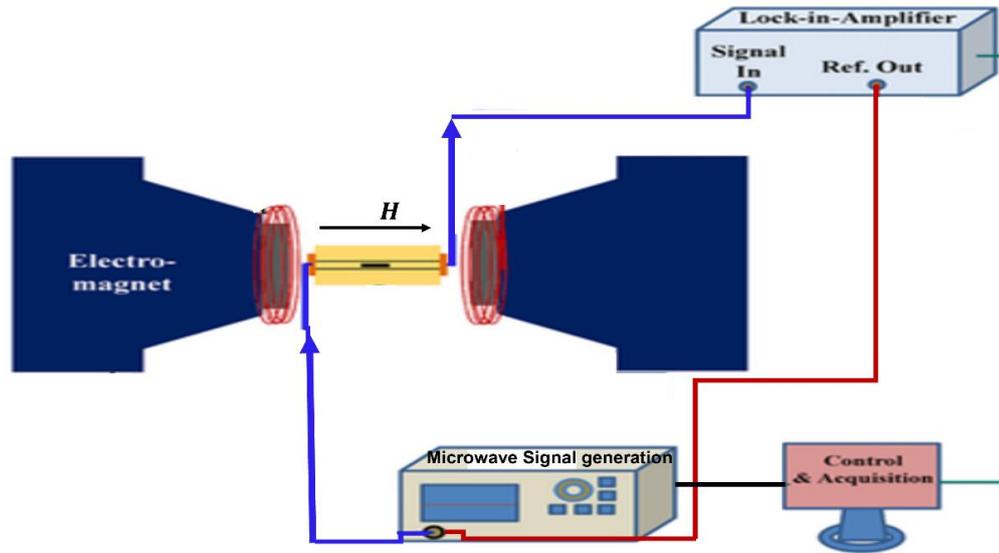
Figure 4.4: Diagram displaying the FMR with the directions of the microwave and the rf for the external field and the ferromagnetic magnetic film is placed on the CPW mounted in non-magnetic sample holder between the magnetic coils.

The process of generating and detecting broadband microwaves can be carried out using either a microwave signal generator in alliance with a diode detector or a vector network analyser as the source and phase detector of the necessary microwaves [21]. A coplanar waveguide (CPW) or strip-line can be used to transfer the stimulations of microwaves to the sample. Fig.4.4 illustrates the FMR instrument schematically, where the applied magnetic field is swept each microwave frequency. The RF signal is amplitude modulated and output of a power detector diode is measured with a lock-in amplifier. This allows measurement of transmitted power vs field at a given RF frequency.

4.4.1 Analysis method for the FMR

 FMR analysis gives us access to the ferromagnetic layer's many material characteristics for estimation of the spin current behaviour [21]. In general, electrical FMR measurements detect the transmission and/or reflection of microwave power by an antenna. These are often given by the scattering parameters S_{21} and S_{11} measured by a VNA. [15]. The scattering parameter values represent the microwave absorption intensity through the magnetic sample, and in the measured spectrum, the microwave power absorption is shown as a dip. In this thesis, a measurement roughly equivalent to S_{21} is made by driving the strip-line with a microwave signal generator and detecting the power output at the other end of the strip-line as the output voltage of a RF power detector diode [57]. In order to improve the signal to noise, the RF signal is modulated at ~5 kHz with sinusoidal modulation and lock-in detection is used to measure

the diode power detector output voltage. The S_{21} signal can be divided into two components as real (in-phase) and imaginary (out-of-phase). The FMR experiment's microwave response signal (εx) relies on the RF magnetic susceptibility $x = x' + ix''$ along the applied RF field direction. The Landau-Lifshitz-Gilbert (LLG) equation can be used to determine the linear response to a RF signal for both in-phase and out-phase components as

$$\varepsilon'_x = A \left(1 + \frac{H - H_{\text{FMR}}}{\Delta H^2 + (H - H_{\text{FMR}})^2} \right), \tag{4.11}$$

$$\varepsilon''_x = A \left(\frac{H - H_{\text{FMR}}}{\Delta H^2 + (H - H_{\text{FMR}})^2} \right). \tag{4.12}$$

Here H is the external applied DC field, the resonance field is H_{FMR}, ΔH is the half-width-at half-maximum linewidth of the Lorentzian absorption. The amplitude A can also be obtained from

$$A = a\Delta S M_S d \frac{B_{\text{FMR}}}{B_{\text{FMR}} + H_{\text{FMR}}}, \tag{4.13}$$

where B_{FMR} and H_{FMR} are B and H field at the FMR, the film surface area is ΔS, a is the proportionality factor, and d is the film thickness. It is not necessary to separate the measurement of the ε'_x and ε''_x, a mixture measurement of them can be taken that can be seen on a rotated coordinate system as their projection by using the angle of rotation in the complex plane φ as

$$\varepsilon_x^{mix} = \text{-}sin\, \varphi \varepsilon'_x \ + cos\, \varphi \varepsilon''_x \, . \tag{4.14}$$

Fig.4.5 shows an example of measured FMR spectra taken by the field sweep. The field- and frequency-dependent background is a result of the impact of the Lorentz force on electrons making up the RF current in the strip-line. For the analysis, all raw data are collected without assumptions and then fitted with a suitable model based on equations 4.10-4.14. The simplex algorithm was used to determine the approximate location of the peaks as starting point to the fit. The background is modelled as locally quadratic over the range of the peaks, and the data far from the resonance peak is discarded since the background may become more complicated further from the resonance condition. We fit a model with three parameters describing the

quadratic background, amplitude, peak position, linewidth, and mixing angle describing the resonant absorption peak. The mixing angle, as defined in equation 4.14, serves as a measure of how much the in-phase and out-of-phase components of susceptibility contribute relative to each other. It represents the angle that characterizes the phase relationship between the RF field and the magnetization precession.

The RF frequency- (f) dependence of the half-width-at half-maximum linewidth enables the Gilbert damping parameter alpha to be determined using

$$\Delta H = \Delta H_0 + \frac{4\pi\alpha}{\gamma} f. \tag{4.15}$$
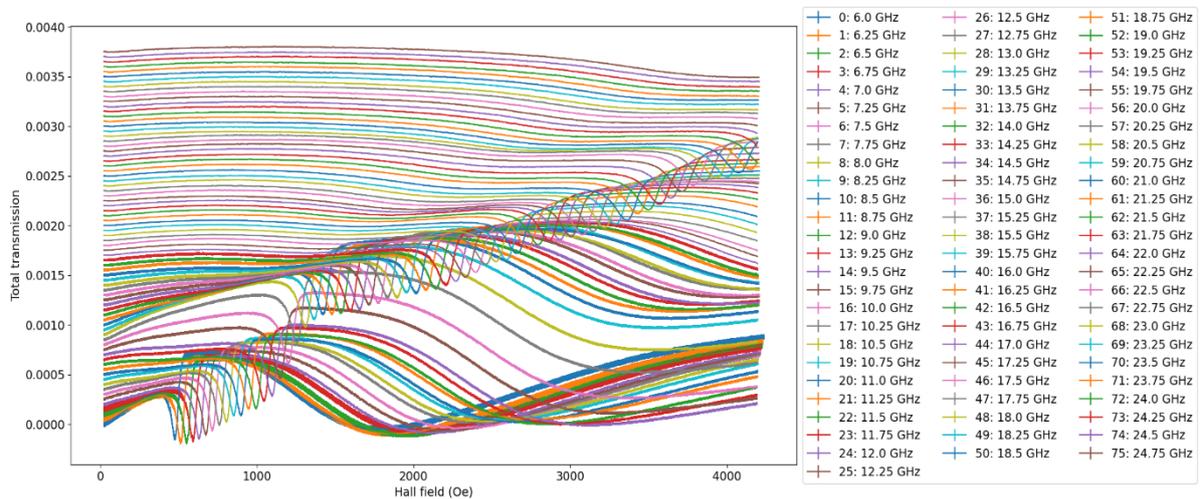
Figure 4.5: Shows a typical data of FMR measurements of the field sweep measurement for CoFe 10 nm/ Ag 4 nm / CoFe 10 nm sample.

In Figure 4.5, the error-bars in the measured transmission for each datapoint serve as an illustration of the total signal noise originating from the lock-in amplifier. This noise is an aggregate of multiple factors: the Johnson noise generated by the power detector diode (associated with its resistance), the input noise from the amplifier stage of the LIA (a specification of the amplifier itself), and the resolution of the analog-to-digital converter integrated into the LIA. The fit performed here is based on the 'least-squares' method, and this provides errors in the various parameters that are then carried forward into the analysis, as demonstrated in Figure 4.6. The resulting error-bars are generally small and are not visible in this instance. After this, by measuring the resonance frequency as a function of the external

magnetic field, we can derive the effective magnetization anisotropy constant (H_a) and the g-factor (g) by utilizing the suitable Kittel equation (eq 4.10).

Fig 4.6 (a) shows the Kittel equation fitted to an example set of FMR spectra, similar to those in fig 4.5 but represented as a colour map. This equation is a proven theoretical model for describing the resonance condition in ferromagnetic substances. It paves the way for the extraction of vital parameters, which include the effective magnetization, anisotropy constant, and the gyromagnetic ratio. The fitting process relies on minimizing the variance between the observed experimental data and the predictions made by the Kittel equation. This minimization is achieved using a least-squares fitting method.

Fig4.6 (a) and (b), the resonance linewidth as a function of frequency is displayed. The linewidth is associated with the damping in the system, indicating the rate of energy dissipation in the system. As the frequency increases, the linewidth typically widens, illustrating augmented damping at higher frequencies. A line is fit to the linewidth-frequency data, as in equation 4.15, the intercept gives the extrinsic linewidth and the slope, when used in conjunction with the gyromagnetic ratio, gives a measure of the effective Gilbert damping. The fitting approach employed in these instances is instrumental in deriving physically meaningful parameters from the data, thereby enabling a comprehensive understanding of the system. The reliability and precision of the fitting process are crucial to deriving accurate parameters and gaining a profound understanding of the experimental results. The fit's quality is generally evaluated based on the residuals (the difference between the experimental data and the fitted data), and chi-squared value.
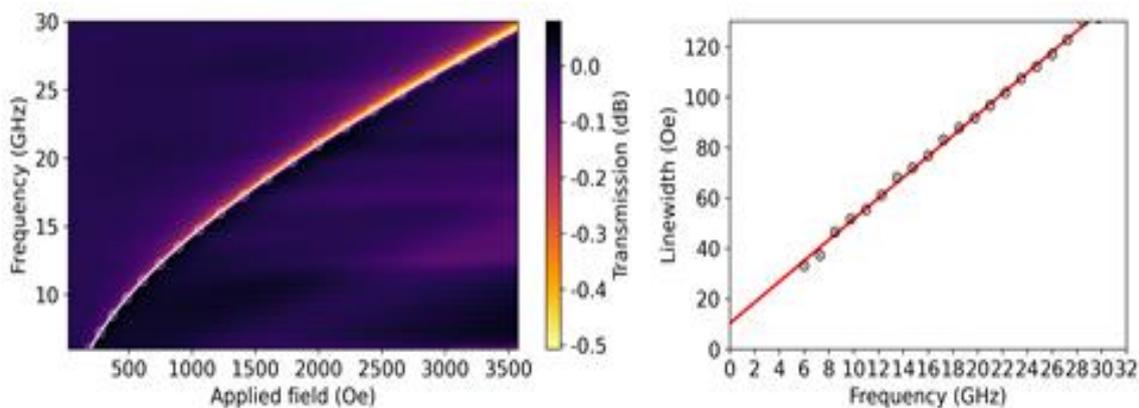
Figure 4.6: shows (a) and (b) are the Kittel formula fitting according to the relation between the field and the frequency.

In the following chapter, we have explored correlation plots and histograms, providing examples of field-dependent line-shapes. For each frequency, the absorption aligns well with a Lorentzian line-shape function and a quadratic background, as defined in this chapter. Also, the high quality of the fit is affirmed by the residual plots for each dataset.

Chapter 5: The Evolution of Damping in FM/Ag/FM Thin-Films as a Function of Ag Thickness

5.1 Introduction

This chapter provides detailed description of the magnetic damping in FM/NM/FM samples system. The chapter begins with a background discussion on the fundamental concepts followed by an analysis of damping, experimental details, and ferromagnetic resonance (FMR) data analysis. The techniques employed are explained in detail, and the results of the effective damping are presented. Based on the observed FMR linewidth variations with resonance frequency, our findings have been separated into two categories: those with a 'conventional' linear frequency dependence and those with an anomalous non-linear frequency dependence of the linewidth. Non-linear linewidth indicates that these FM/Ag/FM structures may exhibit complex behaviours, which are difficult for our existing theoretical models to sufficiently clarify. The defining of this novel linewidth behaviour in this chapter motivates the studies in the following chapters, which aim to clarify this behaviour using different experimental methods.

5.2 Background

The study of precessional dynamics of magnetization is crucial for magnetic field and current driven applications, including magnetic data storage and magnetic sensors, where fundamental limits on the speed of data writing and switching behaviour are controlled by the magnetic precessional dynamics and damping. A deep understanding of the spin pumping mechanism is critical, especially in the field of spintronics, where controlling spin currents is indispensable for creating advanced devices such as spin-transfer torque memory and spin-based logic gates. Investigations into the origins of damped magnetization precession, especially within the scope of magnetic devices, have been an area of focus in both theoretical and experimental scientific disciplines. FM materials, notably CoFe and NiFe alloys, have garnered considerable interest due to their unique physical and magnetic characteristics [24, 58-64]. Their high saturation magnetization makes them suitable for applications in magnetic data storage and magnetic resonance imaging. Furthermore, these alloys are notable for their high magnetic permeability, a property that is advantageous in magnetic shielding applications. Another essential feature is

their low coercivity, meaning they can be magnetized and demagnetized with relative ease, a valuable quality for components such as transformer and inductor cores. Additionally, these materials possess high Curie temperatures, allowing them to maintain their ferromagnetic properties at higher operational temperatures. Their impressive resistance to corrosion, especially for NiFe alloys, makes them suitable for long-term use in diverse environments [10]. However, it is essential to acknowledge that these alloys' magnetic traits can significantly differ depending on the components' proportions. Such variability opens a wide spectrum for research, potentially leading to improvements in magnetic devices' operational efficiency. A good example is the study into understanding the correlation between alloy composition and damping in CoFe alloys discussed in [65].

When ferromagnets are combined with a heavy NM material as an adjacent capping layer, the overall damping value changes [59, 60, 65-67]. Previous studies, like the one conducted by Tserkovnyak et al., have delved into this phenomenon [67, 68]. Their research explained how spin pumping could significantly contribute to damping. In layered structures involving magnetic and non-magnetic materials, such as bilayers and multilayers, the characteristic known as spin-diffusion length plays a significant role in determining the behaviour of the overall system. Spin-diffusion length refers to the distance that an electron can travel within a material before its spin information is lost due to scattering processes. When dealing with a bilayer system, it is generally desirable to have a material with a short spin-diffusion length. This ensures that any spin-current originating in one layer is efficiently absorbed by the adjacent layer, effectively influencing its magnetic behaviour and in turn, the damping properties.

Theoretical studies of FM/NM bilayers have demonstrated how damping changes with increasing thickness of the non-magnetic layer assuming a flat interface. The damping behaviour due to NM layers can be significantly influenced by the nature of the material used and the thickness of the layers. Two main factors can explain this prediction. Firstly, the spin diffusion length, which may vary among materials. Consequently, materials with a shorter spin diffusion length so that the NM layer acts as a more effective spin-sink and has a greater impact on damping in FM. Secondly, the spin-mixing conductance, can also impact damping behaviour by controlling the ability of spin-current to cross the interface into NM [69]. Hence, the material's innate properties and the NM layer's thickness could modulate the damping characteristics observed in these bilayer systems. It also suggested that the damping properties of FM and NM materials are not constant throughout their constituent monolayers, meaning

that these properties can exhibit spatial variations within the individual layers of the material [70]. Such variation might be due to various factors such as a lack of uniformity in the material's intrinsic properties, structural anomalies or defects, or the effects of interfacial interactions at the layer boundaries. These spatially variant properties can profoundly influence the overall system dynamics, including the damping behaviour observed.

In FM/NM/FM trilayer structures, a pivotal role is also played by spin pumping. The precessing magnetization in one FM layer generates a spin current or an angular momentum flux that injects spins into the adjacent NM spacer layer. These spins can then traverse the NM layer, potentially reaching the FM layer on the other side. This process can lead to a variety of effects, including the exchange of angular momentum between the two FM layers. If the NM layer thickness is sufficiently small relative to its spin-diffusion length, it can promote an effective angular momentum exchange, hence enabling a coupling between the FM layers. This interaction mediated by the spin current can induce complex magnetic behaviours that are crucial in the design of advanced spintronic devices [71].

Chiba's paper explores into the analysis of magnetization dynamics in spin valves, which are essentially synthetic antiferromagnets [72]. The initial state of the magnetizations in this system is set to be antiparallel, courtesy of the RKKY (Ruderman–Kittel–Kasuya–Yosida) interlayer coupling. The interlayer coupling, and the two magnetic layers are considered to be identical. The precession of FM layers can be either in-phase or out-of-phase, when the coupling between the FM layers is strong enough, it can cause a phenomenon called mode splitting. This is where each of the FM layers would individually have the same resonance frequency in the absence of coupling, but due to their coupling, two distinct resonance modes appear: the acoustic mode and the optical mode. The acoustic mode entails the synchronized oscillation of the magnetic moments, leading to a larger combined magnetic response. Conversely, out-of-phase precession, or the optical mode, involves oscillation of magnetic moments in opposition, potentially resulting in a net dynamic component of the magnetization of zero and a lower energy state. This distinction can drastically alter the magnetic behaviour of the multi-layered structure and its applicability in spintronic devices such as magnetic sensors [73, 74].

The interaction of magnetization in a FM/NM/FM system can vary substantially depending on whether the orientations are colinear or noncolinear. When the magnetizations are colinear, either parallel or antiparallel, the synchronized precession of the two layers simplifies the system's dynamics, typically presenting a single resonance frequency. On the other hand, a noncolinear configuration, where the magnetizations are not aligned parallel or

antiparallel, allows for asynchronous precession, which introduces complexity into the dynamics and may result in multiple resonance frequencies with anomalous field dependence, and modified damping [75].

In multilayer system, the concept of spin-mixing conductance is crucial as it indicates how successfully the spin current can be transferred between the magnetic layers. A high spin-mixing conductance facilitates a more efficient exchange of spin angular momentum at the interface of the layers, leading to considerable implications for the system's dynamics. Varying theories regarding resonance frequency and damping can be intricate due to their dependence on a multitude of factors. These factors include not just the spin-mixing conductance and spin-diffusion length, but also the strength of interlayer coupling, the ferromagnetic layers' inherent properties, and external aspects such as the imposed magnetic field. Typically, an enhanced interlayer coupling combined with a more efficient transmission of spin current can result in more noticeable alterations in resonance frequencies and damping.

When the spin current is efficiently transferred across the NM layer and reaches the other FM layer, it indicates a strong coupling between the two FM layers facilitated through the NM layer. This efficient exchange of spin across the layers can significantly influence the dynamics of the system. The extent of this effect is tied to the characteristics of the interface separating the layers and the thickness and nature of the nonmagnetic layer [76-78]. Thus, there is interest in investigating the dependence on the dynamic properties on the NM spacer thickness, which can impact not only the interface development but also the static and dynamic coupling between the FM layers.

The two FM layers can exhibit in-phase (acoustic mode) or out-of-phase (optical mode) behaviour, contingent on the strength of interlayer exchange coupling, further impacting the damping behaviours. To effectively assess the overall damping in such a trilayer structure, it is crucial to consider both intrinsic and extrinsic damping sources. The individual contributions from each source can vary based on the type of FM material, their interfaces, the type of nonmagnetic material involved, and the system's configuration, such as whether the magnetizations precess in-phase or out-of-phase [72]. Both intrinsic and extrinsic damping contribute to the overall increase in damping.

In the FM/NM/FM system, the interactions between spin currents originating from each FM layer play a crucial role in the coupling between the FM layers and the resulting damping behaviour. The interface characteristics between the FM and NM layers [79], including

interfacial roughness and interfacial magnetic properties, can significantly influence the spin current coupling. When the interface is smooth and well-maintained spin current can flow seamlessly from one FM layer to the NM layer. However, if the interface is rough spins get flipped, and the flow becomes less efficient. This is because the uneven surface causes scattering of the spins. Thus, a smoother interface allows for more efficient transfer of spin current, improving the coupling between the FM and NM layers. The magnetic properties at the interface also play a significant role in the spin current coupling. If the interface possesses strong magnetic properties, it can act like a magnet that causes spin precession, influencing their flow. On the other hand, if the interface has weak or negligible magnetic properties, it has less influence on the spin current. Therefore, by controlling the interfacial magnetic properties, we can potentially control how the spin current couples between the FM/NM or NM/FM layers.

The coupling between the FM layers in the presence of the NM layer can give rise to intriguing phenomena. One example is spin-transfer torque, where the spin-polarised current from one FM layer exerts a torque on the magnetization of the other FM layer, leading to a transfer of angular momentum. Another phenomenon is spin-torque oscillations, where the spin currents induce sustained oscillations of the magnetization in one or both FM layers. To comprehensively understand these intricate spin current interactions and their impact on the damping behaviour, detailed experimental evidence is required in order to guide and drive theoretical understanding. Experimental characterization techniques, such as spin pumping can provide insights into the spin current dynamics and their coupling effects.

The spin current will inevitably lose coherence within a limited distance in ferromagnetic metals, transverse spin-current absorption occurs through dephasing [79-81], which is the destructive interference of coherent spins precessing around the magnetic exchange field. Figure 5.1 illustrates this mechanism, where transverse electronic spins enter the ferromagnetic metal with varying wavevectors, precessing around the magnetic exchange field at different rates, resulting in a cancellation of the net transverse polarisation and loss of phase coherence within a finite distance. Diffusive spin-flip scattering [81] is an additional mechanism for the absorption of spin currents, in which the spin orientation of electrons transporting the spin current may be altered to various orientations when they collide with impurities or an interface.
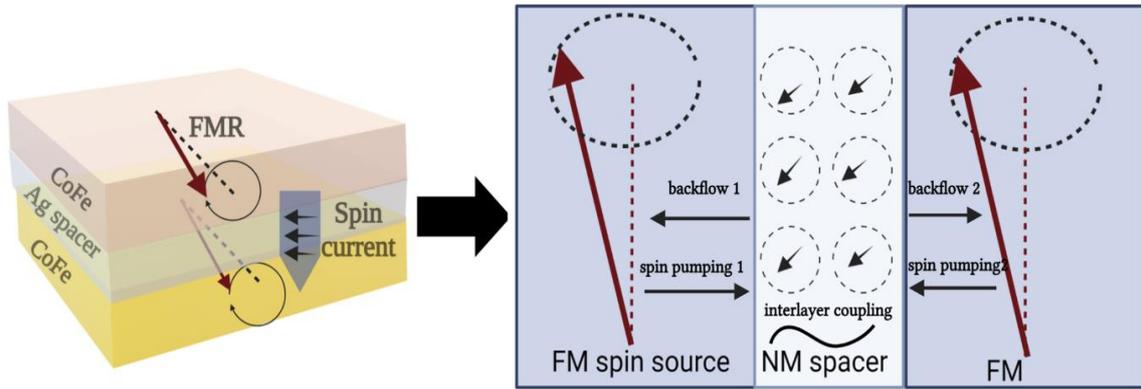
Figure 5.1. When a transverse spin current is generated by FMR in a ferromagnetic (FM) spin source, the propagating spins are coherent in the normal metal (NM) spacer, as shown by the aligned black arrows. However, in the second FM layer, the spins process around the ferromagnetic exchange field by varying degrees, leading to a loss of phase coherence. This process is referred to as dephasing of the transverse spin current.

This chapter focuses on investigating the spin-pumping contribution to the damping between two identical 10 nm thick CoFe magnetic layers separated by Ag. The precessional dynamics were measured using ferromagnetic resonance. The results showed that the thickness of the Ag interlayer had a significant impact on the damping. Spin-pumping between the two identical FM layers possibly leads to an enhancement of the damping when the Ag layer thickness corresponded to an antiferromagnetic coupling peak. Due to the Ruderman-Kittel-Kasuya-Yosida (RKKY) interaction into the effective fields, stationary spin-wave modes in anti-phase could possibly be formed across the Ag layer, similar to what was modelled in [72, 82].The RKKY coupling is an indirect interaction between spins in the ferromagnetic layers, mediated by the conduction electrons in the Ag layer. While the RKKY coupling in Ag is generally weak, it is not negligible, and it facilitates a certain degree of magnetic coupling between the ferromagnetic layers. When the thickness of the Ag layer corresponds to an antiferromagnetic coupling peak, the weak RKKY interaction in Ag tries to align the spins of the ferromagnetic layers in an antiparallel configuration but it is not strong enough to do so. However, it still plays a role by making a contribution to the effective magnetic field. Consequently, it induces alterations in the precessional movement of the spins.

5.3 Experimental Details

A range of FM/Ag/FM based thin-films were fabricated by depositing multi-layer thin-films on an oxidised silicon substrate with a 100 nm SiO_2 layer. All samples are fabricated by sputtering with a base pressure of $\approx 10^{-7} - 10^{-8}$ Torr. In Chapter 3, further information is provided on sample preparation as well as magnetron deposition. The FM layer was formed straight onto the SiO_2 substrate, and the overall structure of all thin films generated was Si/ SiO_2/FM/Ag/FM. Both FM layers were 10 nm thick, whereas the Ag layer thickness varied from 0.2 to 10 nm. The replication of the same growth conditions across five sets of samples, each set comprising around eight samples, demonstrates a reproducible and well-controlled deposition process. Though the sets were formed at different times, maintaining identical growth conditions ensures the consistency of the experimental data. This uniformity is a proof to the robustness of the sputtering system, which enables precise control over the growth process, leading to reproducible results across different sets.

It is possible that the surface of the FM material in the thin films has completely or partially oxidised because of the absence of the capping layers. An additional capping layer can be a potential strategy to mitigate unwanted influences on the FM/Ag/FM system. However, it is important to note that introducing a capping layer increases complexity to the physical system, which may complicate the interpretation of the trilayer behaviour. All characterization was done at room temperature. Under this condition, the oxides of CoFe should not show magnetic ordering, thus this should not have an influence on FMR. In this study, the key focus was to investigate the effect of Ag layer thickness on the damping. The addition of a capping layer could further influence the precessional dynamics.

5.3.1 FMR, Data Analysis and Magnetic Damping Thickness Dependence

FMR was used to study the dynamic magnetization behaviour of CoFe/Ag/CoFe samples, and the system details can be found in Chapter 4. There are several steps of analysis used to determine the dimensionless damping parameter, which provides insight into the magnetic properties of the material. Figure 5.2 presents examples of the FMR data obtained for selected CoFe/Ag/CoFe samples.
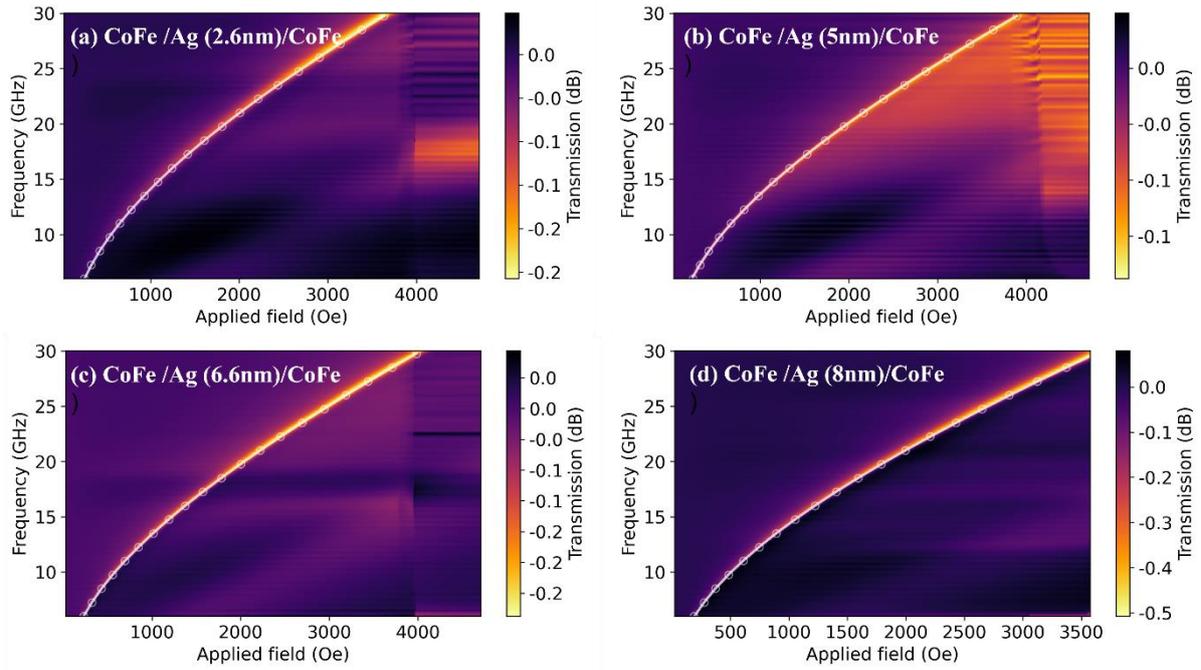
Figure 5.2. Examples of FMR measurements taken for CoFe/Ag/CoFe, including (a) CoFe (10nm)/Ag (2.6nm)/CoFe (10nm), (b) CoFe (10nm)/Ag (5nm)/CoFe (10nm), (c) CoFe (10nm)/Ag (6.6nm)/CoFe (10nm) and (b) CoFe (10nm)/Ag (8nm)/CoFe (10nm). Datapoints show the fitted resonance field at various frequencies, and the solid line is a fit to the Kittel equation.

Each plot shows a bright absorption feature, which corresponds to the absorption line (an example of which has been shown in chapter 2) at each frequency, as a colour-map encoding the absorbed power in dB. The datapoints overlayed are the resonance field and error obtained from fitting the absorption line-shape at each frequency, and the solid line is a fit to these points using the Kittel equation. From FMR data, magnetic parameters, such as saturation magnetization, magnetic anisotropy, and gyromagnetic ratio, can be extracted using the Kittel fit. These magnetic parameters are linked to the resonant field by the Kittel equation [21]

$$f = \frac{\gamma}{2\pi} \sqrt{(H + H_K)(H + H_K + M_{eff})},$$

(5.1)

where f is the resonance frequency, γ is the gyromagnetic ratio, H is the applied magnetic field, H_K is the magnetic anisotropy field, and M_{eff} is the effective magnetisation. To perform a Kittel fit, the FMR data is first plotted as a function of magnetic field. The resonant peak is identified, and a region of the data centred on the peak is selected for fitting. The resonant field is extracted from the peak position. The Kittel fit is a simplified model employed to characterize the resonance behaviour of ferromagnetic materials. It assumes a uniform precession of

60

magnetization in a single-domain sample, where the resonance field is primarily determined by the magnetic anisotropy field. The four frames in figure 5.2 show samples with different Ag thickness. Parameter values extracted from Kittel fit are given in table 5.1.

Sample	Effective Magnetization (G)	g- factor	Anisotropy Field (Oe)
Ag (2.6nm)	1342 ± 4	2.4 ± 0.03	-81.3 ± 0.5
Ag (5nm)	1136 ± 3	2.5 ± 0.02	-29 ± 0.4
Ag (6.6nm)	1025 ± 2	2.6 ± 0.02	-23 ± 0.3
Ag (8nm)	1067 ± 3	2.6 ± 0.03	-25 ± 0.3

Table 5.1. Values extracted from Kittel fit from selected samples with varying the Ag thickness.

As can be seen from table 5.1, the effective magnetization $\mu_0 M_{eff}$ values measured from all the samples are within the anticipated range for CoFe alloys, which were approximately 2400 mT for $Co_{25}Fe_{75}$ for a single layer film [83] and 2350 mT for films characterized by $Co_{28}Fe_{72}$ (10 nm) with Cu layers in both sides [65]. In our study, the $\mu_0 M_{eff}$ was determined to be around 1685 mT. The evident difference of 665 mT and this can provide a window into potential variations in perpendicular magnetic anisotropy. The thickness of the Ag layer in our films emerges as a probable contributor to this variation. As the thickness of the Ag layer shifts, it can modulate the magnetic interactions at the boundary, subsequently affecting the film's overarching magnetic anisotropy. This juxtaposition points out the nuanced interdependencies between the material components, their respective thicknesses, and the resulting magnetic characteristics. In specific FM/Ag/FM structures, the g-factor, describes the relationship between the magnetic moment and the angular momentum of electrons in a magnetic field, values can indeed correspond to those enumerated in Table 5.1. The determination of the g-factor in FMR investigations is sometimes difficult in thin-film limit due to larger uncertainties. However, by using an advanced analytical approach on a broad data set, it is possible to achieve errors to less than 1%. The g-factor data in shown in table 5.1 may have some dependence of Ag thickness. The presence of interfaces and adjacent layers has been shown to modify the g-factor in thin films [84]. Also, the in-plane anisotropy field values are listed in Table 5.1 for a range of Ag thicknesses. When the Ag layer is greater, we can see a more consistent and lower anisotropy value. On the other hand, the thinner Ag layer, in this case 2.6 nm, exhibits a higher anisotropy value. The RKKY interaction in these thinner layers could potentially cause this increasing in the anisotropy.

5.3.2 Absorption Line-shape

In general, a Lorentzian function is used for modelling the shape of spectral lines. The reason lies in the basic nature of resonances, which naturally give rise to this Lorentzian shape [85]. Moreover, the width of the Lorentzian offers valuable information, it ties directly to the resonance's lifetime. Thus, when interpreting FMR measurements, employing a Lorentzian function generally provides a good description of the measured data, but also provides key insights into the magnetic properties of the material under investigation. Full width at half maximum (FWHM) provides an estimate of the linewidth, which is related to the damping parameter in the LLG equation. The gyromagnetic ratio is needed to calculate the damping, so the Kittel fit must be performed before the linewidth can be fitted. The linewidth is related to the Gilbert damping parameter (α).

Fig 5.3 shows examples of the field-dependent line-shape. At each frequency the absorption is well fitted with a Lorentzian line-shape function and quadratic background as described in chapter 2 and the residual plot below each dataset confirms the quality of fit. The correlation plots (lower right of each frame) can be seen as navigational charts, delineating the relationships among varied variables. A circular shape reveals the absence of correlation, while an angular shape indicates a pronounced correlation. These suggest a primary correlation between the width of the absorption peak and its amplitude, indicating that variation in the fitted amplitude will trigger corresponding variation in width. Contrastingly, the positioning of the peak is found to be correlated with the mixing angle as well as elements of the background. In the histogram plots (lower left of each frame) a Gaussian-like shape, that is smooth, indicates that monte-carlo samples have been taken to accurately determine parameter values and their associated uncertainties. It also signals that none of the parameter values are restrained in an artificial way. Monte Carlo sampling is used to estimate complex systems or find solutions to problems with random and uncertain data. It works by generating a large number of random samples or simulations to estimate specific quantities or probability distributions. In FMR analysis, Monte Carlo simulations can be applied to model magnetic systems. By subjecting the model to Monte Carlo simulations and comparing the simulated data to experimental FMR measurements, we can extract an improved estimate of the uncertainties in fitting parameters in the model, ultimately leading to a better understanding of the material's magnetic behaviour and its response to external conditions. This makes it a valuable tool for studying magnetic materials. Within the main panels of figure 5.3, the green absorption line corresponds to the

energy consumption of the system across the field at fixed frequency. By measuring the microwave absorption as a function of both the microwave frequency and the applied external field, we are indeed able to determine the FMR dispersion and, consequently, obtain valuable information about the magnetic properties of the material under investigation; the dispersion line is shown as a yellow colour. The black line in the plot shows a fitting to the line shape, representing the best fit. The variability in the best fit parameters, essentially the uncertainty or error in the curve, is exhibited by the red lines; these are generally not clearly visible in a good fit. Below these, the normalized residuals are indicated in black, with the spread or range of these residuals, based on the red lines, shown in red. In FMR, the Gilbert damping parameter is measured from the frequency dependence of the FMR linewidth (often measured as the full width at half maximum, or FWHM, of the resonance peak). In a system that primarily experiences Gilbert damping, the FWHM increases linearly with frequency. Figure 5.4 exhibits the same line shape illustration, but it is employed on an alternate dataset that, as we should shortly see, showcases a different frequency-dependence to the linewidth. The absorption line-shapes are well represented by a Lorentzian line-shapes on a quadratic background. In Figure 5.4, our correlation plots confirm that the linewidth shares a strong correlation solely with the amplitude. Furthermore, the histogram plots reinforce the credibility of the fits, showing the derived values and their corresponding errors to be convincingly determined without any artificial constraints on the parameters.

Figure 5.3. Each frame shows (upper) fits to the FMR absorption line-shape, with the model, and its various components, as solid lines. Normalised residuals in each case are shown beneath. The lower plots in each frame show histograms (left) for the Monte-Carlo sampling of each parameter, and parameter correlation plots (right). Frames represent data at frequencies across the measured range for a sample with 5 nm Ag thickness, showing a linear frequency-dependence of linewidth.

Figure 5.4. Each frame shows (upper) fits to the FMR absorption line-shape, with the model, and its various components, as solid lines. Normalised residuals in each case are shown beneath. The lower plots in each frame show histograms (left) for the Monte-Carlo sampling of each parameter, and parameter correlation plots (right). Frames represent data at frequencies across the measured range for a sample with Ag thickness 0.6 nm, showing anomalous frequency dependent linewidth.

5.3.3 Magnetic Damping

The absorption linewidths extracted from the field-dependent absorption at each frequency were used to determine the inhomogeneous line broadening. These values, along with the gyromagnetic ratio determined from Kittel fitting, were also used to determine the Gilbert damping parameter. In multilayer structures consisting of FM layers and a NM layer, the FMR frequency and linewidth can be influenced by the NM thickness.

Fig.5.5(a) and (b) represent the frequency-dependent linewidth for a range of CoFe/Ag/CoFe trilayer samples with different Ag thicknesses, separated into two classes based on the form of the frequency-dependence. The figures illustrate that as the frequency increases, the linewidth also increases. Fig. 5.5 (a) exhibits a linear relationship between frequency and linewidth, while a linear dependence can be understood in terms of an effective Gilbert damping, the anomalous enhancement of damping at intermediate frequencies - a bump is seen in Fig. 5.5 (b). The linewidth in FMR measurements provides information about the homogeneity and dynamics of the magnetization in a sample. Typically, in the FMR, the linewidth tends to increase as the frequency increases. The frequency increases, energy loss occurs at an accelerated pace due to various mechanisms, resulting in increasing of the linewidth. The relationship between the resonance frequency and the applied magnetic field strength in both sets of samples is well represented by the Kittel formula, which demonstrates that the resonance frequency increases with an increase in the applied field, as described by equation 5.1.
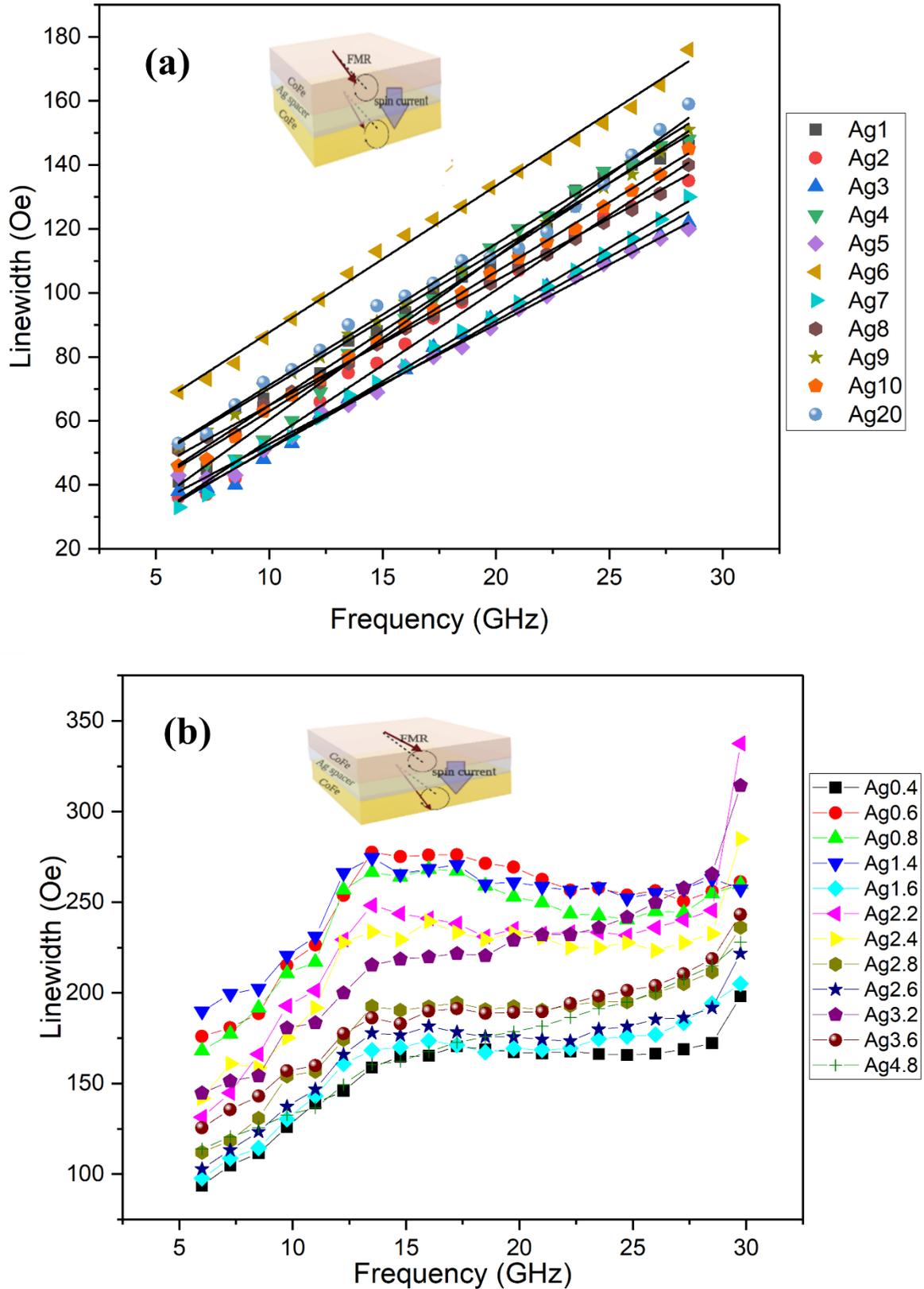
Figure 5.5. (a) and (b) show a selection of the main data and FMR measurements relating to variations in linewidth with frequency for the thin film. Also, (a) shows the subset of the samples where the frequency-dependence of the linewidth follows a conventional linear trend, and (b) shows the subset of samples where it does have an anomalous 'bump' at intermediate frequencies.

The unusual bump visible in Figure 5.5 (b) signifies a peculiar increase in damping at certain frequencies. This unexpected trend disrupts the usual damping characteristics we would typically see in FMR studies, where damping tends to increase steadily with increasing frequency due to established mechanisms both internal and external to the system [33]. In this case, the appearance of the bump could suggest the presence of an additional mechanism at play, influencing the behaviour of damping within these specific frequency ranges. It is possible that this could be a result of various phenomena such two-magnon scattering and spin pumping at the interface. Two-magnon scattering is a phenomenon where a spin wave quantum, or magnon, divides into two or more magnons [86]. This event can cause an alteration in energy from the macroscopic precession of magnetization to the microscopic spin waves, thus increasing the system's overall damping. In terms of spin pumping at the interface in a system composed of FM and NM layers, the precessing spins from the FM layer can inject spins into the adjacent NM layer. This momentum exchange process could lead to energy reduction, which is observed as an increasing in damping. Both mechanisms are potential contributors to the observed enhanced damping in the system.

In Fig.5.5(a), the linewidth shows a variation of approximately 80 Oe over a range of around 25 GHz. Similarly, Fig.5.5(b) exhibits a roughly analogous degree of variation in the linear part of the linewidth. This similarity suggests that the Gilbert damping, an intrinsic property that represents the loss of magnetic energy within a material, should be comparable for both the linear and non-linear samples. However, a noticeable difference can be observed in the inhomogeneous linewidths of the two figures. In Fig 5.5(a), the inhomogeneous linewidth, representing the distribution of local field variations within the sample, is relatively small. In contrast, Fig 5.5(b) displays a much larger inhomogeneous linewidth. This could be indicative of a greater degree of local field variations in the sample represented in Fig 5.5 (b). This will be investigated quantitatively in section 5.3.5.

5.3.4 Magnetic Damping in Literature

The chapter focuses on the dependence of precessional damping on the thickness of a non-magnetic Ag layer in CoFe/Ag/CoFe trilayer system. We have observed in Fig 5.5(b) a novel frequency dependence of the magnetic damping, where at certain Ag thicknesses, the resonance

linewidth is enhanced at intermediate precession frequencies, remains constant, or slightly reduces as the frequency increases, and then regains the expected linear frequency-dependence at higher frequencies. In simple ferromagnetic materials under the influence of an external magnetic field, the magnetic moments gradually align with the field direction. As the field strength increases, more and more moments align until a point is reached where all moments are aligned. This is the saturation point, and further increasing the field strength does not increase the magnetization. However, in a system with noncollinear configurations, the interactions between different magnetic moments, and between the moments and the applied field, can become quite complex. These interactions, especially when combined with dynamic exchange interactions between different layers, could potentially impede the alignment of the moments with the field.

Moments might be in a particular noncollinear configuration due to the exchange interactions, making it harder for them to align with the field. Moreover, if the system has a significant degree of magnetic anisotropy, preferred directions of magnetization due to crystal structure or shape, reaching saturation can be more difficult when the field is applied in a hard direction, a direction that is not a preferred axis of magnetization. In such a case, the saturation field, the field required to reach the saturation [72], can be significantly larger than when the field is applied in an easy direction .

The magnetization dynamics of a trilayer system consisting of a NiFe(5nm)/Pt (5nm)/CoFeB(5nm) trilayer on a substrate have been evaluated by measuring the FMR [87]. They found that the Pt layer causes ferromagnetic coupling between the two ferromagnetic layers due to the magnetic proximity effect. The magnetic damping constant for the NiFe layer showed a significant enhancement with increasing microwave power, which was explained by the temperature dependence of a weak ferromagnetism in the Pt layer induced by the magnetic proximity effect. For an Ag spacer layer, we do not anticipate significant proximity-induced magnetism, and so this mechanism can be disregarded. A different study focussed on the static and dynamic magnetic properties of a CoFe (10nm)/Ru(0-3nm)/CoFe(5nm) trilayer sample. An interesting observation was the non-linear relationship between the remanence ratio, defined as the ratio between the hard and easy axes, and the thickness of the Ru layer, suggesting the presence of biquadratic coupling; it is an interlayer coupling that causes moments to align orthogonal to one another in the sample plane, as opposed to aligned or anti-aligned [88]. The damping factors peaked at a certain thickness of the Ru layer, suggested as being due to the impact of dynamic interlayer exchange coupling on the behaviour of

magnetization dynamics. Another study focused on the FePt(40nm)/Cu(5nm)/FeNi(20nm) trilayer structure and explored the modulation of magnetic parameters, including damping and effective field, via investigating the angular dependence observed in broadband ferromagnetic resonance measurements. There the occurrence of spin-pumping resulted in an augmented linewidth. Mutual precession led to a collective reduction in the anisotropy field for both the FePt and FeNi layers [34]. In the Fe/Pd/Fe trilayer structure, the Pd layer influences the magnetic relaxation in this system. A noticeable change was observed in the Gilbert damping around the characteristic length pertaining to static interlayer exchange coupling in the Fe/Pd/Fe structure. The substantial variations in Gilbert damping values were attributed to the entwined dynamics of the two Fe layers, governed by both static and dynamic exchange coupling [89].

The intrinsic and extrinsic damping mechanisms in the FM/NM layers are augmented by spin-orbit coupling and interfacial d-d hybridization. These processes occur at the interface and are subject to potential impacts from topological irregularities and intermixing. These alterations can modify the electronic structure at the interface. Additionally, the phenomenon of spin pumping, wherein angular momentum is absorbed from the precessing magnetization, can also intensify damping. In this situation, d-d electron hybridization serves a critical role as it not only occurs at the interface of the FM/NM layers but is also affected by any present surface unevenness or intermixing. Through these mechanisms, the hybridization alters the interface's electronic structure, and the process of spin pumping boosts the damping by absorbing angular momentum from the magnetization's precession. The effect of d-d hybridization on damping can display frequency-dependence. As frequencies increase, d-d hybridization might introduce additional damping paths, thus shaping the resulting spin dynamics in a characteristic way, such as anisotropic effect and shifting the resonance peaks. This highlights the multifaceted role of d-d hybridization in the context of frequency is important to study the magnetic damping [90]. However, in the work presented in this thesis, focus is not on investigating d-d hybridisation; the experiment involves keeping the FM layers thicknesses constant while varying the thickness of the Ag layer. As a result, the degree of d-d hybridization remains relatively unchanged throughout the investigation. Instead, the primary objective is to explore the impact of varying NM thickness on the magnetic properties and interactions within the multilayer structure. Furthermore, the d-d hybridization might also vary with changes in the thickness of the Ag layer. However, it is important to note that as long as Ag is continuous there should be no impact.

5.3.5   Analysis of FMR Measurements

The thickness of Ag layer in a trilayer structure can influence several damping mechanisms, which includes spin pumping (or spin relaxation) and those related to the crystal structure, such as inhomogeneous broadening and two-magnon scattering. The process of spin pumping could see its efficiency affected by the thickness of the Ag layer. NM layer possesses a unique spin diffusion length, representing the extent to which spin signals can propagate without considerable decay. When the thickness of the Ag layer is less than Ag's spin diffusion length, signals can traverse the entire Ag layer with minimal loss. However, the Ag layer's thickness can also influence the interface quality between the FM and the Ag. A thinner Ag layer might result in a cleaner interface, promoting enhanced spin transport. In opposition, a thicker Ag layer could introduce a more uneven interface or a greater chance of defects, both of which may reduce spin pumping efficiency and cause spin decoherence. Also, in very thin Ag layers, magnetic coupling between the ferromagnetic layers might be more pronounced. This could complicate the spin dynamics at the interface and influence the efficiency of spin pumping. It is clearly expected damping parameters from similar material systems in literature, which typically fall between 0.001 to 0.1 [87, 91, 92]. These parameters reflect the conversion of magnetic energy to lattice energy during magnetization precession, the larger the damping parameter, the faster the energy dissipation and subsequent relaxation of magnetization. This discrepancy in non-linear frequency dependence of the linewidth observed in our research may be attributed to a multitude of factors.

To be able to compare between samples with bump and linear behaviour, we need to define an effective damping. In Figure 5.6, an analysis is employed to approximate the inhomogeneous and Gilbert damping in non-linear sample sets. This is achieved by focusing on the assumed linear segments of the data spectrum, particularly at the outermost frequency ranges, avoiding the anomalous bump region. By doing so, one can determine a reasonable comparison between datasets that exhibit this bump feature and those adhering to a more traditional linear trend. From the data fitting, two important parameters appear: the effective Gilbert damping from the slope, and the effective inhomogeneous linewidth, determined by the intercept.
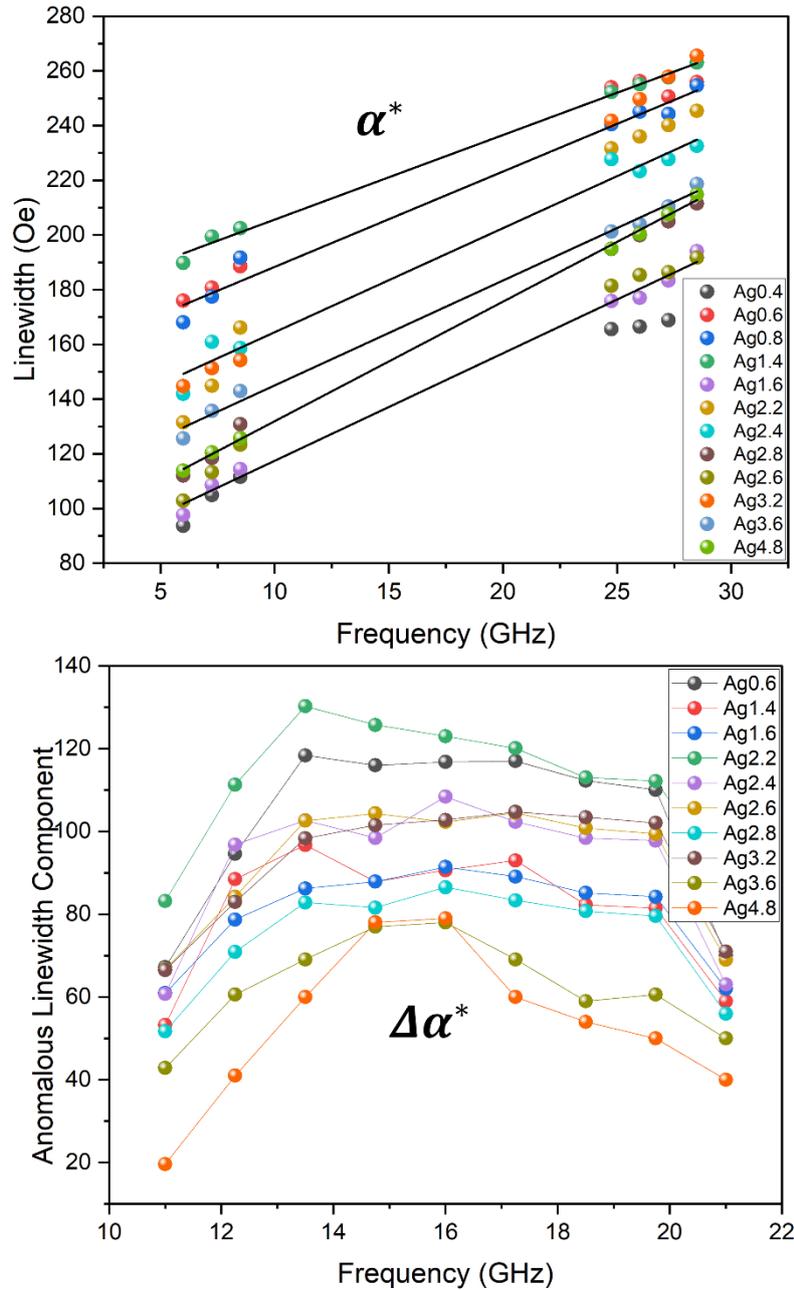
Figure 5.6. Demonstrating an instance of fitting non-linear frequency data to deduce the effective damping parameter can illustrate how α^* and $\Delta\alpha^*$ are determined.

From the analysis in fig 5.6, we can find the dependence on the Ag layer thickness of the effective Gilbert damping, the effective inhomogeneous linewidth, and the bump amplitude. As we have discussed earlier, to determine the damping in the non-linear frequency regime, within the linear frequency domain, a linear fit to the data represented as α^* was employed. By the taking the other bit of the data characterized as the 'bump' and subtracting off linear fit α^*, we were able to recognize the magnitude of the non-linear influence on the system for each sample. Figure 5.7 provides a visual representation of amplitude values derived

from bump data corresponding to non-linear frequency samples. The amplitude is consistently in the region of 30-50 Oe, suggesting that whatever may be the mechanism of the bump it produces a reasonably consistent contribution to the overall linewidth independent of the Ag thickness. In other words, the amplitude does not appear to vary with Ag thickness beyond random fluctuations caused by its extraction method. This is consistent with a spin-pumping model, as the Ag thickness is considerably less than the spin-diffusion length. It is also consistent with varying anisotropy as only a weak AF coupling would be required to cause anisotropy in the early stages of top FM growth.
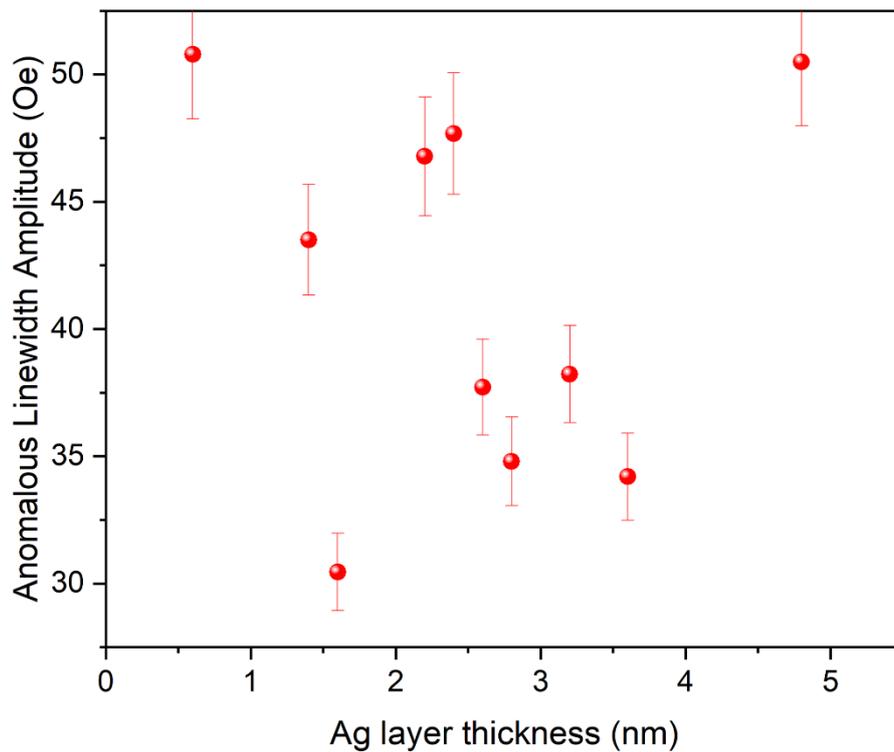

Figure 5.7. Amplitude values for the bump data of the non-linear frequency samples.
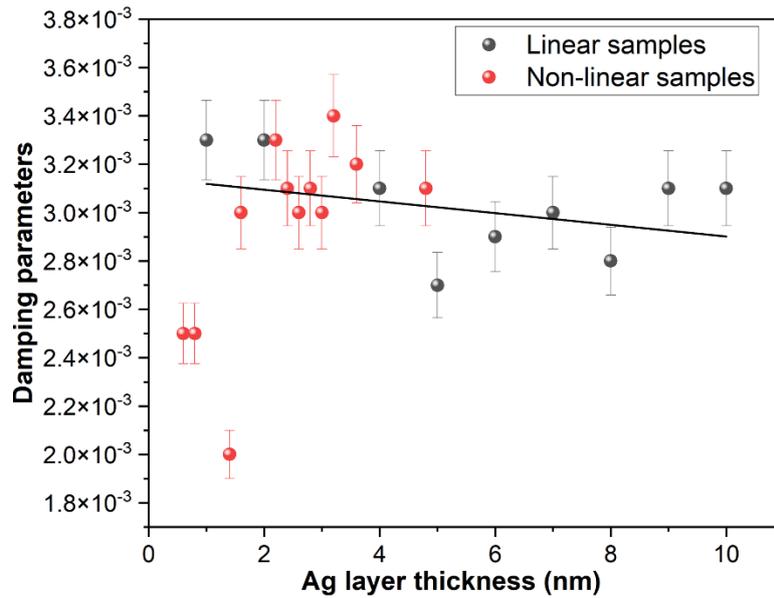
Figure 5.8. representing the damping parameters for CoFe/Ag/CoFe with respect to NM layer thickness could provide a meaningful perspective on the relationship between the thickness of the NM layer and the ensuing effective damping.

The results depicted in Figure 5.8 illuminate the relationship between effective damping and the Ag spacer thickness. In samples demonstrating linear frequency dependence and non-linear frequency dependence, effective damping seems relatively unaffected by the thickness of the layers. This behaviour suggests the consistency of intrinsic factors, like Gilbert damping, which are a fundamental property of FM material. However, the first three samples presenting non-linear frequency dependence, there was a noticeable difference in the effective damping range. This variation can be recognized as an artefact of the approach we adopted, where we focused on fitting a limited subset of the data. In a comparison of Gilbert damping values derived from our study with those reported in previous studies, there are visible variations. Our non-linear samples demonstrated damping values ranging from 0.0020 to 0.0034, while the linear samples displayed a tighter spread from 0.0027 to 0.0033. Contrarily, earlier study documented values in the slightly elevated of 0.004 to 0.005 [65]. This indicated that Gilbert damping remains fairly consistent throughout most samples and does not change greatly with Ag thickness.

The spin-diffusion length provides insights into spin transport properties, facilitates the understanding of spin dynamics, and has implications for the development of spintronic devices. In systems where the thickness of the Ag layer is considerably smaller than the spin-diffusion length, the spins do not have sufficient distance to lose their initial phase coherence

significantly. This implies that the spin signal, which is associated with the coherence of the spins, may not show a substantial change, or decrease even as the thickness of the Ag layers changes. This is because the spins can traverse the thin layers without undergoing substantial dephasing. Hence, in such systems, the layer thickness may have a less pronounced or observable impact on the amplitude of the spin signal. This explains why there is no clear thickness dependence seen in figure 5.8. For the samples with non-linear frequency dependence, the effective damping values remain stable, indicating that the mechanism for the anomalous damping enhancement is different from the typical Gilbert damping. This contrasts with bilayer spin-pumping, where this increase is seen as an enhancement of the effective Gilbert damping.

In a multilayer system, each layer can have its own resonance frequency. When these frequencies overlap, it can enhance the interaction between the layers and affect the overall behaviour of the system. For instance, it can increase the strength of the spin pumping effect or lead to more complex dynamic behaviour. In a coupled system, the interaction between the components can lead to collective oscillations that resemble the propagation of acoustic and optical modes. These modes are a result of the coupling between different components of the system. When excited, these modes can influence the system's dynamic response and lead to more complex behaviours.

5.3.5.1 Mechanisms for non-linear frequency dependent linewidth

Where non-linear behaviour is apparent, the damping can increase proportionally with the amplitude of magnetization precession. Such a situation might be applicable to our samples. Our measurements were primarily conducted at a microwave power of -5dBm. The power we used was roughly the same as that used in previous studies in the field [93], where the range was -11, -5, and -4 dBm. To validate this assertion, we performed additional measurements at varying power levels (-11, -6 and -5dBm). Interestingly, no discernible difference was noted in the observed behaviours, indicating that the influence of microwave power on the magnetization dynamics of our samples can be eliminated. In previous FMR investigations, non-linear frequency-dependent linewidths were observed in samples such as CoFeAl [94] and CoFeGe [95] films. For both studies, the linewidths were observed with the saturating magnetic field oriented in the film plane. However, in Ref. [95], out-of-plane measurements revealed a linear linewidth. In both instances, the observed frequency-dependent linewidths were linked

to the effects of two-magnon scattering. This study has relaxing impurity mechanism which could be the possible mechanism for the bump in our data. The slow-relaxing impurity mechanism refers to a specific damping process in ferromagnetic materials. This mechanism is driven by thermal fluctuations that lead to the longitudinal relaxation of impurity atoms. These impurities are exchange-coupled to the ferromagnetic lattice, resulting in an exchange anisotropy. This anisotropy affects the energy levels of the impurity, causing them to split or change based on the current direction of the magnetization. It is unclear how a slight variation in Ag layer thickness in our samples would lead to a significantly different impurity concentration within the surrounding FM layers.

The phenomenon of two-magnon scattering could also contribute to an increased resonance linewidth. In this phenomenon, interactions or scattering events between spin waves lead to enhanced damping. This effect intensifies with the increase in magnetization precession amplitude, a characteristic that may be relevant for our non-linear samples. In the theoretical study by Landeros et al.[96], two-magnon scattering appears as a pronounced influence on the FMR linewidth, especially when magnetization adopts an orientation partially out-of-plane in low fields. This distinct behaviour is evident as a noticeable bump in their data. The interaction between the two magnons scattering is influenced by the angle between the magnetization and the film plane. When the magnetization is out-of-plane its effect is typically small. The contribution of the two-magnon scattering to the FMR linewidth displays a pronounced variation based on the orientation of the magnetization and the external field relative to the plane of the film, as illustrated in Figure 5.9. The noticeable effect or bump caused by this scattering; the field should be applied at an angle ranging from 60 to 70 degrees from the sample's plane as explained in [96].

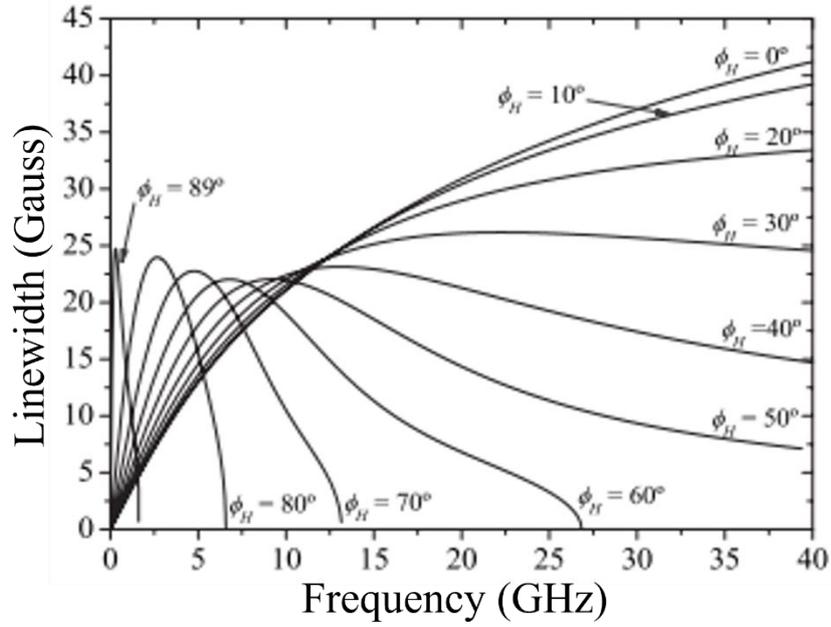**Figure 5.9.** the frequency dependence of the two magnon contribution to the FMR linewidth (adapted from [44])
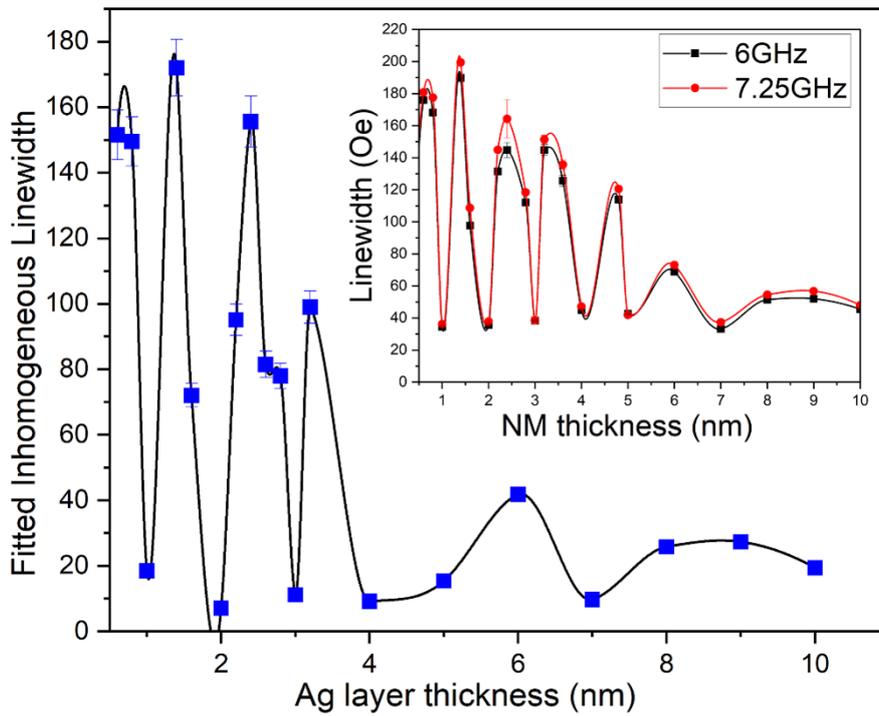

Figure 5.10. shows the relationship of the inhomogeneous linewidth with Ag thickness and the inset plot shows the behaviour observed in the linewidth at 6 and 7.25 GHz, which depends oscillatory on the thickness of the NM layer in the CoFe/Ag/CoFe trilayers, could potentially signify the impact of RKKY.

In Figure 5.10, the relationship between the effective inhomogeneous linewidth and the Ag thickness for samples showing non-linear frequency-dependent linewidth is depicted. Such oscillations, observed within the CoFe/Ag/CoFe trilayered structure, could be related to the RKKY interaction. Additionally, the inset illustrates an oscillatory behaviour in the linewidth at frequencies of 6 and 7.25 GHz , which can be expected to show a similar behaviour to the inhomogeneous damping. This underscores the robustness of the linear fit applied to the extremes part of the bump data. The understanding and appropriateness of the linear fit further enhance our confidence in the observed oscillatory behaviour and its potential implications, suggesting that the variations seen might indeed be an outcome of RKKY-mediated interactions within the trilayer. Thus, the thickness of Ag plays a critical role in the effective magnetic damping of the trilayer samples. The RKKY interaction can cause moments in different layers to tend to align or anti-align, affecting the overall magnetization dynamics of the system. Therefore, it has a different impact on magnetization dynamics than spin-pumping does. When the RKKY occur, the observed variation in the inhomogeneous linewidth can be attributed to the inherent anisotropies in the upper CoFe layer. The RKKY interaction causes a spread in the easy axis directions in the upper layer, since the magnetization of cluster during initial growth can be turned either left or right from the magnetisation of the first layer. This then gives a spread of easy-axis directions which contributes to the inhomogeneous linewidth.

A possible explanation also for the enhanced damping is that the RKKY interaction influences the alignment of the easy-axis in the second FM layer during its initial growth stages, causing it to turn from the easy-axis of the first FM layer. This misalignment results in different resonant conditions for the precession of the two layers [97]. Consequently, several phenomena can occur, including the induction of spin-pumping effects, the overlapping of resonances, and the excitation of acoustic and optical modes. It is crucial to acknowledge that the potential impact of the RKKY interaction on the damping is currently speculative, and there is a lack of direct evidence supporting this hypothesis. But, investigating these possibilities can provide valuable insights into the complex interplay between the RKKY interaction, the misalignment of layer easy-axes, and the varied resonant behaviours observed in the system. Such investigations, including techniques like PNR or PNR-PA, can deepen our understanding of the underlying mechanisms and dynamics in multilayer structures. The next chapter of our study will explore the combination of PNR and PNR-PA measurement to investigate the potential of magnetic coupling across a non-magnetic spacer in adjusting the resonance linewidth for non-linear frequency dependent samples.

Chapter 6: X-ray and neutron reflectometry study of CoFe/Ag/CoFe with weak antiferromagnetic coupling

6.1 Introduction

In this chapter, the fitting procedures and resulting data from XRR and PNR-PA measurements performed on the CoFe/Ag (2.6nm)/CoFe sample system is investigated. The work on this chapter builds on the descriptions of the fundamental principles outlined in chapter 3. The discussion here starts with an overview of the related literature providing the framework for the following analysis of the experimental methods and data analysis. The techniques harnessed in the study are described, leading to the disclosure of empirical findings associated with parameters such as thickness, roughness, and density. In this chapter, a CoFe/Ag/CoFe system was studied to examine the variations in the structural and magnetic scattering length density (SLD), that is a determine of the density of scattering centres within a material. It is used to illustrate both atomic and magnetic structures in materials. For atomic structure, SLD is related to the arrangement of atoms and their electron density for x-rays, nuclear density for neutrons. In the case of magnetic structure, it includes information about the local magnetization. The data analysis involved fitting various structural models of the sample to the experimental data to determine the best fit. The results indicated a change in the structural SLD at the interface between Ag and CoFe layers and polarisation analysis allowed investigation of the anisotropy by rotating the sample.

6.2 Background

Spintronic devices have recently attracted considerable interest due to their promising applications in revolutionizing data storage, computing, and communication sectors. A critical factor in designing and optimizing these devices involves understanding the magnetic and structural attributes of thin films and interfaces. In this regard, neutron reflectivity techniques have become a potent and adaptable method, providing exclusive perspectives into these properties, and allowing researchers to investigate the performance of non-magnetic and ferromagnetic materials employed in spintronic device [98, 99]. PNR provides a means to assess layer thickness, interfacial properties, and variations in composition. The addition of polarisation analysis provides depth sensitive vector magnetometry making it a valuable resource for exploring magnetic arrangements, domain formations, and the direction of

magnetic moments [39, 53]. PNR-PA is less commonly used than conventional PNR due to the extended counting times required, and the difficulty in using small devices.

Additionally, PNR-PA supports other characterization approaches, such as x-ray reflectivity (XRR) and x-ray diffraction (XRD), by supplying extra information on a material's characteristics. This complementarity allows a more thorough understanding of materials and their performance in various environments and applications. PNR-PA also enables in-situ and in-operando measurements, which allows for the investigation of materials and their properties under different external conditions like temperature, pressure, and applied fields [39, 100]. This capability is essential for understanding the behaviour of materials in practical applications and for the development of more sophisticated materials and devices.

Previously, PNR-PA has been used to determine the vector magnetization for examination of exchange bias in magnetic double superlattices that are sputtered. The structure of these superlattices is such that a ferromagnetic superlattice is constructed over an antiferromagnetic superlattice where the magnetization of adjacent layers is anti-aligned via the RKKY interaction. Exchange bias is a peculiar effect where the hysteresis loop of a ferromagnetic substance is displaced along the magnetic field axis [101, 102]. Typically, it is noticed when a ferromagnetic material is closely juxtaposed with an antiferromagnetic one. This unique bias is thought to emerge from the coupling at the interfaces of the ferromagnetic and antiferromagnetic materials. The study indicates that the system displays a parallel domain wall and a spin flop transition. The spin flop is the phenomenon of the reorientation of spins in antiferromagnets due to an external magnetic field. However, these two manifestations are not directly tied to the exchange bias observed. Instead, a substantial anisotropy in the antiferromagnetic block appears to be critical for the triggering of the exchange bias [102]. This particular work is explained in more detail since the approaches used are similar to our study.

The spin arrangements in these double superlattices were determined from a combination of energy minimisation calculations, MOKE and PNR-PA measurements. The gathered data facilitated the direct viewing of a magnetic parallel domain wall. Remarkably, this study provided the first experimental corroboration of the theories proposed by Mauri et al [103]. This theory proposes that inducing a certain degree of anisotropy into the antiferromagnetic superlattice is a prerequisite to stimulate an exchange bias in the structure. Furthermore, the study underscored that in the absence or near-absence of anisotropy, the spin

flop phase is present in the antiferromagnetic material. In conclusion, the observed phenomena of the parallel domain wall and the spin flop phase, though intriguing, do not have a direct correlation with the exchange bias [102] . The exchange bias, instead, is more likely linked to the level of anisotropy in the antiferromagnetic layer.

Several studies have utilized the PNR technique to illustrate the variations in in-plane magnetization of samples based on depth. An examination of the interfacial magnetism in an exchange bias system, specifically at the interface between Fe_3O_4/NiO (FM/AFM), revealed alterations in magnetization. Additional inquiries in ferromagnet/semiconductor [104] and ferromagnet/normal metal [105, 106] structures identified shifts in the magnetic depth profile at the interface, thereby affirming the potential of PNR for studying the effect of the presence of magnetic dead-layers or proximity induced magnetism. The in-plane anisotropy induced at the FM/semiconductor interface causes the magnetisation to align along a certain crystallographic direction. By aligning the easy-axis along the beam direction, the magnetization is held along the beam and so scattering appears in the spin-flip channel in PNR-PA [106, 107]. Consequently, initial explorations into the magnetization and the magnetic asymmetry at varying interfaces started employing the PNR technique.

The aim of the work described in this chapter is to use a combination of PNR and PNR-PA to studying the enhanced linewidth observed in CoFe/Ag/CoFe with weak AF coupling. In the case of CoFe/Ag(2.6nm)/ CoFe sample, one suggested explanation is that antiferromagnetic coupling across the Ag layer causes the magnetizations of the CoFe layers to precess in anti-phase, leading to linewidth enhancement due to spin-pumping [72]. Also, the RKKY interaction could result in the formation of unique easy axes within the ferromagnetic layers which develop during the deposition process. This occurrence might cause the overlap of two slightly different resonances, thereby broadening the apparent linewidth. However, it is essential to note that the coupling intensity of the RKKY interaction, especially in metallic materials like Ag, tends to be weak and therefore full antiferromagnetic alignment of the two layers, easily observed in a magnetic hysteresis measurement [108].

6.3 Experimental Details

In this chapter, multilayer as deposited CoFe/Ag(2.6nm)/CoFe trilayer sample was investigated. All samples were analysed using the methods outlined in chapter 2. The same set of samples were studied by MOKE, X-ray reflectivity and diffraction, and PNR-PA.

In XRD analysis, the thickness of the material being studied can have an impact on the observed diffraction patterns. To investigate this effect, it is common to vary the thickness of the material of interest and analyse how the diffraction patterns change accordingly. This approach helps in understanding the influence of thickness on the crystallographic properties of the material. In our specific case, a range of Ag thicknesses was used in the XRD analysis. By analysing the diffraction patterns obtained from each sample, it is possible to observe how the diffraction peaks change, broaden, or change in intensity as the Ag thickness changes. On the other hand, for the PNR-PA analysis only one thickness was used which is Ag (2.6nm). This is a sample with enhanced linewidth, so where we anticipate nominally AF RKKY coupling, but also the Ag is sufficiently thick that the interfaces are well formed, and the spacer layer is resolvable in PNR/PNR-PA.

6.3.1 X-ray reflectivity

The XRR performs as a non-invasive approach for determining the depth-dependent density profiles of the samples. This study used XRD analysis to determine the out-of-plane lattice parameter and analysed thin-film samples of CoFe/Ag/CoFe using XRR to determine their thickness and interface roughness. XRR data provides information on CoFe/Ag/CoFe layers. This information is obtained from fitting using a model based on chapter 3 which includes the layer thicknesses and roughness for the FM/NM/FM multilayers.

The complexity of the interface characteristics between ferromagnetic and non-magnetic layers plays a critical role in shaping the performance of FM/NM/FM multilayer system. The interface roughness directly affects the magnetic exchange coupling, which is an interlayer interaction where the magnetic orientation of one layer affects that of the other layers [15]. The roughness can either enhance or hinder this coupling, depending on the nature and scale of the roughness. For example, if the interface roughness is comparable to the length scale of the magnetic exchange length, it can strongly disrupt the exchange coupling, leading to a decrease in coupling strength. The typical exchange length λ for CoFe would be approximately 20 nm [10, 109]. Interface roughness also induces random magnetic anisotropy due to the

variation in the local atomic coordination which refers to the arrangement and bonding of neighbouring atoms around a given atom in a material. This should affect the magnetic orientation and coercivity of the material. This effect is more pronounced in very thin films, and materials with high magnetic anisotropy [82, 110]. Likewise, the quality of the interface also impacts the electronic transport properties of the multilayer, with imperfections or increased roughness potentially leading to elevated scattering of electrons and spin-mixing conductance.

The impact of interfacial irregularities on antiferromagnetic (AF) coupling is closely related to the inherently short-range property of the exchange interaction, which primarily functions within a limited range of a few atomic distances. When interface roughness exists within a minor scale, equivalent to a few atomic layers, it indicates a near-smooth atomic surface. when the roughness is small, the layers behave as if they are uniform, and the coupling is uniform laterally. When the layers are rough then the effective thickness of the spacer varies laterally, and the coupling is also then spatially non-uniform. This, in turn, weakens the coupling between these layers or potentially disrupts it entirely, leading to a diminished or wholly lost AF coupling. As a result, there might be an observable change in the multilayer's magnetic properties, including its coercivity and electrical properties.

The influence of interface roughness is multifaceted and can differ based on the exact materials involved and the characteristics of the roughness. For example, specific roughness types might amplify AF coupling by creating more routes for coupling or by modifying the magnetic anisotropy. For example, in a previous study of Fe/Cr/Fr sample, The XRR results indicate that when dealing with a film that has high substrate roughness, the buffer layer can partially mitigate the substrate's roughness. In each of the three samples, the peak of the antiferromagnetic coupling is found around a Cr layer thickness of 1.2 nm. There appears to be an almost linear relationship between the increase in interface roughness and the decrease in the strength of the antiferromagnetic coupling [111].

Figure 6.1 shows XRR data and fits for several CoFe/Ag/CoFe trilayers with different Ag layer thicknesses. The data show Kiessig fringe oscillations observed in thin-film XRR studies, display a pattern where they appear closer together as the film thickness increases. This is due to the interference of x-rays reflected from the top and bottom surfaces of the film. In the case of the Ag 5nm sample, the fringes are less clearly defined. This lack of resolution could imply a rougher surface or interface, as the irregularities in film thickness or density can

blur the sharpness of the fringes. On the other hand, for the 7nm Ag sample, the fringes start to be well resolved, indicating a smoother surface or better uniformity in film thickness. This suggests an improvement in the quality of the film compared to the 5nm sample. The 10nm sample shows very well-resolved fringes, suggesting even better uniformity in the film thickness and smoothness of the interfaces. Well-resolved fringes often indicate high-quality thin films with fewer imperfections.
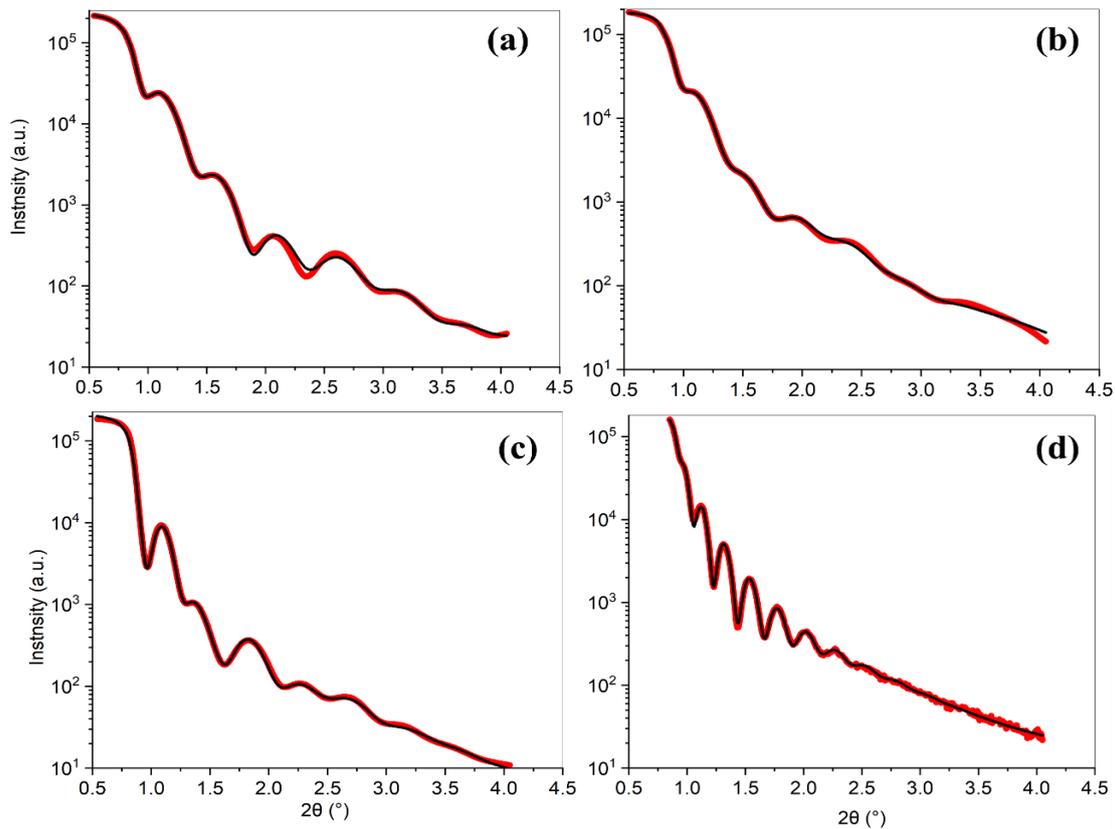
Figure 6.1: X-ray reflectivity data and the corresponding best fitting simulations for various samples of CoFe (10 nm)/Ag/CoFe(10nm) with Ag thickness (a) 4 nm, (b) 5 nm, (c) 7 nm and (d) 10 nm. Data is shown as black markers and best fitting simulation as a red line.

Table 6.1. displays the structural properties of certain CoFe/Ag/CoFe multilayer samples, as determined by fitting XRR measurements; shown as the solid lines in figure 6.1. These properties include the thickness of the CoFe layer (d_{FM}), the thickness of the Ag layer (d_{NM}), and the roughness at the interface between the ferromagnetic (FM) and non-magnetic (NM) layers.

Sample	$d_{FM,upper}$(nm) SiO$_2$/FM/Ag/**FM**	Upper Interface Width FM/NM (nm)	d_{NM}(nm)	Lower Interface Width NM/FM (nm)	$d_{FM,lower}$(nm) SiO$_2$/**FM**/Ag/FM
Ag 4nm	9.20± 0.02	1.03 ± 0.09	3.75± 0.10	0.72± 0.03	9.22± 0.07
Ag 5nm	9.60± 0.09	0.91± 0.05	5.54± 0.06	0.52± 0.07	10.10± 0.14
Ag 7nm	10.30± 0.10	0.85± 0.10	6.10± 0.04	0.64± 0.20	9.90± 0.03
Ag 10nm	9.02 ± 0.07	0.56± 0.04	7.40± 0.10	0.94± 0.08	9.06± 0.10

Table 6.1: The structural attributes of CoFe/Ag/CoFe multilayer samples used in the XRR fitting process. The table includes variations of the Ag layer thickness at 4, 5, 7, and 10 nm.

The results of XRR structural analysis indicate that the interface width of CoFe/Ag/CoFe samples are in the range around 0.5 to 1 nm. The upper interface width, which can be seen as a measure of the interface roughness, decreased as the thickness of the Ag layer increased. In other words, as more Ag was added, the transition from the CoFe layer to the Ag layer became sharper. This could suggest that a thicker Ag layer promotes a smoother interface between the CoFe and Ag layers, possibly due to a more complete coverage or fewer defects at the interface. In several previous studies that used XRR to investigate multilayer systems [112, 113], a similar degree of interface roughness was reported. Specifically, for Ag/Co and various other multilayer systems, the interface roughness fell within a range of 0.4 to 0.85 nm. This range indicates that the interface characteristics in our study are broadly consistent with findings in similar contexts. The slight differences might be attributed to the specific materials employed, the deposition techniques used, or the conditions under which the samples were fabricated.
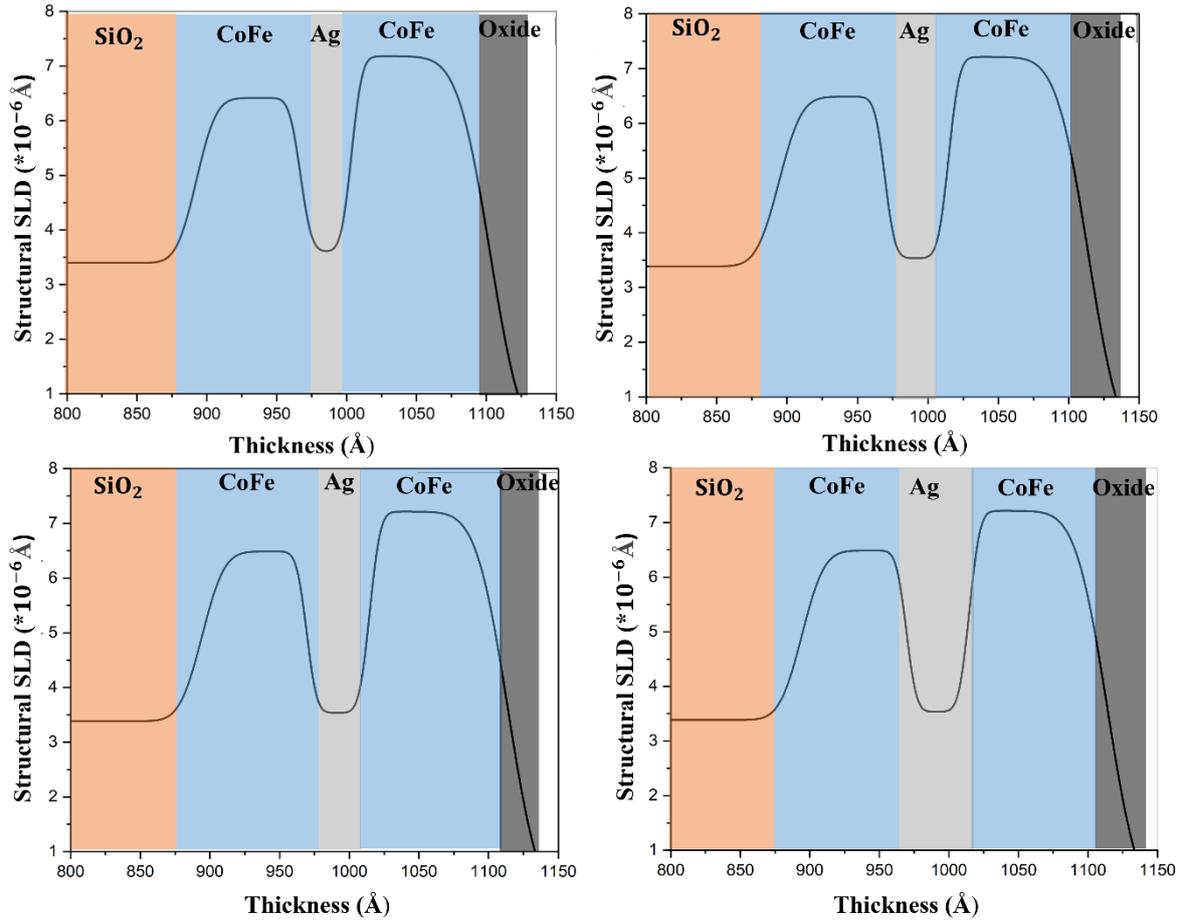
Figure 6.2. Extracted structural scattering density from the best fit simulation of XRR measurement for CoFe / Ag / CoFe trilayered samples grown on Si/SiO$_2$ substrate using GenX simulation.

The structural SLD profiles depicted in Figure 6.2 reveal a substantial consistency between the two CoFe layers in our trilayered samples, implying symmetric interfaces. However, some variability in the Ag layer is noticeable, attributable to the differing thickness and density of the Ag layers in each sample. The presence of intermixing is not definitively substantiated, since the x-ray scattering length in XRR exhibits a continuous variation, making it challenging to distinguish between roughness and intermixing in the specular reflectivity. Examples of magnetic asymmetry at the FM/NM interfaces have been reported [114, 115], despite the minimal measurable differences in the interfacial roughness.

Rotated XRR measurements can yield further insights into a sample's structure. By conducting the XRR measurement with the sample a mounted with the edges at different in-plane angles relative to the scattering plane, we can study both the depth profile and the in-plane structure of the sample. This approach offers additional insights into the lateral structure of the sample, such as the directionality of lateral correlations for rough or intermixed

interfaces. However, interpreting rotated XRR measurements can be quite challenging, as they amalgamate information from both the depth profile and the in-plane structure of the sample. To decipher the relevant structural parameters from the data, a modelling or fitting procedure is usually employed.

As an illustrative example, we considered the CoFe/Ag (2.6nm)/CoFe sample mounted now such that the scattering plane is along the sample diagonal (45 degrees) relative to the edge of the sample. Notably, a fringe periodicity with a spacing around 0.4° was observed. The Kiessig fringes in the XRR profile were more distinct at 2θ values of 0.7°, 1.2°, and 1.7° compared to those from a 0-degree scan. This clarity corresponds to a film thickness of 2.6 nm, inferred from the oscillation pattern of these fringes. In data taken at 0 degree, a primary periodicity of 0.5° was evident. However, the secondary features of the Kiessig fringes were located at different positions on the 2θ scale. More prominent Kiessig fringes were observed around 1.2° and 2.8°, correlating to a thickness of approximately 2.3 nm. The change in Kiessig fringe intensity was not as marked as in the 45-degree scan. Therefore, while both scan results suggest the presence of a layer with a thickness of approximately 2.6 nm, this layer might not be identical when comparing results from the 0-degree and 45-degree scans.
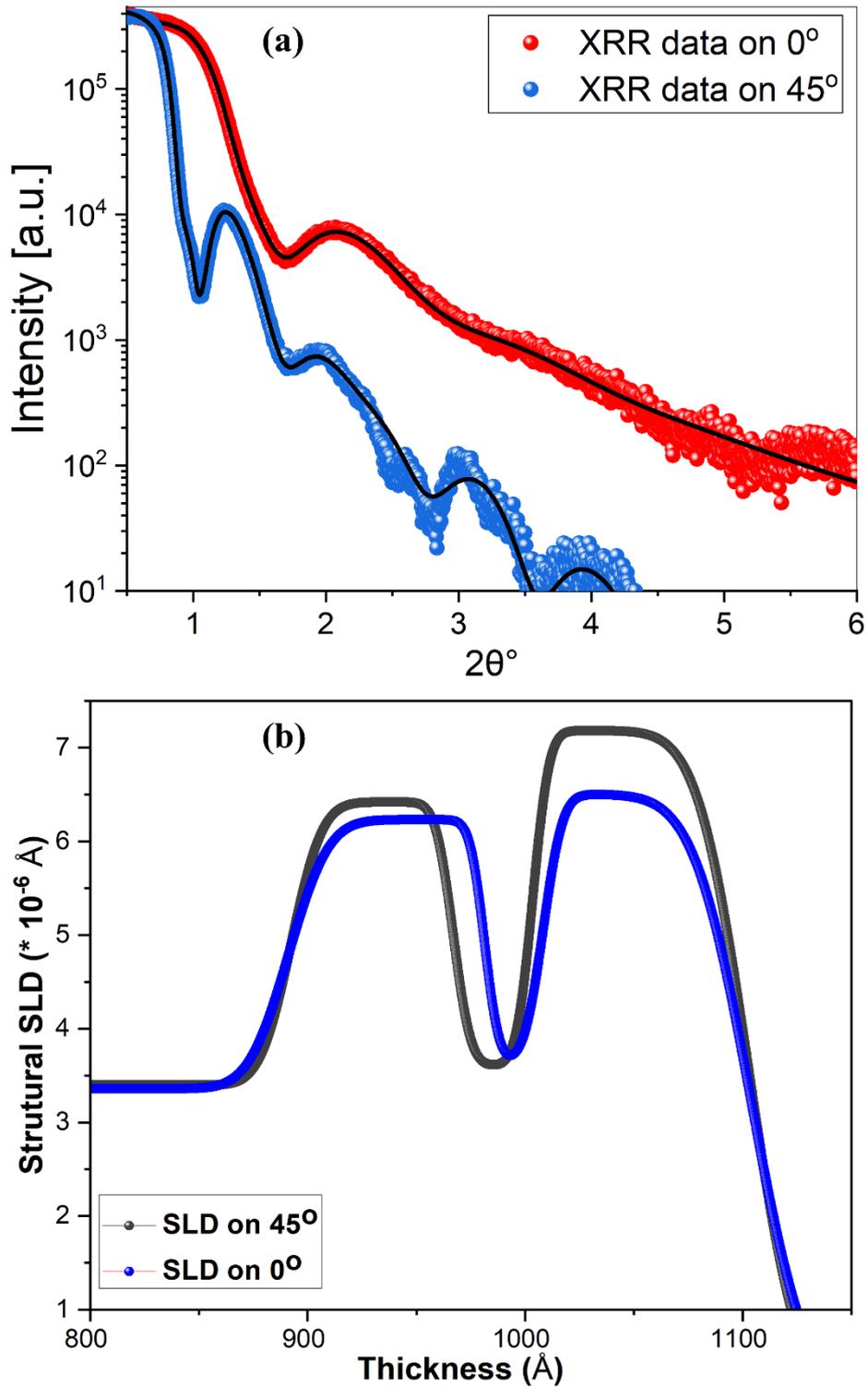
Figure 6.3: (a) X-ray Reflectivity (XRR) measurements and their corresponding best-fit models (black lines) CoFe/Ag(2.6 nm)/CoFe with the scattering plane aligned along, and at 45 degrees to the sample edge. (b) Scattering Length Density (SLD) profiles which produce the best fits shown in (a).

The alteration of a sample's orientation can significantly modify its XRR profile, which is primarily due to the variation in apparent structure of the sample with angle [39]. In multi-layered structures, like CoFe/Ag/CoFe, the XRR profile is sensitive to changes in layer thickness, density, and interface roughness. The rotation of the sample by 45 degrees alters the Kiessig fringe pattern, which suggests a varying directional property changes with respect to the incident x-ray beam and the volume over which it samples. Any inherent structural anisotropy in the sample could potentially give rise to a form of magnetic anisotropy. The properties of the Ag material can significantly impact the XRR profile [82]. The XRR profile can be influenced by aspects such as grain orientation, surface roughness, layer density, and thickness, all of which can be altered by the sputtering process. For example, the grain orientation of a polycrystalline Ag layer, determined by sputtering conditions such as the temperature of the substrate and the deposition rate, can change the interaction of the X-ray beam with the layer. Similarly, the roughness dictated by the sputtering conditions, can lead to a more scattered XRR profile as seen in figure 6.3 for a CoFe/Ag (2.6nm)/CoFe sample. The XRR analysis revealed that the actual layer thicknesses varied from the nominal values initially assigned to the sample layers. The obtained values, which are reported in Table 6.2, suggest an anisotropy of the effective layer thicknesses.

Sample	$d_{FM,upper}$ (nm) SiO_2/FM/Ag/**FM**	Upper Interface Width FM/NM (nm)	d_{NM} (nm)	Lower Interface Width NM/FM (nm)	$d_{FM,lower}$ (nm) SiO_2/**FM**/Ag/FM
Ag 2.6nm at 0°	9.50 ± 0.20	1.09 ± 0.50	2.34 ± 0.10	0.85 ± 0.40	9.80 ± 0.40
Ag 2.6nm at 45°	8.33 ± 0.10	0.65 ± 0.20	2.72 ± 0.08	0.51 ± 0.30	10.2 ± 0.03

Table 6.2: Extracted layer thicknesses and roughnesses obtained from XRR models along different in-plane directions for a CoF/Ag (2.6 nm)/CoFe sample. Each simulated parameter in both the 0-degree and 45-degree measurements is accompanied by an associated error.

The asymmetry observed in the thickness of the non-magnetic layer, as well as the sharper interfaces within the FM/Ag/FM configuration at a 45-degree angle compared to the 0-degree angle, is responsible for the variations in the Kiessig fringe depth's position and prominence. There is discernible visual difference between the data from the two scans. The x-ray beam used measures a thickness that is an average across a large part of the sample [82]. Hence, any inconsistency in the layer thickness across the sample would appear as a broadened interface area. Also, the oxide layers are not expected to show magnetic behaviour when they are at room temperature. Thus, they should not impact the FMR or PNR-PA results [116].

The study revealed a significant shift which showed that the SLD of a 2.6 nm thick Ag layer. The SLD of this Ag layer showed the lower CoFe layer appears thinner for the 45-degree scan. In addition, there was a noticeable change in the height of the upper CoFe layer for both measurements. In the framework of the CoFe/Ag/CoFe structure, the existence of interfaces of the alloys suggests at some sort of behaviour at the interface, possibly a shift in the CoFe alloy composition or the mingling of Ag within the alloy. As this layer's thickness is around the smallest observable detail within XRR, any quantitative analysis of this part is expected to carry larger errors when compared to the inferences made about the bulk Ag or CoFe layers. At this point, the cause behind the alteration in the XRR profile of the CoFe/Ag/CoFe structure upon rotating the sample 45 degrees remains ambiguous. The apparent difference in the thickness of the lower CoFe layer could be the result of a directional roughness or corrugation. The amplitude of the SLD is about the same, with only the apparent thickness varying. The upper layer shows a much higher SLD in the 45-degree scan. This makes no physical sense since the intensity of the SLD is related to the density of the material, which cannot be directional. One can imagine that the two modifications, thickness of one layer and amplitude of the other, are correlated in the fitting. This would suggest that it is that there are several different structural models of the sample which provide similarly good fits showing that all of these analyses are not necessarily absolute and need to be treated with some consideration.

6.3.2 X-ray diffraction

The CoFe and other alloys have different interface widths due to their crystal structures. Changes in atomic arrangements and material properties between CoFe and other alloys that could lead to distinct growth patterns of Ag on these surfaces. CoFe can display either a BCC or FCC structure, depending on composition and circumstances [117, 118]. In our sample we

expect to have BCC CoFe because a higher concentration of Fe. Ag, with its FCC structure, could align more harmoniously for other alloys like NiFe due to the similarity in crystal structures, thus potentially facilitating a more seamless and consistent growth. However, when Ag is deposited on a BCC CoFe structure, the incongruity in crystal structures may give rise to defects at the interface, potentially disrupting the Ag growth pattern and causing irregular formations like clusters or islands [119]. Additionally, the lattice parameter discrepancies between Ag and the two alloys could cause strain in the Ag film, affecting both the film's quality and form. In the specific case of CoFe and Ag, their overall lattice parameters differ (0.286 nm for CoFe and 0.408 nm for Ag) [120].

Figure 6.4 presents the XRD results for CoFe/Ag, which reveals four diffraction peaks, with the first peak corresponding to the (222) crystal plane of CoFe, the second peak representing the (111) crystal plane of Ag, the third peak indicating the presence of the substrate (a Si wafer), and the last peak associated with the (311) crystal plane of Ag. The observation that CoFe has a preferred (111) texture indicates that the CoFe grains are favourably aligned along the (111) crystallographic plane. This arrangement could potentially result in a 3-fold magnetic anisotropy in the plane, a consequence of the inherent symmetry of the (111) orientation. The term 3-fold magnetic anisotropy indicates that the possible orientations of the spins to three specific directions within the plane. However, these expected effects might not manifest in MOKE measurements. If the sample is composed of a multitude of grains each with a random orientation, the MOKE measurement would merely present an average of all these varying orientations, potentially obscuring the expected 3-fold symmetry. The XRD analysis of our film showed the presence of Ag (111) and Ag (311) reflections, corresponding to estimated vertical grain size of approximately 5 nm and 3 nm, respectively. Our expectation is based on the idea that the Ag (311) orientation might initially have a better lattice match or alignment with the CoFe (111) surface. A good lattice match can help minimize the strain when one material is grown on another, at least initially. Once the initial layers of Ag are established, the growth may no longer be dominated by the underlying CoFe lattice structure. As the Ag film becomes thicker, its inherent preference for a lower energy state may come into play. Given that the Ag (111) orientation typically has lower surface energy than (311), the Ag might relax into this more energetically favourable state, resulting in the growth of the Ag (111) orientation.

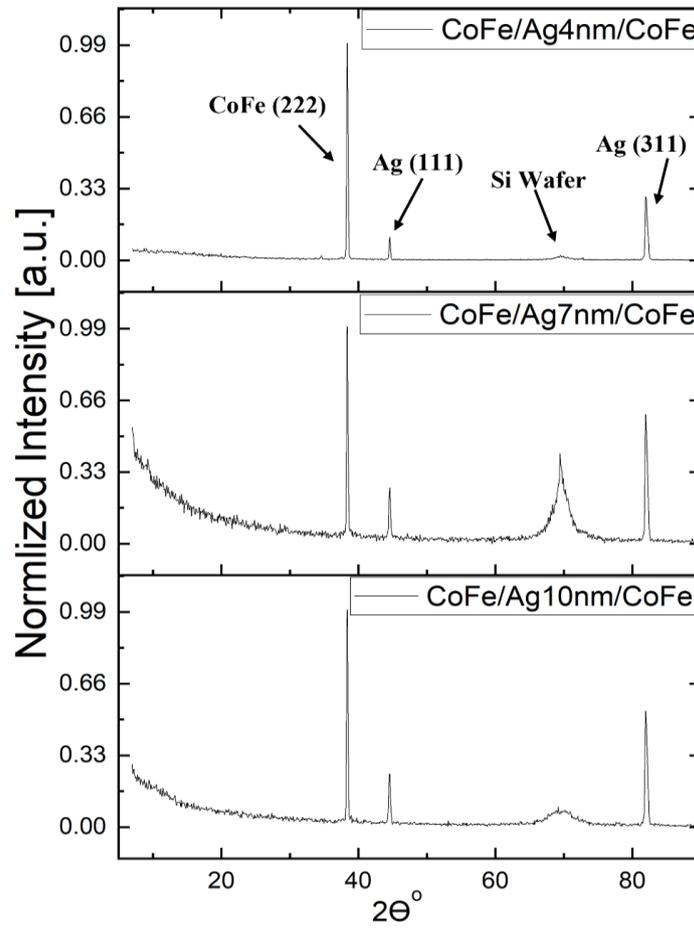**Figure 6.4**: The figure shows XRD measured for CoFe/Ag/CoFe with three Ag layer thicknesses. Only 222 peak of CoFe is observed, along with both 111 and 311 peaks of Ag at all thicknesses of Ag.
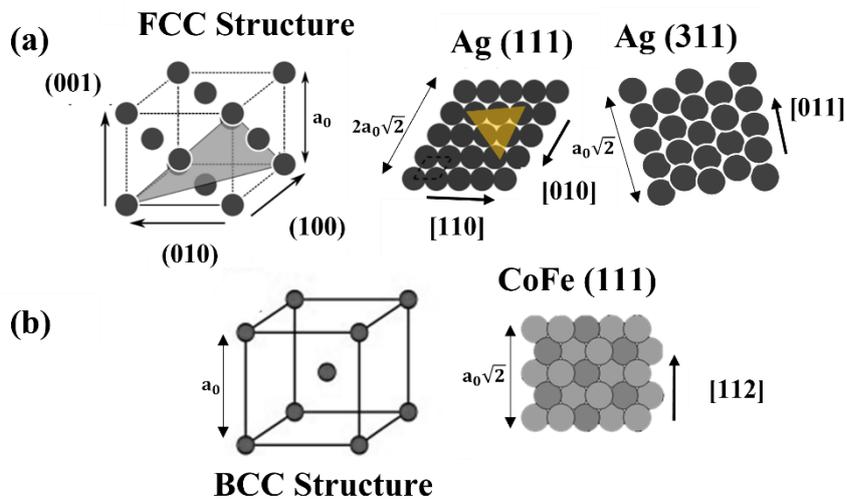

Figure 6.5: (a) The figure shows the Ag FCC structure, the (100), (010), and (001) surface planes, the top view of Ag (111) and Ag (311), (b) the top view of CoFe BCC structure and unit cell of CoFe (111).

The crystal structures and diagrams of the surfaces of the (111) surfaces of CoFe and Ag, and the (311) surface of Ag, are shown in figure 6.5. The interplanar spacing mismatch between Ag (111) and CoFe(111) is 0.070 nm while the mismatch between Ag(311) and CoFe(111) is smaller at 0.042 nm. Thus, reduced strain indicates that the lattice structures of the two interfacing materials are more compatible in that orientation, making it easier for them to align without introducing significant deformation or defects. If the grain size for one orientation were to increase as the film thickness increased, this would indicate a change in orientation after some initial thickness. However, this is not what is observed. The grain size of both Ag (111) and Ag (311) is found to be independent of the Ag layer thickness. this indicates instead that there is always a mixture of small Ag crystallites with (111) and (311) orientations. But the observations do not reflect this assumption. The grain size of both Ag (111) and Ag (311) is found to be independent of the Ag layer thickness. this indicates instead that there is always a mixture of small Ag crystallites with (111) and (311) orientations.

6.4 Magnetic properties

The magnetic characteristics of a trilayer sample with Ag thickness of 2.6 nm was analysed using a variety of methods. Three of these techniques were MOKE, FMR and PNR-PA. The magnetic properties of the Ag sample are revealed in different ways depending on the method used. For instance, the PNR-PA method can be used to obtain a depth profile of the magnetization in thin films, which is useful for probing the nanoscale magnetic structure.

The FMR approach was used to investigate the dynamic magnetization properties of the sample. As described in chapter 5, at certain Ag thicknesses anomalous enhancement of effective damping is observed, as we expect that could correlate with the weak RKKY antiferromagnetic coupling in Ag. Here we concentrate on a sample with Ag thickness of 2.6 nm, potentially exhibiting antiferromagnetic (AF) coupling due to the RKKY interaction, and it displays an unexpected increase in damping, as discussed in the preceding chapter.

6.4.1 Magneto Optic Kerr Effect (MOKE)

Illustrated in Figure 6.6 are two hysteresis loops that demonstrate the magnetic characteristics of our sample along its easy and hard axes. The main figure represents the direction in which the magnetization of our material can be switched with minimal energy or external magnetic field. Conversely, the hard axis inset the direction where a change in magnetization encounters the most resistance, requiring a higher external magnetic field for reorientation. These different behaviours are captured in the hysteresis loops, showing variations in coercivity, the strength of the magnetic field required to demagnetize the material, and saturation fields, the field strength at which all magnetic moments become aligned, preventing further increases in magnetization.
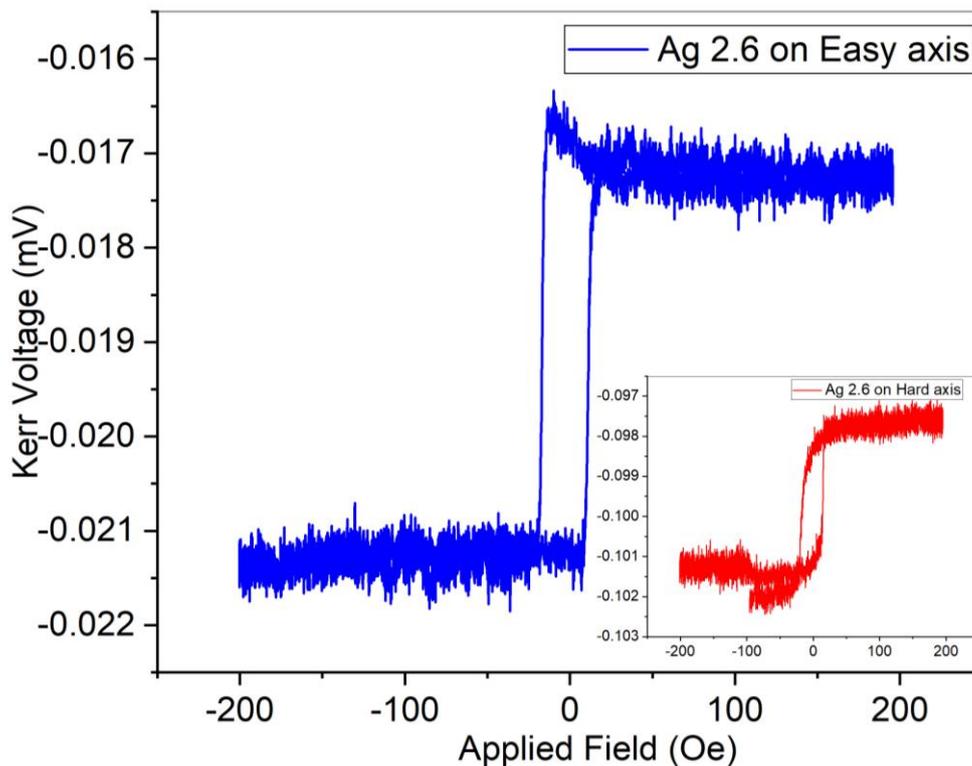
Figure 6.6: Longitudinal MOKE hysteresis loop for easy and hard axis of the CoFe/Ag 2.6 nm /CoFe sample.

When preparing for an experiment such as PNR, these hysteresis loops provide crucial information. They instruct us on how to orient the sample in the PNR device. The aim is to govern the magnetic field along the hard axis, expecting that the sample will settle into an anti-ferromagnetically aligned state along the easy axis once the field is diminished.

6.4.2 Polarised neutron reflectivity and Polarized analysis

As previously discussed in chapter 4, neutrons possess the unique ability to discern both structural and magnetic properties. Their ability to delve deep into substances provides insights into atomic and magnetic configurations. This characteristic stems from their lack of charge, enabling them to interact directly with atomic nuclei and magnetic moments instead of electron clouds, thus offering distinct understanding of atomic structures and magnetism. An in-depth explanation of this method is detailed in Chapter 4. PNR measurements were carried out at the PolRef beamline located at the ISIS neutron source.

In the PNR/PNR-PA measurement setup, a key consideration is the alignment of the magnetic field along the hard axis of the sample. We relax the magnetization from hard-axis saturation, and we might naively expect the layers to tend to align antiparallel to one another, along/against the beam direction as the field is reduced. PNR-PA will detect whether this is the case. The strength of the field applied in the PNR measurement exceeds the saturation field - the least external magnetic field strength needed to completely magnetize the sample. The value of the saturation field is predetermined through MOKE measurements, as shown in figure 6.6. By conducting the PNR measurement with a field strength surpassing the saturation field, we ensure that the sample remains fully magnetized and stable throughout the experiment. This setup enables us to obtain baseline data regarding the structural and magnetic depth profiles of the sample, which can then be used for more reliable fitting of the more complex PNR-PA data. For this specific experiment, the PNR-PA was taken at two different angles where the sample is rotated about the film normal axis. As in other x-ray analysis in fig 6.3, the sample was measured with the scattering plane along the easy axis of the sample and rotated 45 degrees.
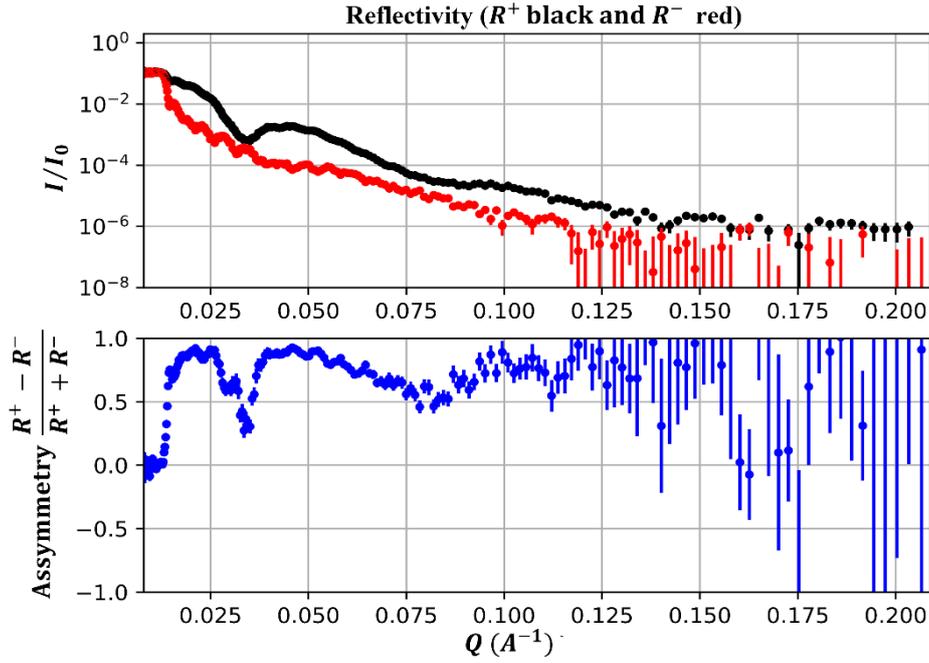
Figure 6.7: The experimental results of PNR for the Ag(2.6nm) sample. The upper frame represents the data, while the lower frame illustrates the asymmetry profile.

A full PNR measurement at saturation is shown in fig 6.7, this is over an extended Q range, but the signal falls to background at higher Q. Due to the extended counting times required for PNR-PA those measurements are only taken to $Q_z \sim 0.1 \text{Å}^{-1}$, and so for consistency fits to the PNR data are made only over this range, shown in figure 6.8. The data shown in both figures 6.7 and 6.8, one can observe a distinct separation between the red and black curves. This indicates the sample has a net magnetization along the field direction. The lower frame of fig 6.7, this shows spin-asymmetry, which is derived from the reflectivity, and highlights the magnetic contribution to the scattering.

Data from the PNR measurement at saturation with a maximum field of 0.7 T applied through the electromagnet, applying a field to the sample, and fitted using the Refl1D software. The best fits are shown in figure 6.8. In the simulated model, the layers of the test sample were sectioned into N divisions, with each division having a SLD. Parameters like thickness, density, interface roughness, and magnetic moment were modulated using Parratt's recursion algorithm to achieve the lowest chi-square (χ^2) value. The optimal number of divisions (N) was identified based on the best model fit and the minimum χ^2 value, in this specific case, N=4 for the trilayer. Any increase in N beyond 4 did not produce a substantial decrease in the χ^2 value, indicating the optimal N was indeed 4 layers. Unique characteristics of the system were identified, including SLD variations near the interface. Given that the SLD, dependent on the depth

perpendicular to the sample surface, incorporates both nuclear and magnetic aspects, it was possible to draw both structural and magnetic depth profiles of the entire system. Consequently, the best fit simulation produced a detailed cross-sectional depth profile of the complete system, depicted in Figure 6.8.

The χ^2 minimization values, which serve as an indicator of the quality of the fit, are displayed in the reflectivity diagrams as shown in Figure 6.8. When the χ^2 value was around 3.8, it signifies a good PNR fit [121]. The theoretical model used presupposes an ideal interface would be completely flat/smooth that is characterized by an error function, but this may not always be an accurate representation.

The SLD results derived from PNR fitting, figure 6.8 b, show a difference in interface width between CoFe/Ag and Ag/CoFe interfaces. There is a difference in the structural scattering length density between the CoFe layers, but the magnetic SLD is very similar between the two layers. From the PNR-PA data fitting, the magnetism of the FM layers was found to be roughly equal, both approximating a magnitude of 1.4 x 10^3 Gauss. The similar magnetization in the two FM layers agrees well with the results of FMR, which was 1.3 x 10^3 Gauss for the same sample, where they are not able to be distinguished, which are detailed in Chapter 5, confirms a coherent narrative regarding the magnetic properties of the system, despite the asymmetry observed in the broader scattering length density. The neutron scattering factors exhibit greater variance compared to x-rays. Consequently, the similarity in PNR SLDs between the top and bottom layers implies highly comparable compositions. This is because even minor compositional changes can result in significant differences due to the pronounced variation in neutron scattering factors.
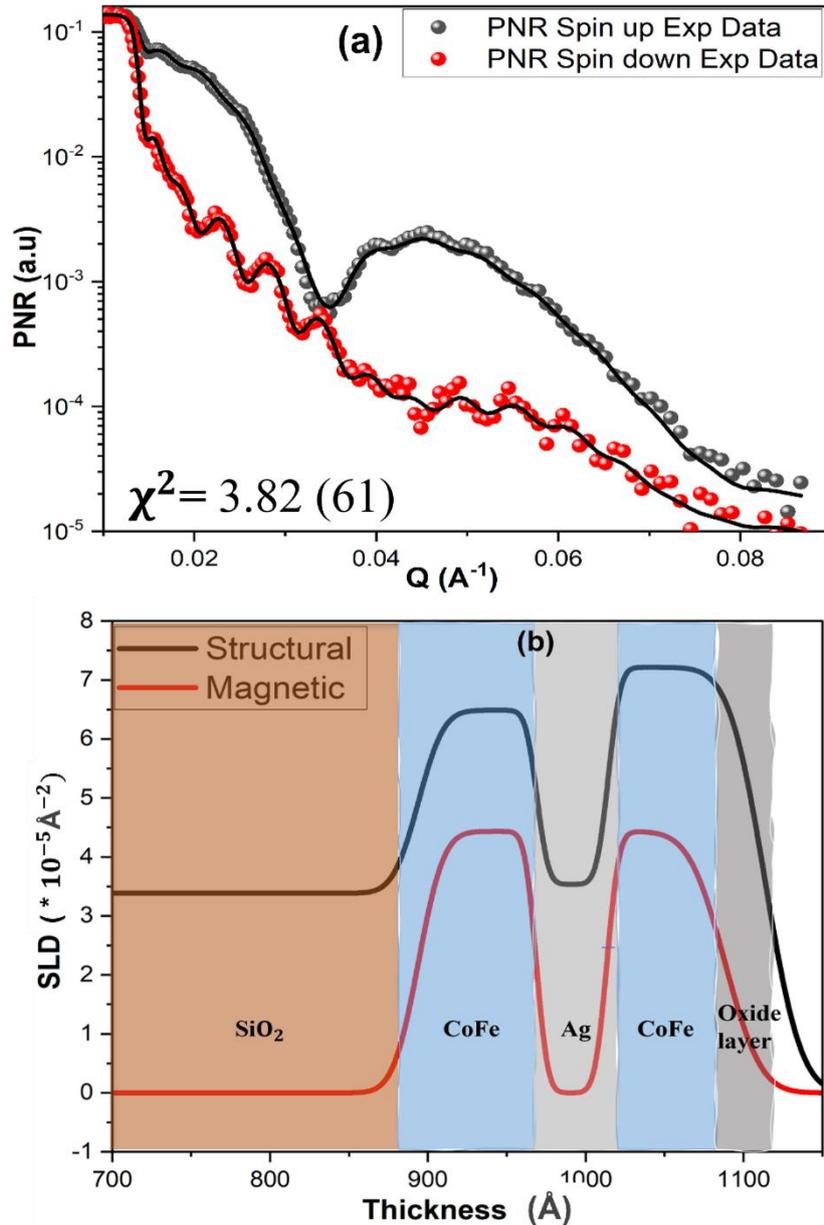
Figure 6.8:(a) show the best fit of the PNR data and (b) extracted structural scattering length density from the best simulation of PNR measurement for CoFe/Ag 2.6 nm /CoFe trilayered samples (as labelled) grown on Si/SiO2 substrate using Refl1D simulation.

6.4.2.1 Polarized analysis

PNR-PA plots display non-spin-flip and spin-flip reflectivity curves, showing structural and magnetic properties of the investigation sample. Spin-flip channels in PNR-PA are essentially detectors for changes in neutron spin orientation caused by interactions with the material's magnetic properties. They show the material's magnetization components' presence and orientation along the neutron beam, more details for the spin states in PNR-PA have been

discussed in Chapter 4. Following the PNR measurement, the PA results are depicted in figure 6.9. Correspondingly, the associated asymmetry profiles for each measurement are displayed at the bottom. All measurements show a higher number of fringes in the 0.025 Å⁻¹ to 0.09 Å⁻¹ range for spin-down data. On the other hand, for the spin up-up range, only a single fringe is visible within the 0.03 Å⁻¹ to 0.04 Å⁻¹ interval. However, it is critical to acknowledge that the PA measurements under saturated conditions the non-spin-flip reflectivity is clear, but the spin-flip reflectivity is all within the noise as demonstrated by the large error-bars. Also, there is essentially no spin-flip reflectivity because the sample is saturated along the field direction, and no magnetic component exists along the beam. The positions and/or depths of the Kiessig fringes, interference patterns seen in x-ray and neutron reflectivity measurements, remain unchanged as the applied magnetic field varies. The asymmetry does not change much, and the relative intensities of the non-spin-flip channels do not change. The magnetization may rotate away from the field direction as the field is reduced, but each layer relaxes to a similar angle from the field; the component of M for each layer along the field direction are similar, so the asymmetry changes little. Figure 6.9 a and b, show the difference between the saturation field 0.7 T and the low field 1.4 mT. The spin-flip signals increase, they are no-longer in the background as the error-bars are now not dominant. This means that there is a component of magnetisation in the sample along the beam direction. In Figure 6.9 c, as rotating the sample by 45 degrees with the low-field condition, the asymmetry remains relatively unchanged.
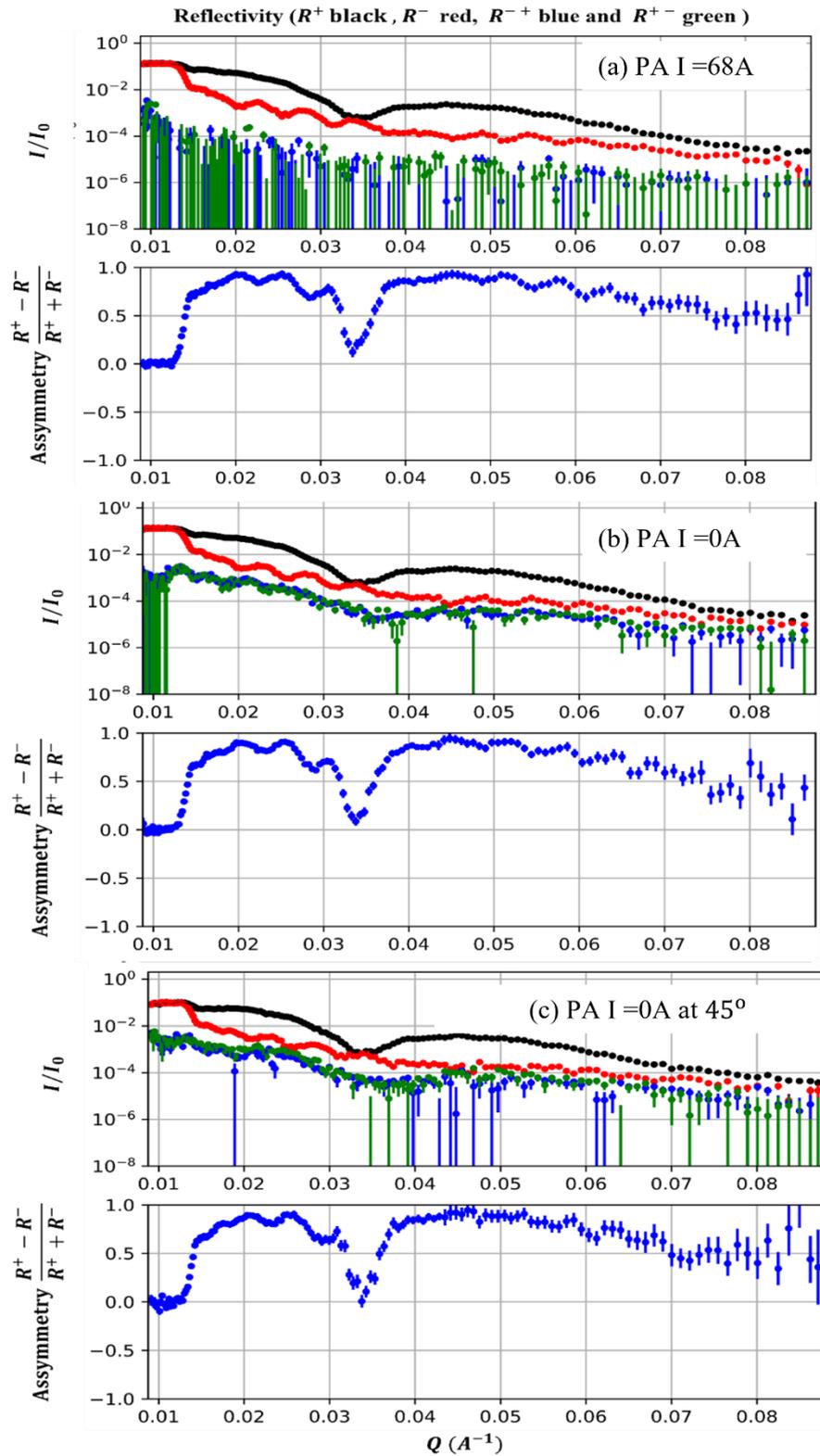
Figure 6.9: illustrates the PA data for samples deposited under varying field conditions. The figure showcases the asymmetry profiles measured at distinct field levels, spanning a magnetic field range from a low of 1.4 mT to a maximum of 0.7 T.

The PNR-PA data along with the best fit models are shown in figure 6.10. The χ^2 values stand at approximately 4.3 for the 0 degrees measurement and lower at 3.6 for the 45 degrees measurement. These figures indicate a successfully performed PNR-PA procedure, with lower χ^2 values suggesting a better fit between the model and the experimental data.
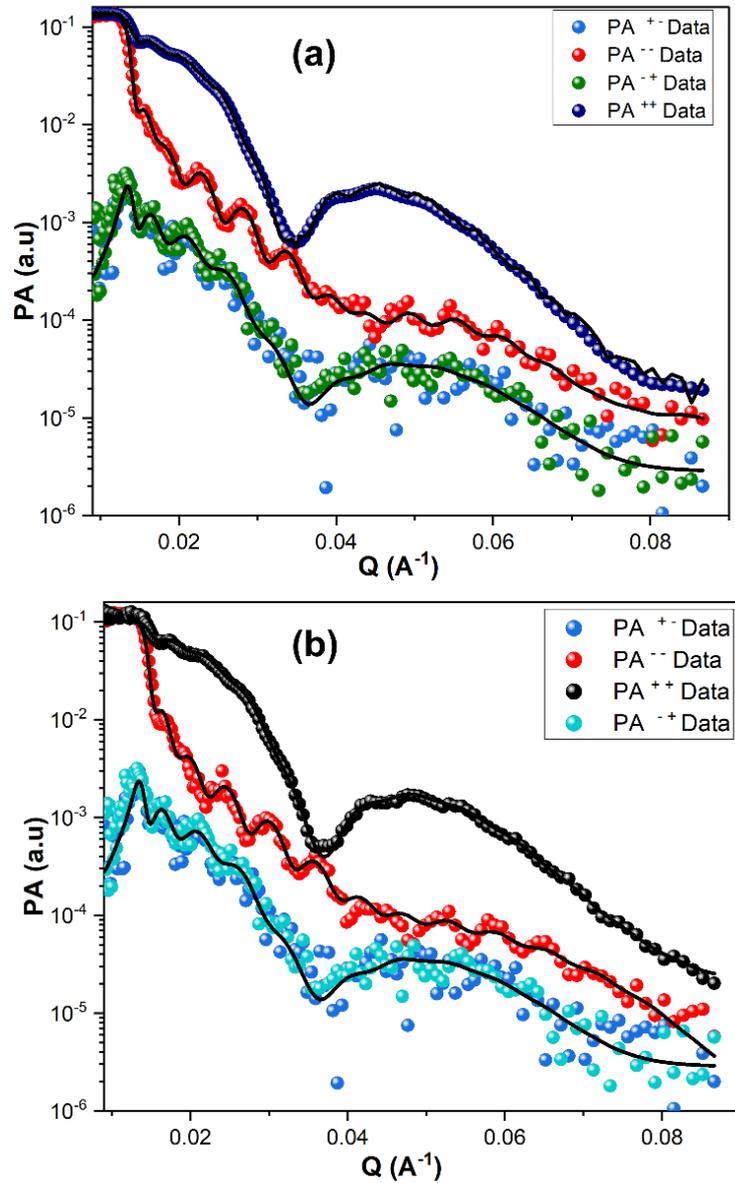
Figure 6.10: The PNR-PA data and the best fit of (a) PNR-PA with the sample oriented with the hard axis aligned with the applied field and (b) PNR-PA with the sample aligned with the hard-axis rotated 45 degrees from the applied field.

As for the XRR measurements discussed in section 6.3.1, we again rotated the sample by 45 degrees about the sample normal, such that the scattering plane is along the sample diagonal. By rotating the sample, the easy axis the rotate relative to the field, and so the magnetizations may point in a different direction at the same low field. From the PA fitting, the magnetization orientation θ_M for the unrotated orientation, as shown in table 6.3, was found to be 265 degrees for the lower layer and 252 degrees for the upper layer. It is important to note that the guide-field direction corresponds to 270 degrees in the fits and the neutron beam propagation to zero degrees. This reveals that the magnetizations of both layers are not aligned perfectly with the external magnetic field; they are rotated by about 5 and 18 degrees, respectively, from the field direction. This misalignment is indicative of the presence of magnetic anisotropies in the layers, which compel the magnetization to deviate from the applied field direction. The angle of this variation arises from an energy minimization process, reflecting the interplay between the anisotropy and Zeeman energy. When the sample was rotated by 45 degrees, the magnetization orientation changed to 250 degrees for the lower layer and 240 degrees for the upper layer, an example shown in fig 6.11. The relative change in magnetization orientations between the layers demonstrates that the magnetisation in the two ferromagnetic layers is modified differently by rotation of the sample in the applied field. This rotation led to a narrowing of the difference in magnetization orientations between the two layers, from 13 degrees to 10 degrees. The consistency in non-spin-flip intensities and spin asymmetry between 0- and 45-degree data. the small difference in angle between the magnetization of the two layers. These subtle differences require detailed data analysis in order to extract the possibly small changes in magnetization orientation. Measurements at further angles and field-strengths will enable quantitative determination of the anisotropy and coupling constants, which will be the subject of future work.
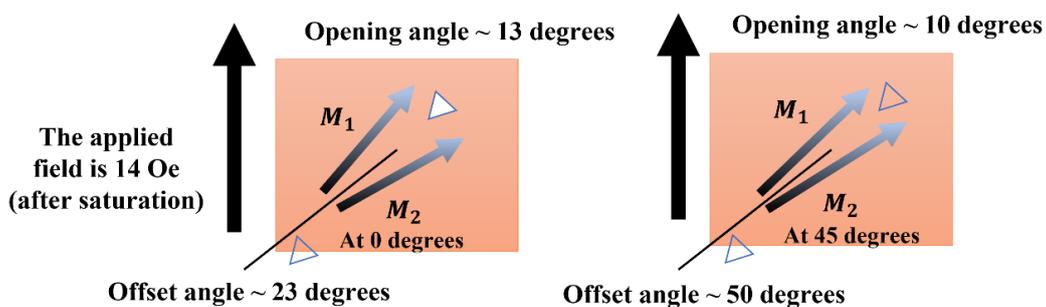

Figure 6.11: A diagram illustrating the directions of magnetization for the two rotation states present at low field 1.4 mT at 0 and 45 degrees.

Angle between nominal hard-axis and guide field	$\theta^{o}_{M\ upper}$	$\theta^{o}_{M\ lower}$
At 0°	252 ± 1	265 ± 2
At 45°	250 ± 1	240 ± 1

Table 6.3: Extracted layer the magnetization orientation obtained from PA models along different in-plane directions for a CoF/Ag (2.6 nm)/CoFe sample. Each simulated parameter in both the 0-degree and 45-degree measurements is accompanied by an associated error.

The difference in θ_M between the upper and lower layers, both at 0 and 45 degrees of sample rotation, signifies that the upper layer has its own magnetic anisotropy. This anisotropy could influence the lower by the RKKY interaction through the Ag layer. The RKKY interaction results from oscillations in the conduction electrons' spin polarization, which extends over the Ag spacer. As these oscillations traverse the spacer, they can alter the magnetic coupling preference in the upper layer [122]. This change in coupling can effectively rotate the anisotropy direction of the upper layer, causing a misalignment with the lower layer's intrinsic anisotropy. This could be attributed to differences in the strength or direction of the anisotropy in each layer. The observed behaviours suggest that the layers respond differently to external magnetic fields, and their magnetization orientations are not simply dictated by the applied field.

The structure of the interfaces is important as this impacts on the spin-mixing conductance; for spin-pumping in tri-layer structures to not cancel out, the two interfaces need to be different in some way and the PNR suggests this is the case. So, spin-pumping could play a role in the damping enhancement. Earlier XRR measurements suggested that this system is predominantly composed of CoFe, with a lower presence of Ag. This variation in composition has been noted in other studies, and it could potentially be explained by the differing surface energies of the elements in CoFe [104, 114]. When the angle is changed, no changes should be detected in the structural SLD. The SLD variations and the changes in θ_M for each layer under different conditions provides key insights into the anisotropic magnetic nature of these layers. This is typical in magnetic thin films due to shape anisotropy and can also be influenced by factors like interlayer coupling and the magneto crystalline anisotropy of the material.

Summary

This chapter investigated the structural and magnetic SLD variations in a CoFe/Ag/CoFe system using best fit models to measurements of polarised neutron reflectometry with polarisation analysis. Findings revealed a decrease in structural SLD at the Ag/CoFe interface and an increase in magnetic SLD during a 45-degree scan, possibly due to compositional variation and anisotropic magnetic properties. An insignificant drop in the Ag layer's thickness was also seen. The PA measurements reveal the relaxation behaviours of magnetic layers through spin-flip reflectivity curves. The magnetization in each layer typically aligns in a specific in-plane direction, which changes upon rotating the sample. This phenomenon could be recognized to the anisotropic nature of magnetic properties and might influenced by factors like interlayer coupling and magneto-crystalline anisotropy. From our FMR analysis, the resonance field change in FMR spectra could be linked to factors such as anisotropy. In materials with pronounced magneto-crystalline anisotropy, we expect the resonance fields to be sensitive to the orientation of the applied field relative to the easy or hard axes of the material. Such shifts provide insights into the magneto-crystalline anisotropy constants. Changes in magneto-crystalline anisotropy can offer explanations for unusual linewidths behaviours. We are utilizing this rationale to explain the anomalous linewidth enhancement observed at mid-range frequencies from FMR in tri-layers with an Ag spacer thickness that might align with an RKKY coupling peak. Such shifts might lead to multiple resonances in close proximity, making them hard to separate. Alternatively, they could cause spin-pumping due to asynchronous magnetization precessions. In essence, variations in the magneto-crystalline anisotropy might be linked to the bump that we observed in the anomalous linewidth. Further insights into the behaviour of the two ferromagnetic layers forming on the substrate will be presented in Chapter 7.

Chapter 7: The Effect of The Magnetic Anisotropy in FM/Ag/FM Sample

7.1 Introduction

In this chapter, we have investigated the magnetic anisotropy present in our FM/Ag(2.6nm)/FM sample, we are studying a sample that is nominally antiferromagnetically (AF) coupled. This is motivated by the PNR-PA measurements described in the previous chapter. We have started by providing an overview of magnetic anisotropy, emphasizing its role in determining a material's magnetic properties. Next, the background used to explore the magnetic anisotropy in FM/NM/FM and NM/FM samples, including a description of how the sample was prepared. After describing details of the approach used to prepare samples with well-defined magnetic anisotropy, we have shown the result of the angular measurements using MOKE and FMR methods. We then discussed results obtained from the MOKE and FMR measurements, interpreting the complex interplay of factors that influence magnetic anisotropy and how it is displayed in the behaviour of our sample. This chapter demonstrates the significant role that magnetic anisotropy plays in determining the dynamic magnetisation behaviour.

7.2 Background

From a fundamental perspective, ferromagnetism relies on magnetic anisotropy, which creates preferred orientations for the magnetization of a material. If the anisotropy energy is less than the thermal energy, the material becomes superparamagnetic. In this state, the material's magnetic moments are aligned at a microscopic level but without a stable magnetisation direction [11]. It has been observed experimentally that ferromagnetic single crystals have easy and hard magnetization orientations, where the amount of energy needed to magnetise the crystal changes depending on the orientation of the applied field with respect to the crystal axes. For technological applications, magnetic anisotropy is a crucial characteristic of magnetic materials. Permanent magnets, data storage media, transformer cores, and magnetic recording heads all require materials with varying degrees of magnetic anisotropy [123].

Magnetic anisotropy can be generated from two basic sources: magnetic dipolar interaction and spin orbit interaction [123]. The dipolar interaction, because of its long-range nature, typically results in a contribution to the anisotropy, the amount of which is shape

specific. In thin films, it plays a crucial role and is largely responsible for the in-plane magnetization that is typically seen. Total electron-spin system energy is agnostic to magnetization direction when no spin-orbit or dipolar interaction is present. The spins in a localised picture are connected to the orbits, which are affected by the crystal lattice via the spin-orbit interaction. The total, spin plus orbital, magnetic moment in itinerant materials is coupled to the crystal axes via a tiny orbital momentum induced by the spin-orbit interaction. As a result, the total energy reflects the symmetry of the crystal and changes depending on the orientation of the magnetization with respect to the crystalline axes. This is the magneto-crystalline anisotropy, introduced in this chapter. Reduced symmetry at an interface drastically alters this contribution relative to the bulk, resulting in what is known as interface anisotropy, also noted in [124]. In multilayers, where the lattice mismatch between adjacent layers causes magnetostriction due to magneto-elastic anisotropy, the spin-orbit interaction, along with the overlap in wavefunctions between neighbouring atoms, is responsible for the induced anisotropy [11].

Within a bilayer structure composed of a FM and some other material, the principal dictators of magnetic anisotropy and its resulting influences are the exchanges occurring between these layers. The processes known as exchange bias and interfacial anisotropy are clear examples of these interactions. With the exchange Bias, when the FM layer is in close adjacency to the antiferromagnetic layer, an interplay between the spins in each layer transpires. This may give rise to the anisotropy in the FM layer, this is termed exchange bias. This bias can induce a change in the magnetic hysteresis loop of the FM layer along the field axis, generating a bias field. This mechanism is widely employed in magnetic storage devices, serving to stabilize the magnetization trajectory of a reference layer [125].

Altering focus to interfacial anisotropy, this form of anisotropy springs from a symmetry disruption at the juncture of the FM and NM layers. The presence of spin-orbit interaction at this interface, coupled with broken translational symmetry, brings about a contribution to the magnetic anisotropy that could markedly deviate from the anisotropy of the bulk material or the FM thin-film without adjacent NM layer. The manifestation of these phenomena is primarily reliant on a range of factors such as layer thickness, quality of interface, and the fabrication techniques employed. For example, the extent of interfacial anisotropy could be influenced by elements like the roughness at the interface, interdiffusion, or strain present at the interface. The spin-orbit interaction at an interface, which couples the spin of an electron with its orbital angular momentum, is leading to pronounced anisotropic behaviour at

the interface. Exchange interactions at the interface further contribute to either ferromagnetic or antiferromagnetic coupling between adjacent magnetic layers, which is highly sensitive to the properties of the non-magnetic spacer layer. The origins of interface anisotropy have significant effects for the magnetic properties shown by thin films. The ability to maintain the stability of magnetization in a given direction via interface anisotropy is an important factor in the performance of magnetic memory devices and spintronic applications. Furthermore, the existence of anisotropy has significant consequences on the formation and stability of magnetic domains in thin films, as well as on the energy barrier that controls magnetic switching [126]. This property holds important value in several technological applications.

As an example of recent studies into interfacial magnetic anisotropy was investigated the relationship between the texture of Pt films grown at various thicknesses over Ta substrates. It was discovered that a minimum thickness of 3 nm for Pt was required to achieve a polycrystalline Pt film with a preferred crystallographic orientation along the (111) plane. The presence of this Pt texture was found to be closely linked to the magnetic properties of a subsequently deposited $Co_{20}Fe_{60}B_{20}$ film. Specifically, when the Pt film exhibited a (111) texture, the single layer CoFeB structure displayed strong perpendicular magnetic anisotropy, characterized by a high remanent to saturation magnetization ratio of up to 0.76. Notably, this study demonstrated that by sandwiching the CoFeB layer, with a specific composition of 20:60:20 (%), between two layers of Pt, strong perpendicular magnetic anisotropy (PMA) behaviour could be achieved. In contrast, when CoFeB was grown with Ta on the opposite interface, a complete loss of PMA was observed, accompanied by a significant decrease in saturation magnetization. The optimal thickness for the CoFeB layer in single ferromagnetic layer structures (Ta/Pt/CoFeB/Pt) was determined to be around 0.8 nm, exhibiting an anisotropy energy comparable to previous reports on Ta/CoFeB/MgO systems and significantly larger than that of Au/CoFeB/Au systems. The study also involved the deposition of multi-layer structures consisting of four CoFeB layers separated by Pt buffers. Analysis of the magnetic hysteresis loops revealed that thinner Pt buffers (1 nm) led to a complete loss of perpendicular magnetic anisotropy, whereas thicker Pt buffers exhibited favourable PMA behaviour with lower nucleation fields. The adjacent CoFeB layers in these structures showed ferromagnetic dipolar coupling with parallel alignment in the out-of-plane direction [127].

Moreover, the magnetic anisotropy in FM/NM/FM trilayer structures is influenced by the oscillatory coupling behaviour resulting from interlayer exchange coupling between the FM layers. This coupling behaviour varies with the thickness of the NM layer. By carefully

tuning the layer thicknesses and selecting appropriate materials, it becomes possible to finely control and customize the magnetic properties of these tri-layer structures to meet the specific demands of various applications [128]. In systems exhibiting antiferromagnetic (AF) coupling, a few key behaviors can manifest. When there's a pronounced AF coupling, antiferromagnetic alignment is typically achieved, making the system susceptible to events like spin-flop, especially if the coupling is exceedingly strong. However, as this coupling's strength diminishes, particularly in relation to the magnetic anisotropy of the system, the dynamics shift. The anisotropy, which represents the material's inherent tendency to magnetize in a specific direction, can dominate [129, 130]. As a result, even if there's some level of AF coupling present, the magnetic layers might prefer to remain in a parallel orientation because the weakened AF coupling can't counteract the strong directional preference imposed by the anisotropy. These investigations have provided valuable insights into the magnetic behaviour of FM/NM/FM systems, contributing to advancements in the field of magnetism and magnetic materials.

Another study has reported unusual magnetic anisotropy and it was observed in NiFe/Cu/Co trilayers deposited using magnetron sputtering on a Cu (5 nm)/Si (111) substrate with a 4° tilt-cut. The easy axis of the NiFe layer was aligned to be orthogonal to that of the Co layer. Interestingly, by introducing a small amount of Co into the NiFe layer, a parallel alignment of the easy axes of the two magnetic components could be achieved. The NiFe/Cu/Co trilayers exhibited magnetoresistance (MR) characteristics suitable for switching devices, with negligible hysteresis. Furthermore, in the case of NiFeCo/Cu/Co trilayers [11], the observed high spin-polarization and stable magnetic properties under varying temperature conditions are noteworthy, indicating the high potential of these structures for magneto-resistive memory devices.

Another study focused on magnetic anisotropy in trilayer systems found that observing a notable emergence of uniaxial anisotropy in a sandwich structure consisting of Co (0.8 nm)/Cu (1.5 nm)/Co (0.8 nm) as the temperature was reduced from 300 K to 50 K. A comprehensive analysis of the various contributions to the anisotropy revealed the challenges in distinguishing between the bulk and interface effects due to the thin Co layers and strong intermixing occurring at the Co/Cu interfaces [131]. However, the interface contribution appeared to be more suitable in explaining the observed behaviour. In multilayer magnetic structures, the interfaces between layers play a critical role in determining the system's magnetic behaviour. The magnetic exchange coupling across the non-magnetic spacer is highly

sensitive to interface properties and can lead to either ferromagnetic or antiferromagnetic coupling between magnetic layers. Additionally, interface anisotropy, arising from the broken symmetry and differing atomic environments at the surface, can dominate over bulk anisotropy in thin films, stabilizing magnetization in a specific direction. The quality of these interfaces, including factors such as roughness can further modulate these effects. Notably, the temperature dependence of these interface properties can differ from that of bulk properties, contributing to distinct temperature-dependent magnetic behaviours. Additionally, the study revealed that the strong perpendicular anisotropy observed at low temperatures could be attributed to the evolution of the intermixed interfaces with changes in temperature. These findings provide valuable insights into the intricate interplay among interface effects, intermixing, and temperature, elucidating their role in determining the magnetic properties, particularly the anisotropy, in thin film structures.

In Ni/Ag/Ni trilayer structures [132] the magnetic anisotropy has been investigated and show that the presence of Ag layer between the two Ni layers was found to have a significant impact on the magnetic properties of the trilayer system. Specifically, it was observed that the introduction of the Ag layer resulted in an enhancement of perpendicular magnetic anisotropy in the Ni layers. The strength of the PMA was found to increase as the thickness of the Ag layer increased. The study further revealed that the improved PMA in the Ni/Ag/Ni trilayer structure was attributed to the interfacial coupling between the Ag layer and the Ni layers. The Ag layer acted as a mediator, influencing the magnetic exchange interactions at the interfaces, and promoting the PMA effect. These findings hold great potential for the utilization of pulsed electrodeposited Ni/Ag/Ni trilayers in various magnetic applications, particularly in magnetic storage and spintronics. The study provides valuable insights into the complex relationship between different layers in trilayer structures and their impact on magnetic anisotropy.

Another investigation into magnetic anisotropy revealed the magnetic properties of Fe (001) thin films grown on GaAs (001) substrates which were systematically explored, focusing on the in-plane magnetic anisotropy [13]. These analyses were performed using FMR spectroscopy. The Fe thin films were fabricated using two distinct methods: magnetron sputtering and Molecular Beam Epitaxy (MBE). Studying the angle-dependent resonance fields revealed a characteristic four-fold in-plane magnetic anisotropy, which aligns with expectations for a cubic lattice structure inherent to Fe. The uniaxial magnetic anisotropy (UMA), which was identified in Fe thin films fabricated by MBE, was absent in the samples produced via magnetron sputtering. Furthermore, X-ray diffraction study of a series of epitaxial

of similar sample clearly rules out magnetoelectric coupling (ME) as well as shape anisotropy as the origin of the observed UMA in the thinnest films [133]. The investigation leads to a conclusion that the UMA in FeGaAs (001) is caused by an interface anisotropy. On the other hand, the evolution of the magnetic anisotropy as a function of Fe deposited thickness is very well described as a result of competition between magnetoelastic coupling and interface UMA.

In $Co_{70}Fe_{30}$ films, the study indicates that applying a magnetic field during the epitaxial growth of bcc-CoFe on GaAs (001) substrates can lead to a substantial enhancement of the film's uniaxial magnetic anisotropy [134]. Interestingly, this enhancement occurs when the applied field is aligned with the interface-induced uniaxial hard axis, which is contrary to what might be intuitively expected. When the deposition field is applied along the interfacial uniaxial easy axis, there is an increase in the component of the ratio between the atomic species-resolved orbital and spin magnetic moments that are directed along the uniaxial easy axis of magnetization. When the deposition field is applied along the interfacial uniaxial hard axis, this component decreases. The study focuses on how the deposition conditions might affect the magnetic properties of epitaxially formed CoFe films, which can be complex. In the investigation of amorphous CoFeB and CoFe thin films, the study revealed that an in-plane UMA can be induced because of the interface interaction [135]. The observed characteristics of this UMA align specifically with those of bond-orientational anisotropy. This finding suggests that such a microstructural mechanism, related to the orientations of local bonds in the material, may also be the pathway through which in-plane UMAs are generated in FM amorphous alloy films that are deposited in the presence of a magnetic field.

In the field of magnetism and spintronics, the alloy systems CoFe and NiFe share both similarities and differences in their structural, electronic, and magnetic attributes. These alloys often adopt crystalline structures, NiFe is (FCC) crystal structure, while CoFe can exhibit either BCC (Fe rich) or FCC (Co rich). Electron motion and spin polarisation are facilitated by the metallic behaviour they exhibit, which can be identified by partially occupied d orbitals. At room temperature, these alloys show ferromagnetic behaviour and possess a high saturation magnetization, causing them advantageous for a multitude of magnetic applications. However, CoFe usually possessing a higher saturation magnetization due to the greater number of unpaired electrons in Co d orbitals. The alloys' different electronic configurations and bonding properties significantly impact their apparent band structures, density of states, and magnetic properties [22,23].

7.3 Experimental Details

In Chapter 3, we explained the processes of sample preparation and magnetron deposition. The films were deposited on a SiO_2 substrate, the resulting structure being $Si/SiO_2/FM/Ag$ (2.6nm) nm/FM. Each FM layer had a thickness of 10 nm while the NM layer was 2.6 nm thick. The central point of exploration in this chapter was the impact of magnetic anisotropy on the NiFe/Ag2.6 nm/NiFe sample, this is the structure with AF alignment across the Ag spacer layer, as used for PNR-PA studies in chapter 6. The significant difference in the growth of this sample hinges on the orientation of the sample stage within the sputtering apparatus. Contrasting with the samples discussed in Chapter 3 where the sample stage was consistently rotated during the growth of all layers, the sample stage remained static during the formation of the first FM layer in the sample we are focusing on in this chapter. The Ag layer was formed in the usual way with the sample stage rotating throughout its growth process. Lastly, the second FM layer's growth was the same as the first layer, but with the sample stage being rotated 90 degrees from its initial position, this is depicted in figure 7.1. The reason for this is to induce orthogonal magnetic easy axes in the two FM layers, to determine the impact of these anisotropies on the dynamic behaviour of the trilayer structure.
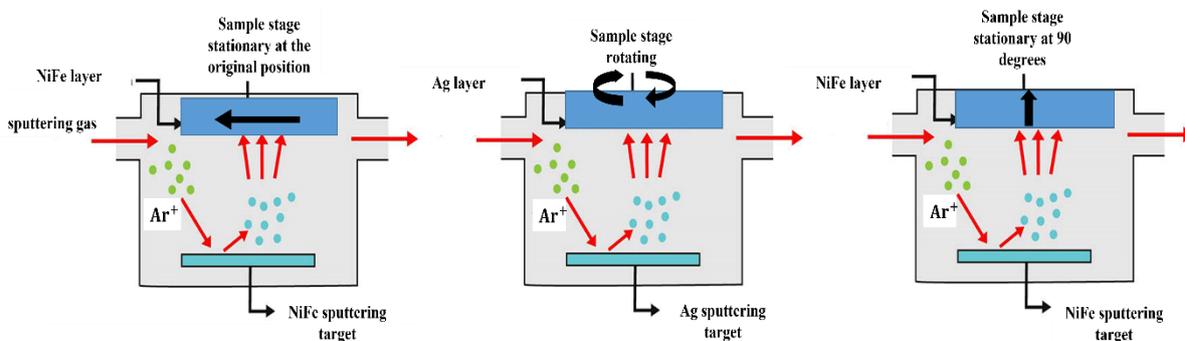

Figure 7.1. The steps for growing the multi-layer thin film of NiFe/Ag/NiFe via Ultra-High Vacuum (UHV) are illustrated, where the positioning of the sample stage was controlled throughout the entire growth process.

In this experiment, we opted for $Ni_{80}Fe_{20}$ as the FM layer, replacing the previously used $Co_{80}Fe_{20}$. The change of our FM layer, from CoFe to NiFe, is not anticipated to materially affect our findings, because the spin-current transport effects depend only on the Ag layer, which should not differ significantly, and AF coupling also depends on the Ag layer only. NiFe is an effective selection here as it is well known to be able to support a uniaxial magnetic anisotropy engineered [136].

7.4 Magnetic properties

Angular measurements with both MOKE and FMR techniques offers significant advantages. These angular measurements are crucial for MOKE because they reveal the direction of magnetization in the sample. In this study, we aim to investigate the complex interaction between varying anisotropy in FM layers and the resultant resonance properties of a trilayer structure with weak AF coupling. Building on the established capability of materials such as NiFe to support engineered uniaxial magnetic anisotropy, we pose the question of whether such a trilayer configuration can manifest a unique resonance signature specifically, a pair of close-but-slightly-different resonances that can be detected by FMR as a double resonance. Furthermore, we seek to discern if, under certain conditions, these resonances can present as a single resonance but with an augmented apparent linewidth over a given frequency range. This investigation not only refer to a fundamental study in the field of spintronics, but it also holds an opportunity to advance our understanding of FMR as an effective method for describing complex magnetic structures.

7.4.1 Angular Magneto Optic Kerr Effect (AMOKE)

The variations seen in the MOKE measurements at differing angles can be recognized as the material's intrinsic magnetic anisotropy. We define the measurement at zero degrees as that where the applied magnetic field coincided with the magnetization's easy axis the direction wherein alignment of the material's magnetic moments is most simple. This orientation results in a wider hysteresis loop, due to an increase in coercivity, the intensity of the magnetic field required to render the material demagnetized, associated with this alignment.

Figure 7.2 shows the MOKE hysteresis loops for the trilayer at various angles relative to the reference edge of the wafer. In this measurement, we expect apparent magnetic anisotropy behaviour between two ferromagnetic layers in a trilayer system. Specifically, the first layer is expected to show an easy axis of magnetization oriented at 0 degrees and a hard axis at 90 degrees. In contrast, the second layer is expected to have its easy axis at 90 degrees and its hard axis at 0 degrees. We assumed that the signals corresponding to these two layers appear superimposed. This superimposition is a result of MOKE's sensitivity to the magnetization within the entire depth of the sample, it appears to be slightly more to the upper layer due to the penetration depth. It is expected that the angles of 60 and 30 degrees would represent an intermediate axis. However, observations indicate an apparent hard-axis-like

behaviour at an angle approximately 50 degrees, which lies between the measurement taken at 30 and 60 degrees and is closer to 60 degrees since this appears more like a hard-axis. This angle reflects a single-layer hard axis, and rotating away from this in either direction becomes like a single layer easy axis.

We have calculated the penetration depth for NiFe at a wavelength of 658 nm to be approximately 26 nm. This means that light can penetrate the material to a depth of roughly 26 nm before its intensity notably decreases. However, it is important to note that this doesn't imply uniform intensity throughout the entire 10 nm thickness of the NiFe layer. As for the magnitude of the MOKE signal, if the change in magnetization (ΔM) of the NiFe is 9750 G, and the penetration depth (δ) is 26 nm, the estimated magnitude of the MOKE signal for the NiFe film is approximately 38 degrees. These values serve as rough estimates and may vary based on the actual material properties and experimental conditions [9,22].
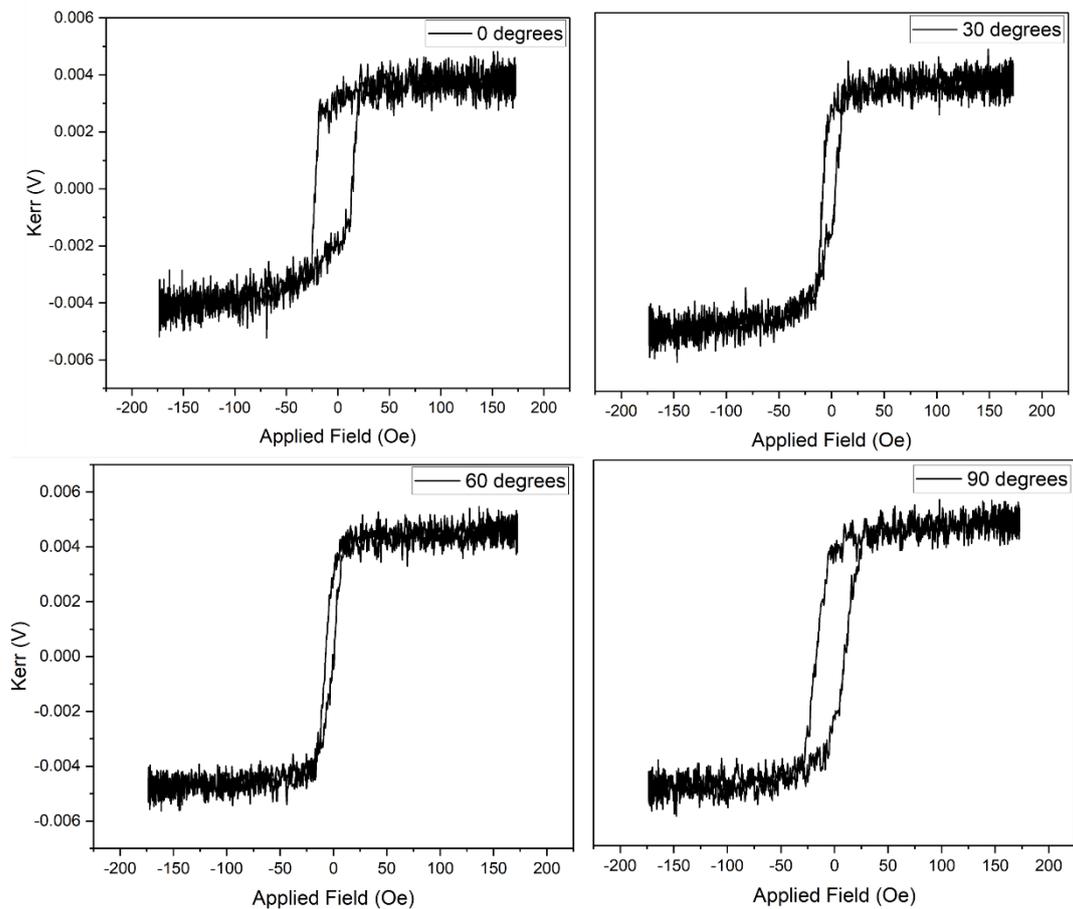

Figure 7.2: presents the results of angular Longitudinal MOKE measurements, depicted as hysteresis loops, for the NiFe/Ag 2.6 nm/NiFe sample at angles of 0, 30, 60, and 90 degrees.

From these observations that we propose that the magnetization behaviour in this system is governed by a complex interplay of factors. Our data suggests that the magnetic coupling across the Ag layer, in conjunction with the intrinsic anisotropies present within these Ag layers, collectively give rise to a nuanced and intricate angular dependence of the magnetization behaviour. This complexity extends beyond a simple superposition of the individual layer properties. However, it can be observed that the interaction facilitated by the Ag layer cooperate with the anisotropies of the neighbouring ferromagnetic layers, resulting in the formation of a different occasionally unexpected angular magnetization profile. This unexpected behaviour shows the crucial role of interlayer interactions in determining the macroscopic magnetic characteristics of these multilayer structures.

7.4.2 Angular Ferromagnetic Resonance (AFMR)

FMR angular measurements allow an in-depth study of magnetic anisotropy by studying the relationship between resonance conditions and the angle. This can reveal important details about the directions of easy and hard axes of magnetisation, which are crucial for understanding the material's magnetic behaviour. Moreover, due to the inherent anisotropy of the material's magnetisation, changes in the resonance field occur as the angle changes. Observing these variations can lead to effective quantification of the anisotropy field [137], thereby establishing a tangible measure of the intensity of the magnetic anisotropy .

FMR angular measurements are also capable of detecting a range of magnetic interactions, encompassing exchange coupling and dipolar interactions, which are key to interpreting the behaviour of magnetic structures like multilayers. FMR angular measurements provide a thorough characterization of both static, anisotropy and exchange coupling, and dynamic properties of magnetic materials. These results highlight the stable and robust magnetic properties of these trilayer structures at room temperature, suggesting their potential suitability for spintronic applications. Especially, the results yielded several key findings. The analysis revealed that the bilinear exchange coupling term is predominant in these samples, with the biquadratic coupling term proving to be at least two orders of magnitude smaller than the bilinear term [19]. Also, it was observed that for extremely thin Ru layer thicknesses, the Co layers are strongly coupled in an antiparallel configuration [19].

The results from our NiFe/Ag/NiFe sample's angular FMR shown in figure 7.3 underscore the presence of magnetic anisotropy. The field range is the same as presented previously, but the frequency range is lower. The lower resonance frequency suggests a smaller saturation magnetisation, about 9706 G [138], as would be expected for NiFe in comparison to CoFe. At a 0-degree angle, which is the easy-axis of the top FM layer, a single resonance field observed across the applied field of 500 to 4000 Oe. The continuous, single resonance throughout the entire range of the applied field indicates that the two ferromagnetic layers appear to precess together, seeing no difference an anisotropy and hence the same effective field. It is expected that the double resonance will be most pronounced where the anisotropy field difference between the two layers is the largest. However, as the sample is rotated to a 15-degree angle, we have observed a change to two separated resonance fields. This change signifies a transition in the sample's behaviour, where the two magnetic layers now see different effective fields, as a result of the built-in magnetic anisotropies in the two layers, and hence precess at slightly different frequencies for a given applied field.
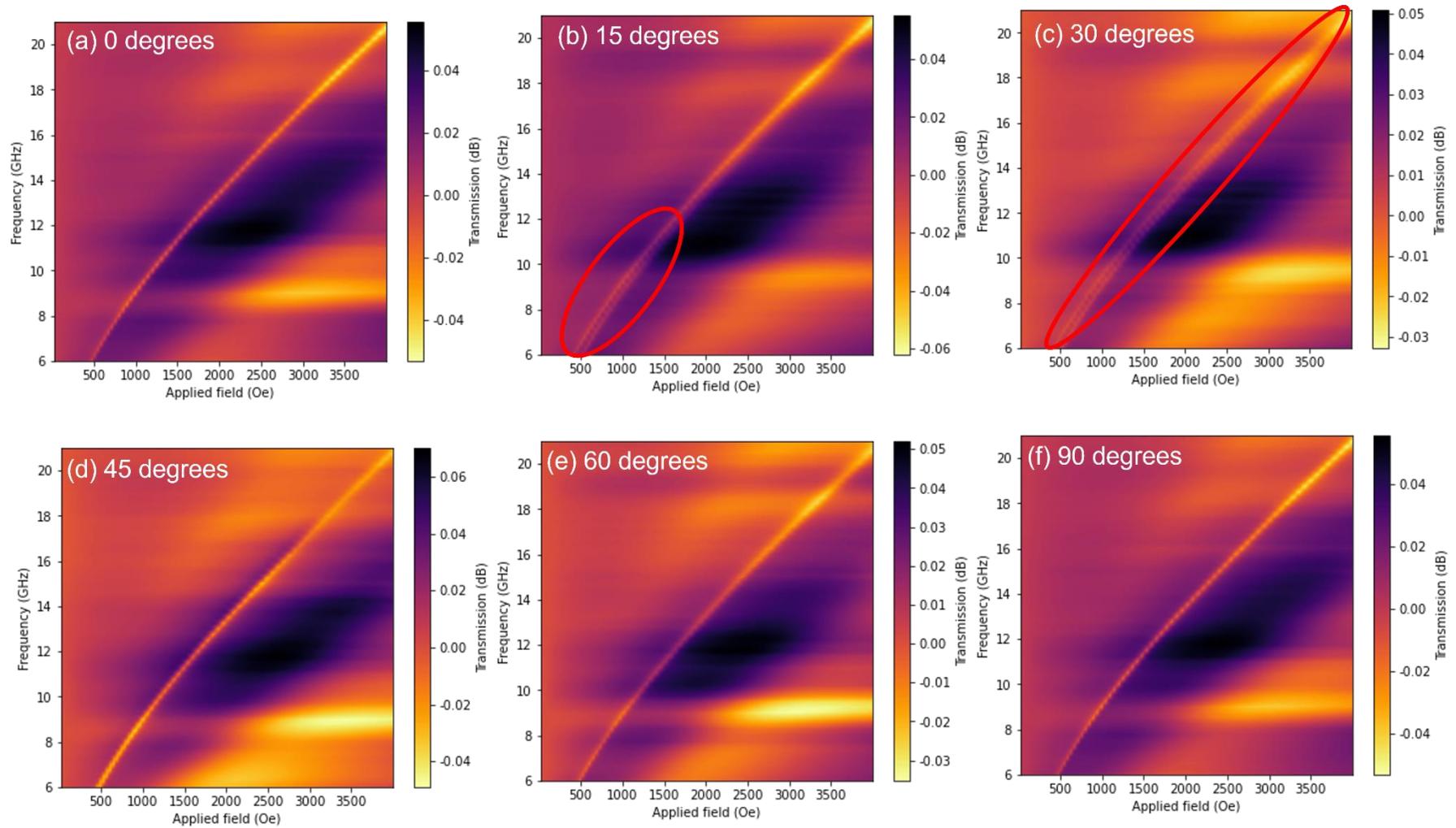
Figure7.3: FMR spectra measured with the applied field aligned at different angles relative to spectrum, where the resonance field in correspondence with frequency against the applied field is graphically represented. These measurements are conducted on a NiFe/Ag 2.6 nm/NiFe sample, with various angular orientations. Notably, the graph emphasizes the manifestation of both solitary and dual resonance fields.

Figure 7.4: Each frame shows fits to the FMR absorption line-shape, with the model, and its various components, as solid lines. Normalised residuals in each case are shown beneath.

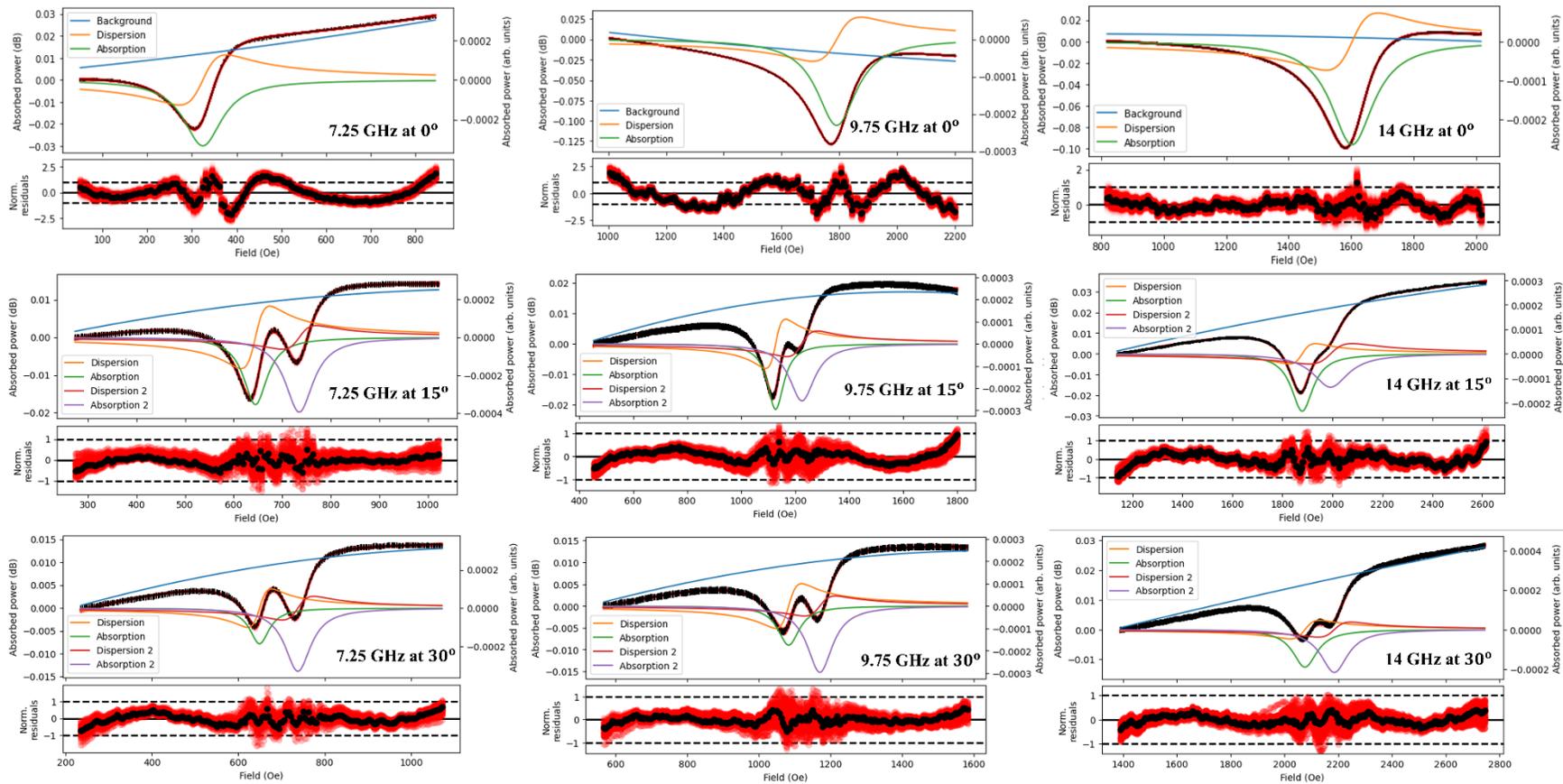Fig 7.3 shows the FMR absorption line-shape for NiFe/Ag(2.6nm)/NiFe sample in different angles, the double resonance is apparent from 500 to 1500 Oe (frequency range 6 to 21 GHz) for only 15 and 30 degrees, but most angles appear as a single apparent resonance at higher field and frequency. This shows that non-colinear easy axes in the two layers do exist and can be observed under certain conditions. The resonances are separated at low field/frequency and become less distinct at higher frequency, this is different from the case in CoFe/Ag (2.6 nm)/CoFe, where any potential impact of non-colinear easy axes linewidth bump is visible only at intermediate frequencies, rather than low or high frequency. The data with two resonances shows the greatest difference in effective field between the two FM layers, creating the largest difference in resonance frequency at a specific applied field. This difference in applied field is due to the combination of the easy/hard axes in the two layers, and the RKKY coupling across the Ag spacer. It is important to note that this aligned with neither the nominal easy or hard axes of either layer in the sample imprinted during growth. Any differences between the effective field in the two FM layers can no longer be clearly resolved. Figure 7.3, (a) shows a single resonance at an angle of 0 degrees. When the sample is rotated to 15 degrees, as seen in (b), two distinct resonances become evident in the 6 to 14 GHz range. At a rotation of 30 degrees, depicted in (c), two clear resonances are observable across all frequencies. When we reach the angles of 45, 60, and 90 degrees as shown in fig 7.3 (d, e and f), there is a return of a single resonance field.

Fig 7.4 shows examples of the angle-dependent line-shape. These plots are similar to those shown for CoFe/Ag/CoFe samples in figures 5.3 and 5.4 in chapter 5. The double-linewidth fits are more complex as they include two Lorentizian line-shapes and hence a larger parameter space. In all cases the fits are good to either a single or double resonance line-shape model, as appropriate. Figure 7.4. showing residuals plot (below the line-shape) reveals that the double line-shape fittings consider relatively stable and even. However, for the single line-shape fittings, variations can be seen on either side of the resonance, suggesting the possibility of double resonance. We have tried to fit this data with a double resonance model, and it does not make any improvement; the fitting tries to fit a single resonance and makes the second resonance either vanishingly small or very broad.
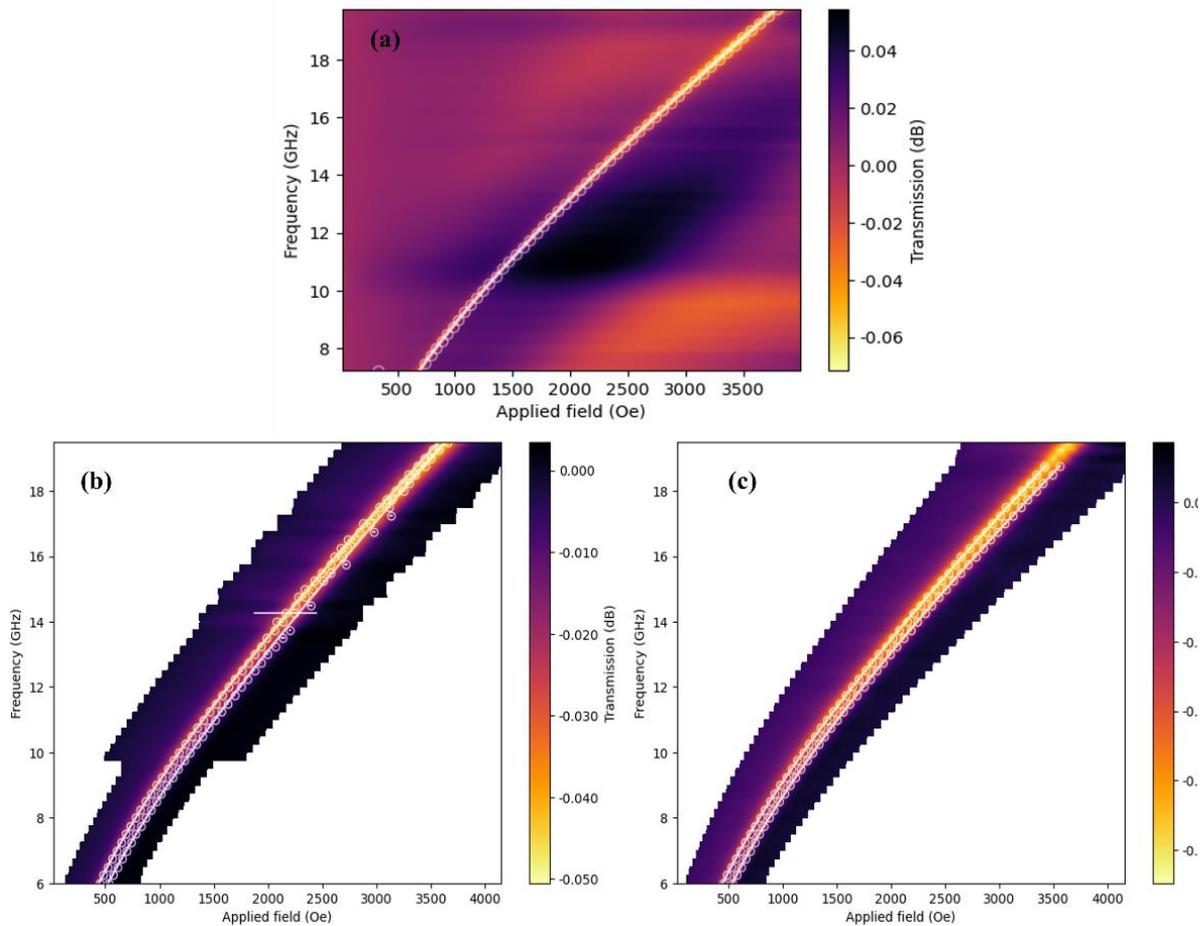
Figure 7.5. Examples of FMR measurements taken for NiFe/Ag (2.6nm)/NiFe, including (a) at 0 degrees, and showing a single resonance, (b) at 15 degrees showing double resonance, (c) at 30 degrees showing double resonance (b). Datapoints show the fitted resonance field at various frequencies, and the solid line is a fit to the Kittel equation

Figure 7.5. shows a good Kittel fit for both a single and double resonance. The three frames in figure 7.5 show the same sample with different measurement angles; 0 degrees where only a single resonance is observed, and 15 and 30 degrees where a clear double resonance is seen.

Figure 7.6: The results of the changes in anisotropy across the range of angles are shown along with the double anisotropy field for the 15- and 30-degree angles. The 15 and 30 angles secondary anisotropy, that correspond to another resonance, marked in blue to clarify.
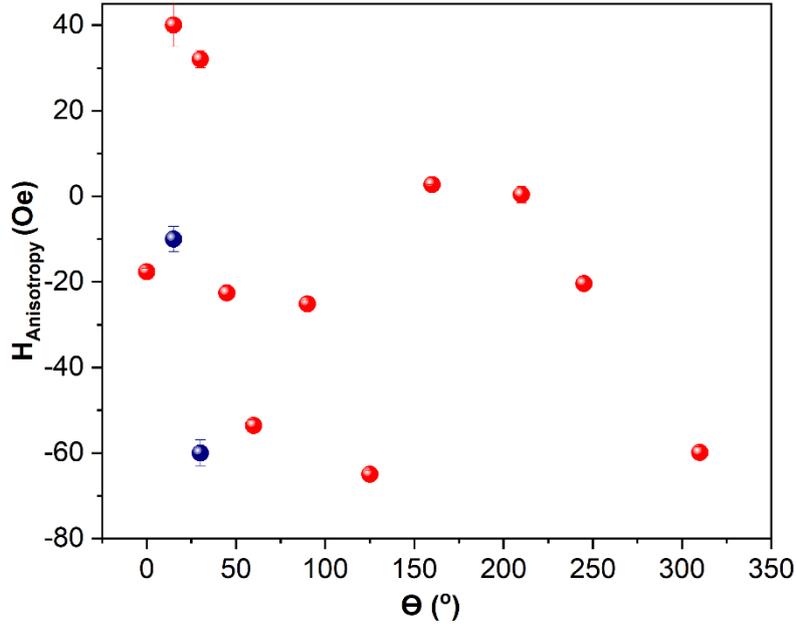
Figure 7.6. shows the change of the anisotropy with different angles. These magnetic anisotropy field is extracted from the Kittel fits as described in chapter 4. For the angles with two resonances each layer has different anisotropy. For instance, at 15 degrees one layer has anisotropy field about + 40 Oe, the other layer -10 Oe. At 30 degrees, the anisotropy field for the first layer is + 32 and - 60 for the other layer. The change in the sign suggests that there are the designated easy-hard axes in the sample. Positive magnetic anisotropy field corresponds to a harder axis, with significant positive anisotropy field observed specifically only at orientations where a clear double resonance is found. The magnetic easy axis should have zero anisotropy field [139]. In the Kittel fitting the anisotropy field is not constrained to be positive, and the negative values found here for most angles suggests that there may be additional effective-field terms missing from the Kittel equation. Also, the anisotropy filed shows no obvious trend with angle. This suggests that the system is more complicated than a single effective uniaxial anisotropy, and that the RKKY coupling may have some more complex impact.
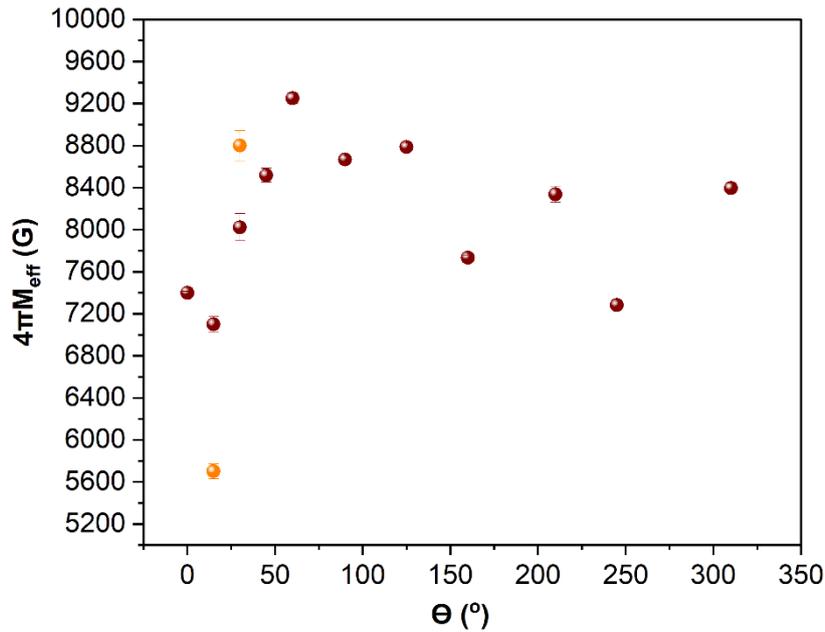
Figure 7.7 displays the fluctuations in the effective magnetization, represented as $4\pi M_{eff}$, in response to changes in the applied angle. The yellow points indicate the secondary $4\pi M_{eff}$ values of 15 and 30 angles.

The obtained effective magnetization from the fit remains relatively constant with respect to angle, as shown in figure 7.7, suggesting that a single-resonance fit is reasonable. The $4\pi M_{eff}$ value in a previous study was report as 9706 ± 1 G [138], and this aligns well with our findings. The consistent $4\pi M_{eff}$ value with changing angle indicates that the material's effective magnetization is largely independent of the orientation in the plane of measurement, as expected. The results from double- resonances fits generally align with this observation although at 15 degrees, where the double resonance is not so well resolved, the second resonance gives an effective magnetization of 5700 G. This may be a result of missing energy terms in the effective field used in the Kittel fitting.

Figure 7.8. Demonstrating an example of fitting double resonances data to determine the Gilbert damping for each resonance and This is the fitting for the line-shape fitted at an angle of 30 degrees.
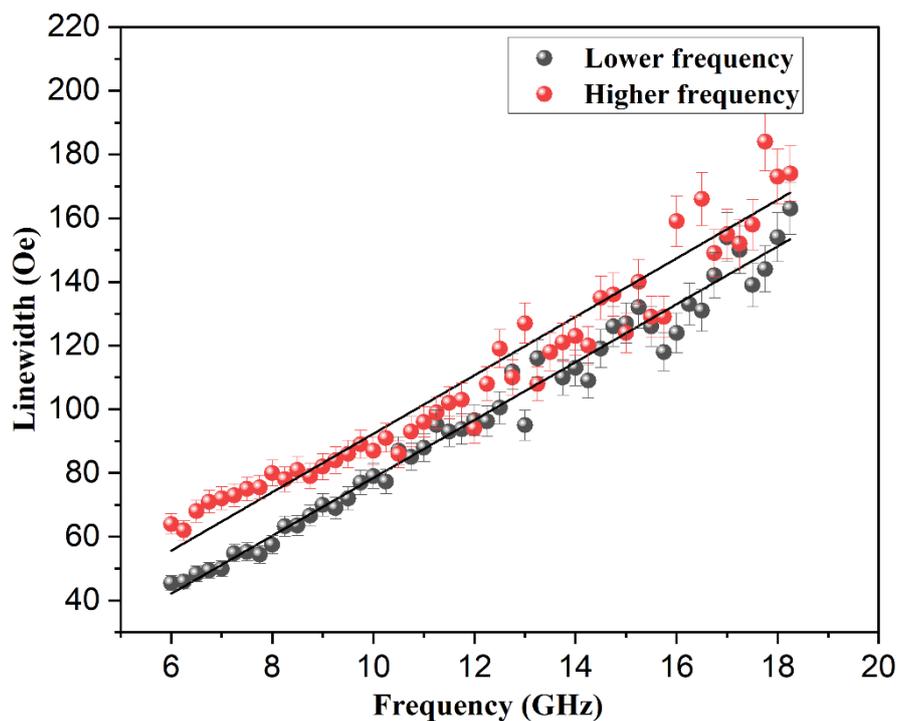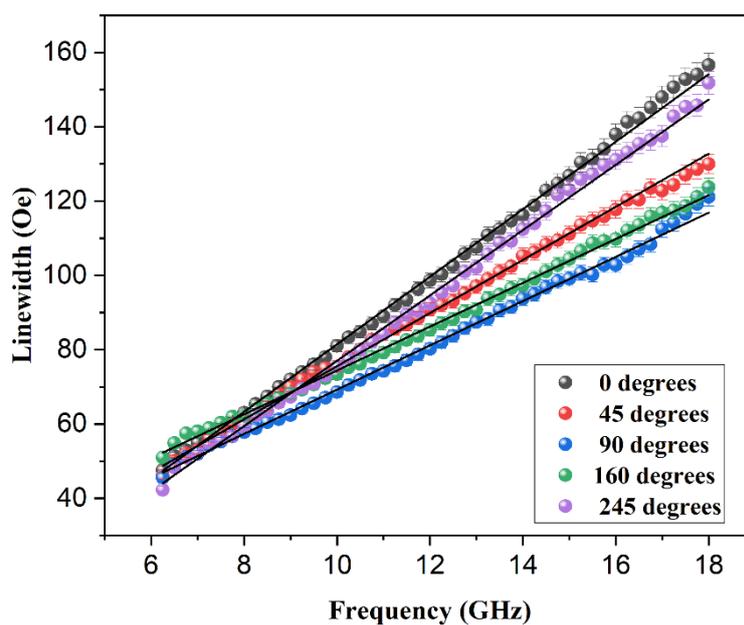

Figure 7.9. showing some examples of fitting single resonances data to determine the Gilbert damping for each resonance. These are the fitting for the line-shape fitted at selected angles.
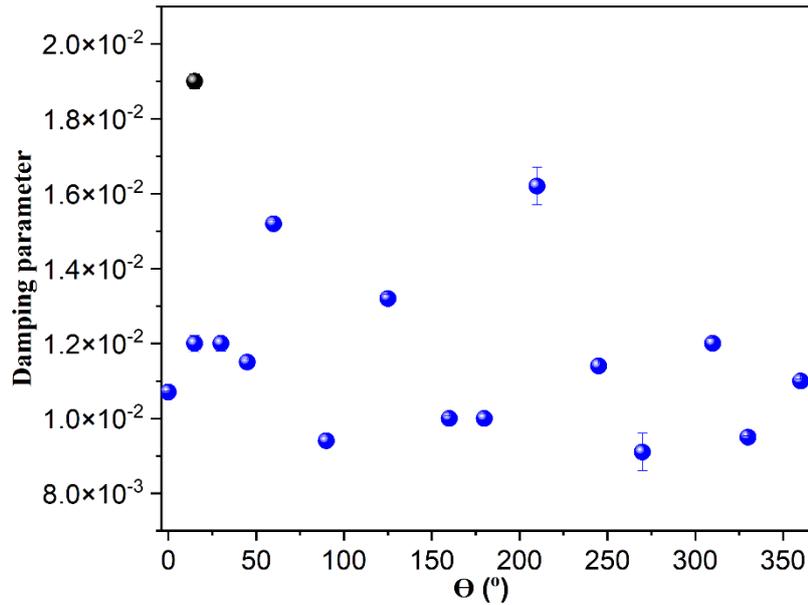
Figure 7.10. Values obtained from the fit of linewidth vs frequency for the NiFe/Ag (2.6nm)/NiFe over various angles are presented. The black points represent the second damping value for angles of 15 and 30 degrees.

Figure 7.8. at 30 degrees data, linear frequency dependence has been observed for both layers, with no bump shown. The same slope for both layers, effective Gilbert damping, is same for both layers as expected. Both layers have the same slope, indicating that the effective Gilbert damping of 0.012, as shown in figure 7.10, is consistent, as expected. This agrees with the findings of a previous study, which determined the magnetic damping of NiFe to be 0.013 [111, 140, 141]. One of the layers shows a slightly greater degree of inhomogeneous damping compared to the other. This might cause by RKKY interaction which induces a variation in the preferred axis orientations within the upper layer. This is due to the fact that the magnetization of a cluster during its initial growth may slightly shift either to the left or to the right from the magnetization of the first layer. At 15 degrees, we could not get a good double of linewidth fits from as the two peaks are less well resolved. As can be seen in Figure 7.9, single resonance displays linear frequency behaviour independent of angles. Since the layers are precessing differently, we have expected the biggest spin-pump effect; however, no such bump is observed. In addition, we have tried to fit two resonances, so we could not have any apparent broadening due to an unresolved second peak. This could suggest that this is the cause of the bump. The values for magnetic damping generally around the range of 0.012. The general trend demonstrates behaviour that is consistent for both single and double resonance, with only occasional and insignificant increases in value. These values are higher, compared to the CoFe/Ag/CoFe samples with an average of about 0.0030. This indicates that the NiFe/Ag/NiFe

samples exhibit greater magnetic damping than the CoFe samples. It is possible that various materials and layer structures might exhibit different magnetic properties. For all the NiFe samples, single resonance fits did not show the same feature as seen in the CoFe samples, a bump. This observation implies that the anisotropies might not be the primary factor causing this bump. Instead, it could be more closely associated with spin current dynamics. In observing two resonance signals at 15 and 30 degrees in the NiFe sample, it is likely to assume that the obvious bump in the CoFe samples is for double resonances. However, in the case of CoFe, only one of these resonances appears clearly in our measurements. One of the resonances might dominate due to factors like signal overlap, inherent magnetic properties, or interfacial effects, thereby obscuring the other resonance in the measurements.

Summary

The variation of magnetic anisotropy during the thin film deposition process significantly shapes the behaviour of the precessional dynamics within the system. Nominally imprinted during the growth phase, magnetic anisotropy critically impacts magnetization dynamics within the material, an influence that can be observed via variations in linewidth corresponding to changes in the direction of the applied magnetic field. Our experimental findings emphasize the complicated nature of the interplay between imprinted magnetic anisotropies and the antiferromagnetic coupling across the Ag spacer layer. The double resonance anticipated due to the difference between effective fields corresponding to crossed easy and hard axes of magnetization appear only when the sample is oriented at around 30 degrees off the nominal easy axis of the lower FM layer. This observation highlights the significant impact of the RKKY coupling across the Ag layer on determining both the static and dynamic behaviours. Both single and double resonances data exhibit linear frequency behaviour that are unaffected by angle variations. Notably, the $4\pi M_{eff}$ value across varied angles highlights that the effective magnetization of the material remains consistent, regardless of its in-plane orientation during measurements. In addition, magnetic damping values are consistent. This provides a possible explanation for the enhanced linewidth in CoFe/Ag/CoFe materials might explain about the anisotropy in the upper CoFe being set at an angle to the EA in the lower FM due to the RKKY interaction and the ways in which this can impact on the apparent damping

Chapter 8: Conclusion and further work

In this thesis, we have investigated the influence of spin-pumping on the energy dissipation process between two homogenous FM magnetic films, each with a thickness of 10 nm. These magnetic layers are separated by a layer of Ag that have deposited onto Si/SiO_2 substrates by magnetron sputtering. The precessional dynamics was studied using ferromagnetic resonance. Also, we have studied the effects of engineering different magnetic anisotropies in the two FM layers.

8.1 Summary and conclusion

In chapter 5, the results have presented the exhibit an interesting dependency of effective magnetic damping on the thickness of Ag within the CoFe/Ag/CoFe trilayer samples. This study indicates a notable difference between the observed damping values and those typically reported in existing literature for comparable material systems. This raises questions about the possible factors contributing to these variances. A reasonable explanation for the heightened effective damping observed in non-linear frequency-dependent samples could be from the two-magnon scattering, where the interactions or scattering events between spin waves result in augmented damping. Also, the thickness of Ag appears to be leading in the effective magnetic damping of the tri-layer samples. The findings suggest that samples with a linear frequency dependence of resonance could exhibit lower damping compared to those with non-linear frequency dependence, as they typically represent well-defined resonance modes and coherent magnetization dynamics.

As the relationship between damping and frequency dependence is multifaceted, varying with different experimental conditions and material properties. Other factors, including magnetic anisotropy, magnetic interactions, and the presence of spin-pumping or spin-transfer torque effects, can independently affect damping. The study also indicates the possibility of RKKY interaction influencing effective damping, particularly in the non-linear frequency-dependent samples. This interaction induces antiferromagnetic coupling via the Ag layer between the CoFe layers, possibly leading to enhanced magnetic damping through spin-pumping. The RKKY interaction could also potentially affect the alignment of the easy axis in the second FM layer during its initial growth stages, creating different resonant conditions for

the precession of the two layers. This can induce phenomena such as spin-pumping effects, overlapping of resonances, and the excitation of acoustic and optical modes.

Chapter 6 provides a description of the analysis of XRR) and PNR-PA data for a CoFe/Ag/CoFe system. By employing the best fit models, at 0 and 45 degrees of sample rotation, the FM upper layer shows magnetic anisotropy due to its magnetic angle difference from the FM lower layer. The anisotropy could affect the lower layer through RKKY interaction through the Ag layer. The higher layer's magnetic coupling preference can change as these oscillations cross the spacer. The coupling change might rotate the upper layer's anisotropy direction, misaligning it with the lower layer.

We observed an increase in the magnetic SLD during a 45-degree scan. We believe this increase signifies the presence of anisotropic magnetic properties in the system, potentially arising due to a multitude of factors, including the intricacies of the spin interactions between the CoFe layers and the Ag layer. The magnetization appears to align predominantly parallel to the layer plane, a condition likely influenced by the magnetic anisotropy of the system. Factors such as interlayer coupling and magneto-crystalline anisotropy could be key contributors to this behaviour, and further studies will need to investigate these factors.

The investigations carried out in Chapter 7 provide valuable insights into the role of magnetic anisotropy during thin film deposition and its impact on key magnetic properties. Our study of magnetic anisotropy across different angles raises the possibility that this property may play an important role in defining the linewidth behaviour and magnetic damping within the system. This is because, in specific angles during the Ferromagnetic Resonance (FMR) measurements, double resonances became apparent. Observations indicate that variations in magnetic anisotropy significantly influence magnetization dynamics in the material, an effect clearly discernible through corresponding linewidth variations that align with changes in the applied magnetic field direction. This features that magnetic anisotropy is not a static property fixed during the growth phase, but it actively dictates the material's magneto-dynamic behaviour.

The intricate dynamics between imprinted magnetic anisotropies and the antiferromagnetic coupling across the Ag spacer layer are evident from our experimental data. The double resonance, expected from the disparity between effective fields aligned to crossed easy and hard magnetization axes, becomes noticeable only when the sample's

orientation is roughly 30 degrees off the principal easy axis of the lower ferromagnetic layer. This points to the profound role of the RKKY coupling across the Ag layer in steering both static and dynamic magnetism. The tailored magnetic anisotropy during film deposition offers a pathway to directly manipulate linewidth behaviour and adapt the magnetic damping traits of multilayer specimens. Such modulations might account for the augmented linewidth observed in CoFe/Ag/CoFe structures, with the anisotropy in the topmost CoFe layer being angled to the easy axis of the lower ferromagnetic layer due to RKKY interactions. This angle might influence the observed damping.

Comparatively, the NiFe/Ag/NiFe samples demonstrated a heightened magnetic damping relative to their CoFe counterparts. Such disparities suggest that distinct material compositions and structural layouts can yield varied magnetic responses. For the NiFe specimens, single resonance fits did not manifest the characteristic bump present in the CoFe samples, leading to the hypothesis that factors beyond anisotropies, potentially spin current dynamics, might be at play. While the NiFe sample displayed two resonance signals at specific angles, suggesting that the prominent bump in CoFe samples might be attributed to double resonances, the CoFe samples predominantly exhibited a single pronounced resonance. This dominance could be attributed to mechanisms such as signal interferences, intrinsic magnetic attributes, or interface.

8.2 Future Work

The findings from our study explain several potential chances for future scientific investigations. Especially, the observed escalation in effective damping in samples exhibiting non-linear frequency dependence encourages an in-depth study the variation in the amplitude of magnetization precession. Given the convoluted relationship between damping and frequency, which is impacted by a multitude of factors like magnetic anisotropy, magnetic interactions, as well as spin-related phenomena, it is advisable to conduct a detailed exploration of these elements. It is crucial to disentangle the intertwined aspects to fully understand the behaviour and properties of these multilayer systems. Further probing of the RKKY interaction's influence on effective damping, notably evident in non-linear frequency-dependent samples, could provide significant insights. Understanding how this interaction impacts the initial stages of ferromagnetic layer growth may reveal how typical resonance conditions are created. Similarly, investigating in detail the changes in structural and magnetic

SLD at the Ag/CoFe or CoFe/Ag interfaces would help show the effects of compositional variations on the magnetic properties of the system.

Moreover, a focused analysis of the impact of negligeable variations in the thickness of the Ag layer on the system's interlayer coupling and resonance behaviour could potentially create beneficial insights, even though these variations may appear negligible at first look. Our study has strongly connected magnetic anisotropy with the thin film deposition process. This link can be used to manipulate anisotropy during the thin film growth process. Such a strategy provides a promising way to use control over magnetic properties, demonstrating the capability of tailoring magnetic properties at will in a controlled laboratory environment. Lastly, the apparent angular dependencies of damping and effective magnetization present exciting opportunities for further investigation, particularly into the role of anisotropy. Investigating these areas could lead to substantial advancements in our understanding of how the damping properties of a material can be manipulated. These suggested research directions, while challenging, offer considerable potential for enhancing our understanding of magnetic properties in thin films, thereby contributing significantly to the field of spintronics.

Measuring the Ruderman-Kittel-Kasuya-Yosida (RKKY) coupling involves a multifaceted approach that combines experimental techniques with theoretical analysis. The variation in the magnetization configuration with applied field can be determkined by PNR, and then the RKKY coupling determined by fitting this variation to appropriate expressions for the energy density.

References

1. Žutić, I., J. Fabian, and S. Das Sarma, *Spintronics: Fundamentals and applications.* Reviews of Modern Physics, 2004. **76**(2): p. 323-410.

2. Azzawi, S.A.R.H., *Understanding and Controlling Magnetic Damping Behaviour in Synthetic Ferromagnetic Thin-film Multilayers.* 2018: Durham University.

3. Bandyopadhyay, S.C., M. , *Introduction to spintronics.* CRC press, 2015.

4. Shanavas, K.V., Z.S. Popović, and S. Satpathy, *Theoretical model for Rashba spin-orbit interaction in d electrons.* Physical Review B, 2014. **90**(16): p. 165108.

5. Cullity, B.G., C, *Introduction to Magnetic Materials.* Introduction to Magnetic Materials, ed. 2. Vol. 241–273 2009.

6. Wang, Z.J., et al., *Spin-wave resonance in ferromagnetic coupled Co/Cu multilayers.* Journal of Magnetism and Magnetic Materials, 1997. **176**(2): p. 127-133.

7. Gilbert, T.L., *A phenomenological theory of damping in ferromagnetic materials.* IEEE Transactions on Magnetics, 2004. **40**(6): p. 3443-3449.

8. McHenry, M.E. and D.E. Laughlin, *Magnetic Moment and Magnetization*, in *Characterization of Materials*. p. 1-25.

9. Spaldin, N.A., *Magnetic materials: fundamentals and applications* 2010: CambridgeUniversity Press.

10. Coey, J.M.D., *Magnetism and Magnetic Materials*. 2010, Cambridge: Cambridge University Press.

11. Aharoni, A., *Introduction to the Theory of Ferromagnetism.* 2000: Oxford University Press.

12. Slater, J.C., *Atomic Shielding Constants.* Physical Review, 1930. **36**(1): p. 57-64.

13. Slater, J.C., *Cohesion in Monovalent Metals.* Physical Review, 1930. **35**(5): p. 509-529.

14. Walker, L.R., *Ferromagnetic-Relaxation Theory. Marshall Sparks. McGraw-Hill, New York, 1964. xii + 227 pp. Illus. $12.50.* Science, 1965. **148**(3667): p. 218.

15. Bogart, L.K. *An investigation of the structure, pinning and magnetoresistance of domain walls in NiFe planar nanowires*. 2010.

16. Stoner, E.C., *Collective Electron Ferromagnetism. II. Energy and Specific Heat.* Proceedings of The Royal Society A: Mathematical, Physical and Engineering Sciences, 1939. **169**: p. 339-371.

17. Slater, J.C., *The Ferromagnetism of Nickel.* Physical Review, 1936. **49**(7): p. 537-545.

18. Ota or Ohta, N., *Magnetic Moment and Band Structure Analysis of Fe, Co, Ni-modified Graphene-nano-ribbon.* Vol. arXiv. 2014. 4504.

19. Morrish, A.H.e.a., *The physical principles of magnetism*. 1965: Wiley Online Library.

20. Kimura, T., J. Hamrle, and Y. Otani, *Estimation of spin-diffusion length from the magnitude of spin-current absorption: Multiterminal ferromagnetic/nonferromagnetic hybrid structures.* Physical Review B, 2005. **722525**.

21. Kittel, C., *On the Theory of Ferromagnetic Resonance Absorption.* Physical Review, 1948. **73**(2): p. 155-161.

22. Jiles, D., *Introduction to magnetism and magnetic materials* CRC press, 2015.

23. Jiles, D., *Introduction to magnetism and magnetic materials*. 2015: CRC press.

24. Azzawi, S., et al., *Evolution of damping in ferromagnetic/nonmagnetic thin film bilayers as a function of nonmagnetic layer thickness.* Physical Review B, 2016. **93**(5): p. 054402.

25. Kalarickal, S.S., et al., *Ferromagnetic resonance linewidth in metallic thin films: Comparison of measurement methods.* Journal of Applied Physics, 2006. **99**(9): p. 093909.

26. Tokaç, M., et al., *Interfacial Structure Dependent Spin Mixing Conductance in Cobalt Thin Films.* Physical Review Letters, 2015. **115**(5): p. 056601.

27. Swann, S., *Magnetron sputtering.* Physics in Technology, 1988. **19**(2): p. 67.

28. Kawamura, M., et al., *Formation of ultra-thin continuous Pt and Al films by RF sputtering.* Thin Solid Films, 2000. **377-378**: p. 537-542.

29. Farooq, M. and Z.H. Lee, *Optimization of the sputtering process for depositing composite thin films.* Journal of the Korean Physical Society, 2002. **40**: p. 511-515.

30. Grove, W.R., *On the electro-chemical polarity of gases.* Abstracts of the Papers Communicated to the Royal Society of London, 1854. **6**: p. 168-169.

31. Liou, S.H., et al., *Magnetic properties of nanometer-size CoPt particles.* Journal of Applied Physics, 1996. **79**(8): p. 5060-5062.

32. Sharma, N., et al., *The microstructure and magnetic properties of cobalt-rich Co-Pt alloy thin films grown using ion-beam-assisted deposition.* Journal of Physics D, 1998. **31**: p. 3020-3027.

33. Frank, F.C. and J.H. van der Merwe, *One-dimensional dislocations. I. Static theory.* Proceedings of the Royal Society of London. Series A. Mathematical and Physical Sciences, 1949. **198**: p. 205 - 216.

34. Ibach, H., *Physics of Surfaces and Interfaces*. 2006: Springer Berlin Heidelberg.

35. Raheem, Z., *Kittel, Charles - Introduction To Solid State Physics 8Th Ed*. 2019.

36. Gilmore, K., Y.U. Idzerda, and M.D. Stiles, *Spin-orbit precession damping in transition metal ferromagnets (invited).* Journal of Applied Physics, 2008. **103**(7): p. 07D303.

37. Holý, V., et al., *Effect of interfacial-roughness replication on the diffuse X-ray reflection from periodical multilayers.* Applied Physics A, 1995. **60**: p. 93-96.

38. Anagnost, K.M., et al., *Simulating 50 keV X-ray Photon Detection in Silicon with a Down-Conversion Layer.* Sensors (Basel, Switzerland), 2021. **21**(22): p. 7566.

39. Daillant, J. and A. Gibaud, *X-Ray and Neutron Reflectivity: Principles and Applications*. Vol. 58. 2008.

40. Tolan, M., *X-ray scattering from soft-matter thin films : materials science and basic research*. 1999, New York :: Springer.

41. Parratt, L.G., *Surface Studies of Solids by Total Reflection of X-Rays.* Physical Review, 1954. **95**: p. 359-369.

42. Gilmore, K., Y.U. Idzerda, and M.D. Stiles, *Identification of the Dominant Precession-Damping Mechanism in Fe, Co, and Ni by First-Principles Calculations.* Physical Review Letters, 2007. **99**(2): p. 027204.

43. Als-Nielsen, J., *Elements of Modern X-Ray Physics*. Vol. 55. 2002.

44. Ogi, A. and K. Inaba. *X-ray thin-film measurement techniques VI . Small Angle X-ray Scattering*.

45. Björck, M. and G. Andersson, *GenX: An extensible X-ray reflectivity refinement program utilizing differential evolution.* Journal of Applied Crystallography - J APPL CRYST, 2007. **40**: p. 1174-1178.

46. Faraday, M., *Experimental Researches in Electricity. Nineteenth Series.* Philosophical Transactions of the Royal Society of London, 1846. **136**: p. 1-20.

47. Bland, J., M. Padgett, and R. Butcher, *Intensity-stabilised He-Ne laser for measuring small magneto-optic Kerr rotations from thin ferromagnetic films.* Journal of Physics E Scientific Instruments, 2000. **22**: p. 308.

48. *Handbook of Spintronics*, ed. Y. Xu, D.D. Awschalom, and J. Nitta. 2015: Springer.

49. Chadwick, J., *Possible Existence of a Neutron.* Nature, 1932. **129**(3252): p. 312-312.

50. Majkrzak, C.F., K.V. O'Donovan, and N.F. Berk, *CHAPTER 9 - Polarized Neutron Reflectometry*, in *Neutron Scattering from Magnetic Materials*, T. Chatterji, Editor. 2006, Elsevier Science: Amsterdam. p. 397-471.

51. Shirane, G., S.M. Shapiro, and J.M. Tranquada, *Neutron Scattering with a Triple-Axis Spectrometer: Basic Techniques*. 2002, Cambridge: Cambridge University Press.

52. Lilley, J., *Nuclear Physics: Principles and Applications*. 2013: Wiley.

53. Blundell, S.J. and J.A.C. Bland, *Polarized neutron reflection as a probe of magnetic films and multilayers.* Physical Review B, 1992. **46**(6): p. 3391-3400.

54. Lynn, J.W., *Magnetic neutron scattering (invited).* Journal of Applied Physics, 1994. **75**(10): p. 6806-6810.

55. Farle, M., *Ferromagnetic resonance of ultrathin metallic layers.* Reports on Progress in Physics, 1998. **61**(7): p. 755-826.

56. Griffiths, J.H.E., *Anomalous High-frequency Resistance of Ferromagnetic Metals.* Nature, 1946. **158**(4019): p. 670-671.

57. Pozar, D.M., *Microwave Engineering, 4th Edition.* 2011: Wiley.

58. Kamberský, V., *On ferromagnetic resonance damping in metals.* Czechoslovak Journal of Physics B, 1976. **26**: p. 1366-1383.

59. Lenz, K., et al., *Two-magnon scattering and viscous Gilbert damping in ultrathin ferromagnets.* Physical Review B, 2006. **73**(14): p. 144424.

60. Barati, E., et al., *Calculation of Gilbert damping in ferromagnetic films.* EPJ Web of Conferences, 2013. **40**: p. 18003.

61. Sun, Y., et al., *Damping in Yttrium Iron Garnet Nanoscale Films Capped by Platinum.* Physical Review Letters, 2013. **111**(10): p. 106601.

62. Rantschler, J., et al., *Effect of 3d, 4d, and 5d transition metal doping on damping in permalloy thin films.* Journal of Applied Physics, 2007. **101**: p. 033911.

63. Malinowski, G., et al., *Control of speed and efficiency of ultrafast demagnetization by direct transfer of spin angular momentum.* Nature Physics, 2008. **4**(11): p. 855-858.

64. Berger, L., *Effect of interfaces on Gilbert damping and ferromagnetic resonance linewidth in magnetic multilayers.* Journal of Applied Physics, 2001. **90**(9): p. 4632-4638.

65. Weber, R., et al., *Gilbert damping of CoFe-alloys.* Journal of Physics D: Applied Physics, 2019. **52**(32): p. 325001.

66. Zhang, B., et al., *High Corrosion Resistance of NiFe-Layered Double Hydroxide Catalyst for Stable Seawater Electrolysis Promoted by Phosphate Intercalation.* Small, 2022. **18**(45): p. 2203852.

67. Tserkovnyak, Y., A. Brataas, and G.E.W. Bauer, *Enhanced Gilbert Damping in Thin Ferromagnetic Films.* Physical Review Letters, 2002. **88**(11): p. 117601.

68. Marcham, M.K., et al., *Phase-resolved x-ray ferromagnetic resonance measurements of spin pumping in spin valve structures.* Physical Review B, 2013. **87**(18): p. 180403.

69. Hait, S., et al., *Impact of ferromagnetic layer thickness on the spin pumping in Co 60 Fe 20 B 20/Ta bilayer thin films.* Journal of Materials Science: Materials in Electronics, 2021. **32**: p. 12453-12465.

70. Swindells, C. and D. Atkinson, *Interface enhanced precessional damping in spintronic multilayers: A perspective.* Journal of Applied Physics, 2022. **131**(17).

71. Fazlali, M., *Magnetodynamics of pseudo spin valves investigated using co-planar waveguide and spin torque ferromagnetic resonance techniques.* 2017.

72. Chiba, T., G.E.W. Bauer, and S. Takahashi, *Magnetization damping in noncollinear spin valves with antiferromagnetic interlayer couplings.* Physical Review B, 2015. **92**(5): p. 054407.

73.   Gong, Y., et al., *Determination of magnetic anisotropies, interlayer coupling, and magnetization relaxation in FeCoB/Cr/FeCoB.* Journal of Applied Physics, 2009. **106**: p. 063916.

74.   Chen, X., et al., *Ferromagnetic resonance modes of a synthetic antiferromagnet at low magnetic fields.* Journal of Physics: Condensed Matter, 2022. **34**(1): p. 015802.

75.   Tanaka, K., et al., *Linewidth broadening of optical precession mode in synthetic antiferromagnet.* Applied Physics Express, 2014. **7**(6): p. 063010.

76.   Warnicke, P., et al., *Exploring the accessible frequency range of phase-resolved ferromagnetic resonance detected with x-rays.* Journal of Applied Physics, 2013. **113**(3).

77.   Jiles, D., *Introductio to Magnetism and Magnetic Materials*. Introductio to Magnetism and Magnetic Materials

ed. 2. 2005: CRC Press Company.

78.   Zhang, C., *Spin-orbit torque damping control and auto-oscillations of dipole field-localized spin wave modes*. 2018, The Ohio State University.

79.   Tserkovnyak, Y., et al., *Nonlocal magnetization dynamics in ferromagnetic heterostructures.* Reviews of Modern Physics, 2005. **77**(4): p. 1375-1421.

80.   Zwierzycki, M., et al., *First-principles study of magnetization relaxation enhancement and spin transfer in thin magnetic films.* Physical Review B, 2005. **71**(6): p. 064420.

81.   Bass, J. and W.P. Pratt, *Spin-diffusion lengths in metals and alloys, and spin-flipping at metal/metal interfaces: an experimentalist's critical review.* Journal of Physics: Condensed Matter, 2007. **19**(18): p. 183201.

82.   Bruno, P., *Theory of interlayer magnetic coupling.* Physical Review B, 1995. **52**(1): p. 411-439.

83.   Körner, H.S., et al., *Magnetic damping in poly-crystalline Co25Fe75: Ferromagnetic resonance vs. spin wave propagation experiments.* Applied Physics Letters, 2017. **111**(13).

84.   Yadagiri, K., et al., *Ferromagnetic resonance properties of multilayer FeGaB/Ta/FeGaB structure.* Journal of Materials Science: Materials in Electronics, 2022. **33**(7): p. 3870-3879.

85.   Harder, M., et al., *Analysis of the line shape of electrically detected ferromagnetic resonance.* Physical Review B, 2011. **84**(5): p. 054423.

86.   Medwal, R., et al., *Spin Pumping in Asymmetric Fe50Pt50/Cu/Fe20Ni80 Trilayer Structure.* physica status solidi (RRL) – Rapid Research Letters, 2019. **13**(10): p. 1900267.

87.   Yafuso, M., et al., *Nonlinear power dependence of ferromagnetic resonance in NiFe/Pt/CoFeB trilayer.* Journal of Physics: Condensed Matter, 2022. **34**(4): p. 045801.

88.   Zhang, Y., et al., *Significant and Nonmonotonic Dynamic Magnetic Damping in Asymmetric CoFeRu/CoFe Trilayers.* Physical Review Applied, 2022. **17**(3): p. 034033.

89.   Li, Y., et al., *Anomalous Gilbert damping induced by the coexisting static and dynamic coupling in Fe/Pd/Fe trilayers.* Physical Review B, 2021. **104**(9): p. 094409.

90.   Panigrahi, B., et al., *Effect of Ta capping layer on spin dynamics in Co50Fe50 thin films.* Solid State Communications, 2022. **348-349**: p. 114743.

91.   Zhu, L., et al., *Origin of Strong Two-Magnon Scattering in Heavy-Metal/Ferromagnet/Oxide Heterostructures.* Physical Review Applied, 2020. **13**(3): p. 034038.

92.   Pogoryelov, Y., et al., *Nonreciprocal spin pumping damping in asymmetric magnetic trilayers.* Physical Review B, 2020. **101**(5): p. 054401.

93.   Khivintsev, Y., et al., *Nonlinear ferromagnetic resonance in permalloy films: A nonmonotonic power-dependent frequency shift.* Physical Review B, 2010. **81**(5): p. 054436.

94.   Mizukami, S., et al., *Low damping constant for Co2FeAl Heusler alloy films and its correlation with density of states.* Journal of Applied Physics, 2009. **105**(7).

95.   Lee, H., et al., *Magnetization relaxation and structure of CoFeGe alloys.* Applied Physics Letters, 2009. **95**(8).

96.   Landeros, P., R.E. Arias, and D. Mills, *Two magnon scattering in ultrathin ferromagnets: The case where the magnetization is out of plane.* Physical Review B, 2008. **77**(21): p. 214405.

97.   González-Guerrero, M., et al., *Engineering the magnetic properties of amorphous (FeCo)B20 with multilayers of variable anisotropy direction.* Applied Physics Letters, 2007. **90**(16).

98.   Ankner, J.F. and G.P. Felcher, *Polarized-neutron reflectometry.* Journal of Magnetism and Magnetic Materials, 1999. **200**(1): p. 741-754.

99.   Majkrzak, C.F., *Polarized neutron reflectometry.* Physica B: Condensed Matter, 1991. **173**(1): p. 75-88.

100.   Als-Nielsen, J.M., D, *Elements of modern X-ray physics* ed. 2. 2011, John Wiley& Sons.

101.   Binek, C., A. Hochstrat, and W. Kleemann, *Exchange bias in a generalized Meiklejohn–Bean approach.* Journal of Magnetism and Magnetic Materials, 2001. **234**(2): p. 353-358.

102.   Steadman, P., et al., *Exchange bias in spin-engineered double superlattices.* Physical review letters, 2002. **89**(7): p. 077201.

103.   Mauri, D., et al., *Simple model for thin ferromagnetic films exchange coupled to an antiferromagnetic substrate.* Journal of Applied Physics, 1987. **62**(7): p. 3047-3049.

104.   Singh, S., et al., *Physical and magnetic roughness at metal-semiconductor interface using x-ray and neutron reflectometry.* Journal of Applied Physics, 2010. **107**(12).

105.   Zhu, T., et al., *The study of perpendicular magnetic anisotropy in CoFeB sandwiched by MgO and tantalum layers using polarized neutron reflectometry.* Applied Physics Letters, 2012. **100**(20).

106.   Park, S., et al., *Magnetic degradation of an FeCo/ GaAs interface.* Physical Review B, 2004. **70**(10): p. 104406.

107.   Park, S., et al., *The influence of growth temperature and annealing on the magnetization depth profiles across ferromagnetic/semiconductor interfaces.* Journal of Applied Physics, 2008. **104**(8).

108.   Parkin, S.S.P., A. Mansour, and G.P. Felcher, *Antiferromagnetic interlayer exchange coupling in sputtered Fe/Cr multilayers: Dependence on number of Fe layers.* Applied Physics Letters, 1991. **58**(14): p. 1473-1475.

109.   Kim, K.-Y., et al., *Long-range interlayer-coupled magnetization reversal mediated by the antiferromagnetic layer in Py/FeMn/CoFe trilayers.* Physical Review B, 2011. **84**(14): p. 144410.

110.   Parkin, S.S.P., N. More, and K.P. Roche, *Oscillations in exchange coupling and magnetoresistance in metallic superlattice structures: Co/Ru, Co/Cr, and Fe/Cr.* Physical Review Letters, 1990. **64**(19): p. 2304-2307.

111.   Kumar, D. and A. Gupta, *Effects of Interface Roughness on Interlayer Coupling in Fe/Cr/Fe Structure.* Hyperfine Interactions, 2005. **160**(1): p. 165-172.

112.   Luby, S., et al., *Effect of magnetic flux distribution on GMR in Ag/Co multilayers.* Thin Solid Films, 2003. **433**(1): p. 243-246.

113.   Luby, S., et al., *Thermal behaviour of Co/Si/W/Si multilayers under rapid thermal annealing.* Applied Surface Science, 1999. **150**(1): p. 178-184.

114.   Bandiera, S., et al., *Asymmetric Interfacial Perpendicular Magnetic Anisotropy in Pt/Co/Pt Trilayers.* IEEE Magnetics Letters, 2011. **2**: p. 3000504-3000504.

115.   Kim, D.-O., et al., *Asymmetric magnetic proximity effect in a Pd/Co/Pd trilayer system.* Scientific Reports, 2016. **6**(1): p. 25391.

116.   Finazzi, M., L. Duo, and F. Ciccacci, *Magnetic properties of interfaces and multilayers based on thin antiferromagnetic oxide films.* Surface science reports, 2009. **64**(4): p. 139-167.

117.   Naik, B., et al., *Preparation of magnetically separable CoFe2O4 supported Ag nanocatalysts and catalysis reaction towards decolorization of variety of dyes.* RSC Adv., 2015. **5**.

118.   *Kinematical scattering I: non-crystalline materials*, in *Elements of Modern X-ray Physics*. 2011. p. 113-146.

119.   Lin, C.H., et al., *Structures and magnetic properties of Co and CoFe films prepared by magnetron sputtering.* Thin Solid Films, 2011. **519**(23): p. 8379-8383.

120.   Liu, L.-g. and W.A. Bassett, *Changes of the crystal structure and the lattice parameter of SrO at high pressure.* Journal of Geophysical Research (1896-1977), 1973. **78**(35): p. 8470-8473.

121.   INYANG, O.-O., *Magnetic proximity effect and interfacial spin dependent transport in ferromagnet/heavy metal thin films*. 2018, Durham University.

122.	Liu, H., et al., *Manipulations of inverse spin Hall effect in a FM/Pt/FM trilayer structure via RKKY interlayer interaction*. 2017. p. B47.006.

123.	Johnson, M.T., et al., *Magnetic anisotropy in metallic multilayers*. Reports on Progress in Physics, 1996. **59**(11): p. 1409.

124.	Néel, L., *Anisotropie magnétique superficielle et surstructures d'orientation*. J. Phys. Radium, 1954. **15**(4): p. 225-239.

125.	Stamps, R.L., *Mechanisms for exchange bias*. Journal of Physics D: Applied Physics, 2000. **33**(23): p. R247.

126.	Victora, R.H. and J.M. MacLaren, *Theory of magnetic interface anisotropy*. Physical Review B, 1993. **47**(17): p. 11583-11586.

127.	Cestarollo, L., K. Srinivasan, and A. El-Ghazaly, *Investigation of perpendicular magnetic anisotropy in Pt/CoFeB/Pt multi-layer structures*. Journal of Magnetism and Magnetic Materials, 2022. **562**: p. 169825.

128.	Grünberg, P., et al., *Layered Magnetic Structures: Evidence for Antiferromagnetic Coupling of Fe Layers across Cr Interlayers*. Physical Review Letters, 1986. **57**(19): p. 2442-2445.

129.	Krebs, J., et al., *Magnetic resonance determination of the antiferromagnetic coupling of Fe layers through Cr*. Physical review letters, 1989. **63**(15): p. 1645.

130.	Zivieri, R., L. Giovannini, and F. Nizzoli, *Acoustical and optical spin modes of multilayers with ferromagnetic and antiferromagnetic coupling*. Physical Review B, 2000. **62**(22): p. 14950.

131.	Dinia, A., N. Persat, and H. Danan, *Temperature induced perpendicular magnetic anisotropy in Co/Cu/Co trilayers*. Journal of Applied Physics, 1998. **84**(10): p. 5668-5672.

132.	Dhanapal, K., et al., *Magnetic anisotropy studies on pulsed electrodeposited Ni/Ag/Ni trilayer*. Applied Surface Science, 2014. **313**: p. 698-703.

133.	Thomas, O., et al., *Interplay between Anisotropic Strain Relaxation and Uniaxial Interface Magnetic Anisotropy in Epitaxial Fe Films on (001) GaAs*. Physical Review Letters, 2003. **90**(1): p. 017205.

134.	Hindmarch, A.T., et al., *Influence of deposition field on the magnetic anisotropy in epitaxial CoFe films on GaAs(001)*. Physical Review B, 2010. **81**(10): p. 100407.

135.	Hindmarch, A.T., et al., *Origin of in-plane uniaxial magnetic anisotropy in CoFeB amorphous ferromagnetic thin films*. Physical Review B, 2011. **83**(21): p. 212404.

136.	Silva, E.F., et al., *Thickness dependence of the magnetic anisotropy and dynamic magnetic response of ferromagnetic NiFe films*. Journal of Physics D: Applied Physics, 2017. **50**(18): p. 185001.

137.	Michael, F., *Ferromagnetic resonance of ultrathin metallic layers*. Reports on Progress in Physics, 1998. **61**(7): p. 755.

138.   Holanda, J., et al., *Magnetic damping modulation in IrMn 3/Ni 80 Fe 20 via the magnetic spin Hall effect.* Physical review letters, 2020. **124**(8): p. 087204.

139.   *Magnetic Anisotropy*, in *Introduction to Magnetic Materials*. 2008. p. 197-239.

140.   Sandler, G., et al., *Determination of the magnetic damping constant in NiFe films.* Journal of applied physics, 1999. **85**(8): p. 5080-5082.

141.   Li, Y., et al., *Suppressing Magnetic Damping Related to Two-Magnon Scattering in Ultrathin NiFe Films by Interface Engineering.* The Journal of Physical Chemistry C, 2022. **126**(17): p. 7748-7754.